PARALLEL AND PERPENDICULAR MOMENTUM DISTRIBUTIONS IN PROJECTILE FRAGMENTATION REACTIONS

By

Krista C. Meierbachtol

A DISSERTATION

Submitted to
Michigan State University
in partial fulfillment of the requirements
for the degree of

DOCTOR OF PHILOSOPHY

Chemistry

2012

ABSTRACT

PARALLEL AND PERPENDICULAR MOMENTUM DISTRIBUTIONS IN PROJECTILE FRAGMENTATION REACTIONS

by

Krista C. Meierbachtol

Projectile fragmentation has been used for decades to produce rare isotope beams for use in advancing nuclear science. Multiple observables are available for studying the underlying reaction mechanism including measurement of the linear momentum of final fragmentation products. Furthermore, the two components of the linear momentum, the parallel momentum distribution and the perpendicular momentum distribution, have been studied very disparately with more measurements of the parallel momentum distribution of fragmentation products.

The full parallel and perpendicular momentum distributions have been measured as a function of fragment mass loss for a wide range of fragments ($37<A<75$, $17<Z<33$) produced from interaction of a ^{76}Ge beam at 130 MeV/nucleon on either a ^{9}Be or ^{197}Au target. The parallel momentum distributions were found to be independent of target species and agree with both previous measured distributions and models of distribution width by Goldhaber and Morrissey. The perpendicular momentum distributions were found to agree with models of the distribution width by Van Bibber for fragments produced with the light beryllium target or fragments with a mass loss of $\Delta A>20$ produced with the heavy gold target. The distribution widths of the heaviest fragments produced with the gold target had scattering angles that could be described by a calculation of the classical deflection function using a repulsive Coulomb plus an attractive nuclear scattering potential between the fragment and

the gold target.

The particle identification procedure used with the S800 spectrometer at the National Superconducting Cyclotron Laboratory has been improved by the addition of the identification of the atomic charge-state of incoming particles. The total kinetic energy of incoming particles can now be measured with a new CsI(Na) hodoscope array, which has been characterized as a function of particle energy, mass, and nuclear charge. The energy resolution was deduced to be approximately 3% in the 100 GeV total kinetic energy regime.

ACKNOWLEDGEMENTS

First I would like to thank my advisor, Dave Morrissey. The support he provided to help me transition to a brand-new research project and finish it in three years can't be measured or valued enough. There have been many occurrences where I was slightly less than calm about my research but Dave never failed to boil it all down to the simplest terms and even supply the occasional encouraging word. I know I could not have accomplished this without his guidance and expertise. I would also like to thank my other guidance committee members, Paul Mantica, Brad Sherrill, Remco Zegers, and Daniel Bazin for their time, insights and helpful discussions about my research. I would especially like to thank Daniel for all the time he spent helping with the hodoscope and for answering all of my many, many questions - even the ones I asked more than once.

There are also numerous people at NSCL that deserve my thanks and appreciation. The many designers, engineers, machinists, staff physicists, and many more people than I have room to mention have made working here a very positive and fun experience. I could have not accomplished my research without their expertise and help along the way. I also want to thank the many people who have become my friends during my time here. All of you have made the hard work worth it and I will always cherish the memories of grad school because of you all. I definitely wouldn't have survived the stress and worries of grad school without such great friends along the way.

I definitely need to thank my family, both by birth and by marriage. You have been my endless cheerleaders, pillars of support, and freely gave your love and encouragement when I needed it most. While you all claim you could never understand what I do I want you to know all of you know that you I'll never understand how I've managed to be so lucky to

have such amazing people in my life that I have the honor of calling family.

Finally and most importantly I want to thank my husband Collin. Your constant, endless support on a daily basis has sustained me and was crucial to me accomplishing this work. You held me up when I wanted to give up and believed in me when I couldn't. I could not have done it without you and I am grateful every day that you are in my life. You deserve a million thank-you's but I'll just start with this one: Thank you.

TABLE OF CONTENTS

LIST OF TABLES

LIST OF FIGURES

Chapter 1

Introduction

1.1 Rare Isotope Beams in Nuclear Science

The construction of the first cyclotron accelerator by Ernest O. Lawrence and M. Stanley Livingston in 1931 [1] shifted the course of nuclear science dramatically. The study of nuclear reactions was no longer restricted to reactions with particles emitted by natural radioactive sources. As the advancement in accelerator technology continued past Lawrence's proton accelerator, more particle species and energy regimes became accessible for production of beams of particles to the point that intense beams of stable particles were available almost half a century ago. Subsequently, the emphasis shifted to the production of not only stable nuclei but unstable, or radioactive, species as well, extending out to the most rare, short-lived species. The advent of rare isotope beams opened many new avenues in nuclear physics. For example, the structure of isotopes along the dripline could now be studied, reaction mechanisms involving unstable isotopes could be studied in detail, and nuclei that are only present in astrophysical phenomena could now be probed in a laboratory setting. Rare

isotope beams have also provided technical and theoretical challenges to nuclear scientists. New detectors were necessary to measure the unusual products of secondary reactions as were advances in accelerator technology to produce the new beams. Theoretical advances also occurred as predictions and explanations of new features of nuclear structure became apparent with the rare isotope beams.

1.2 Methods of Rare Isotope Beam Production

The two main methods available for producing rare isotope beams are target fragmentation and projectile fragmentation, shown schematically in Figure 1.1. Each method has its advantages and disadvantages discussed in the following subsections. The essential difference is the source of the rare isotopes; target fragmentation produces rare isotopes by fragmentation of the target nucleus and the products are trapped in the target lattice while projectile fragmentation produces rare isotopes by fragmentation of the projectile nucleus and these products rapidly exit the target and travel very fast in vacuum. Both techniques have been successfully implemented at a number of laboratories around the world. Present target fragmentation facilities include ISAC at TRIUMF in Canada, HRIBF at ORNL in Tennessee, and ISOLDE at CERN in Switzerland. The present projectile fragmentation facilities include GANIL in France, RIKEN in Japan, GSI in Germany and NSCL in Michigan. The beams available at these and other facilities are diverse in isotope species and kinetic energy and beam time is generally highly oversubscribed by the nuclear science community.

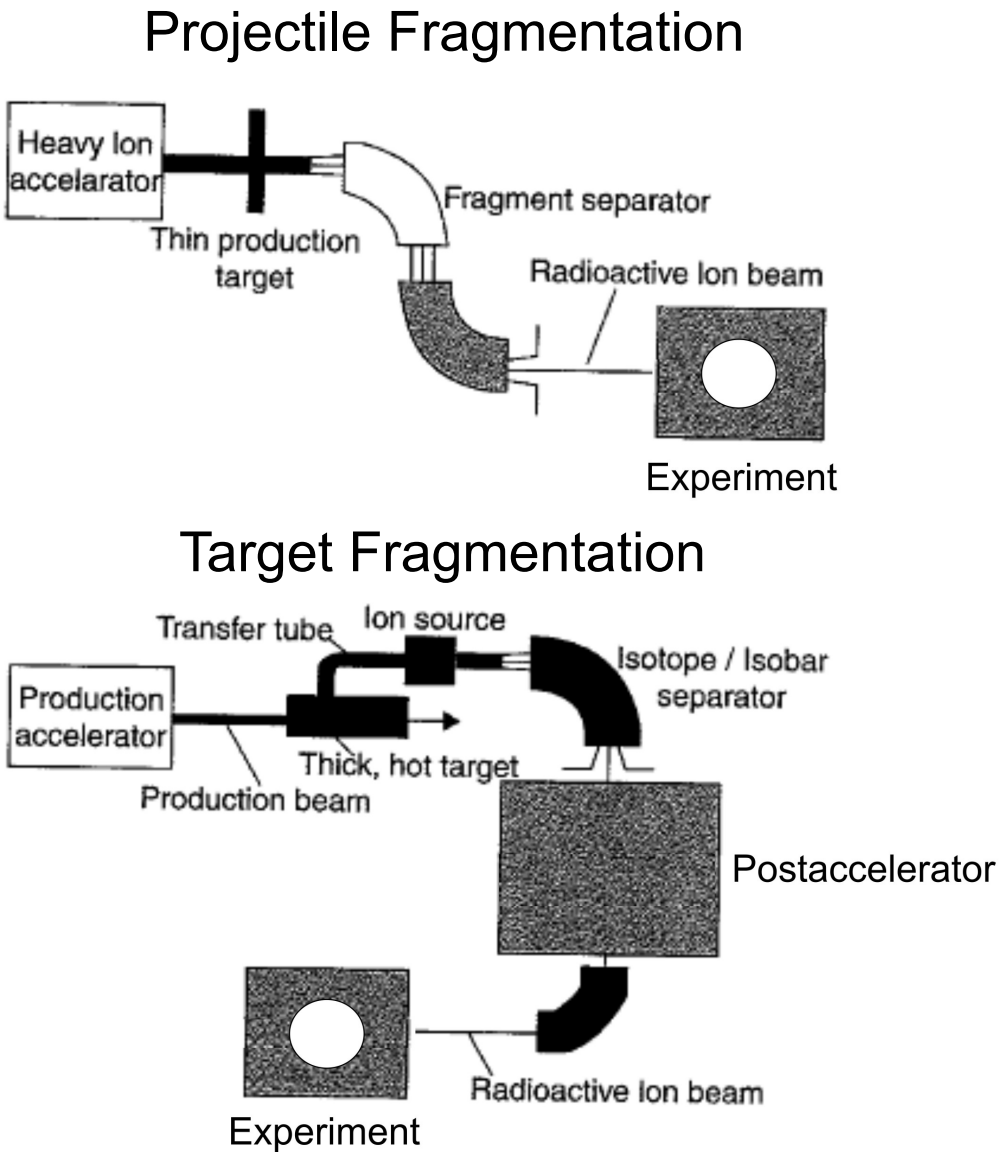

Figure 1.1: Schematic representation of projectile and target fragmentation techniques for producing rare isotope beams. Figure adopted from from [2].

1.2.1 Target Fragmentation

Target fragmentation generally produces rare isotope beams by interacting a high-energy light ion beam, typically protons, on a metal target that is heated to several thousand degrees [2]. A fraction of the protons react with a target nucleus and form a very large variety of products. Products originating from the target nucleus after interaction with a high-intensity proton beam are specifically called spallation products. The fragmentation products thermalize in the target material and many elements can diffuse through the target to the surface according to chemical diffusion properties. Evaporation and subsequent ionization of the fragment(s) leaving the target can be accomplished in multiple ways, including surface ionization, laser ionization, and electron beam ionization [2]. The ionized fragments (generally 1+ ions) are then accelerated to the desired energy in a second accelerator system to produce the final rare isotope beam. Advantages of this technique include potentially high production rates due to intense proton beams and thick targets, highly specific selection of fragment species using chemical selection, and accelerator requirements of only one or two beam species at any time. Drawbacks to this method include the requirement of two separate accelerator systems, and the limitation on short half-life beam species due to time needed for diffusion out of the target material and restrictions due to chemical selectivity.

1.2.2 Projectile Fragmentation

The production of rare isotope beams using projectile fragmentation reactions was developed after intense high-energy beams of heavy ions became available and is in use at the National Superconducting Cyclotron Laboratory (NSCL) at Michigan State University, where the present work was carried out. A stable beam is accelerated to an energy, 50 MeV/nucleon

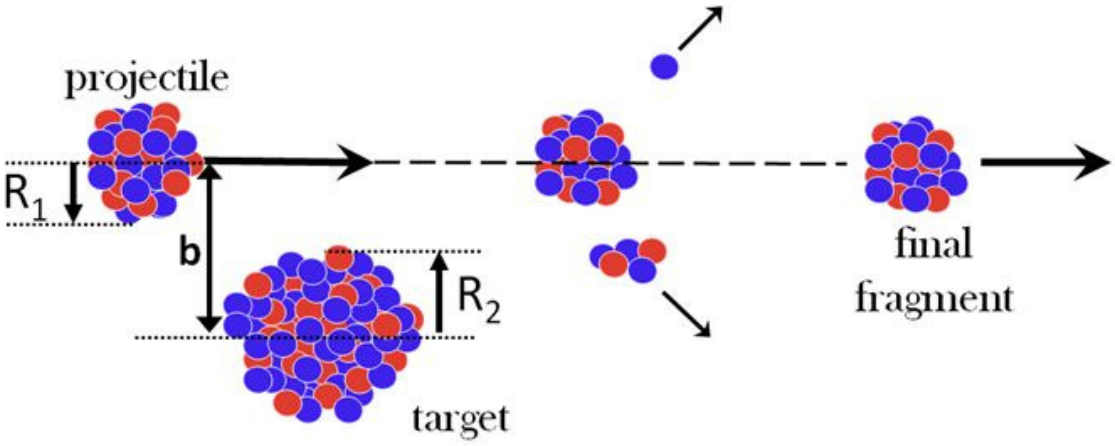

Figure 1.2: Schematic representation of the projectile fragmentation process. R_1 and R_2 are the radii of the projectile and target. b is the impact parameter, defined as the separation distance between the two nuclei. For interpretation of the references to color in this and all other figures, the reader is referred to the electronic version of this dissertation.

and above, that is high relative to the Coulomb barrier and is reacted with a thin, light mass target. Fragmentation of the projectile species occurs when a projectile nucleus with radius R_1 interacts peripherally, labeled by the impact parameter, b, with a target nucleus with radius R_2 and some number of nucleons are removed from the projectile, shown as a schematic cartoon in Figure 1.2. The separation of the resulting reaction products of interest from the unreacted beam and unwanted isotopes is accomplished with a 0 degree fragment separator, which combines dipole and quadrupole magnets to select the desired species [2]. The advantages to rare isotope beam production using projectile fragmentation include essentially no limitation on the half-life of beam species allowing more diverse species available for secondary reactions, and no re-acceleration step as the rare isotope beams retain the majority of the kinetic energy of the original beam. Challenges of projectile fragmentation include lack of control over the properties of the secondary beam, limitations of beam intensity based on thin targets, device acceptances and stable beam intensities [2].

An important consideration in projectile fragmentation reactions is the energy of the primary beam. The probable reaction processes that occur between the projectile and target nuclei depend on beam energy, among other variables. Different reactions are more probable, or have higher cross sections, in particular beam energy regimes. In the low energy regime, typically energies below 20 MeV/nucleon, fragmentation is competing with many processes: elastic and inelastic scattering, transfer, fusion, and compound nucleus reactions to name a few. The intermediate energy regime, typically between 20 and 200 MeV/nucleon, is a transitional region with the fragmentation reaction cross section becoming larger due to the increase in kinetic energy of the projectile to well above the Coulomb barrier. The processes listed in the lower energy regime diminish in cross section compared to the fragmentation process as the beam energy increases, particularly for systems near stability. In the highest energy regime, above approximately 200 MeV/nucleon, 'pure' fragmentation occurs between overlapping projectile and target nuclei. The kinetic energy of the beam particle is now too large to allow for transfer or fusion reactions. The different reaction processes for low and high projectile energies are shown schematically in Figure 1.3.

The stable beams produced at the coupled cyclotron facility (CCF) at the NSCL fall into the intermediate beam energy regime and secondary beams are produced by projectile fragmentation. The rare isotope beam rate capabilities of the CCF at the NSCL are displayed in Figure 1.4 in terms of the production beam rates for each isotope on the chart of nuclides (which arranges isotope species by proton, Z, and neutron, N, numbers) [3]. The large number of isotopes with rate values demonstrates the tremendous range of rare, or short-lived, isotopes that are accessible to be studied or used as secondary beams for further reactions.

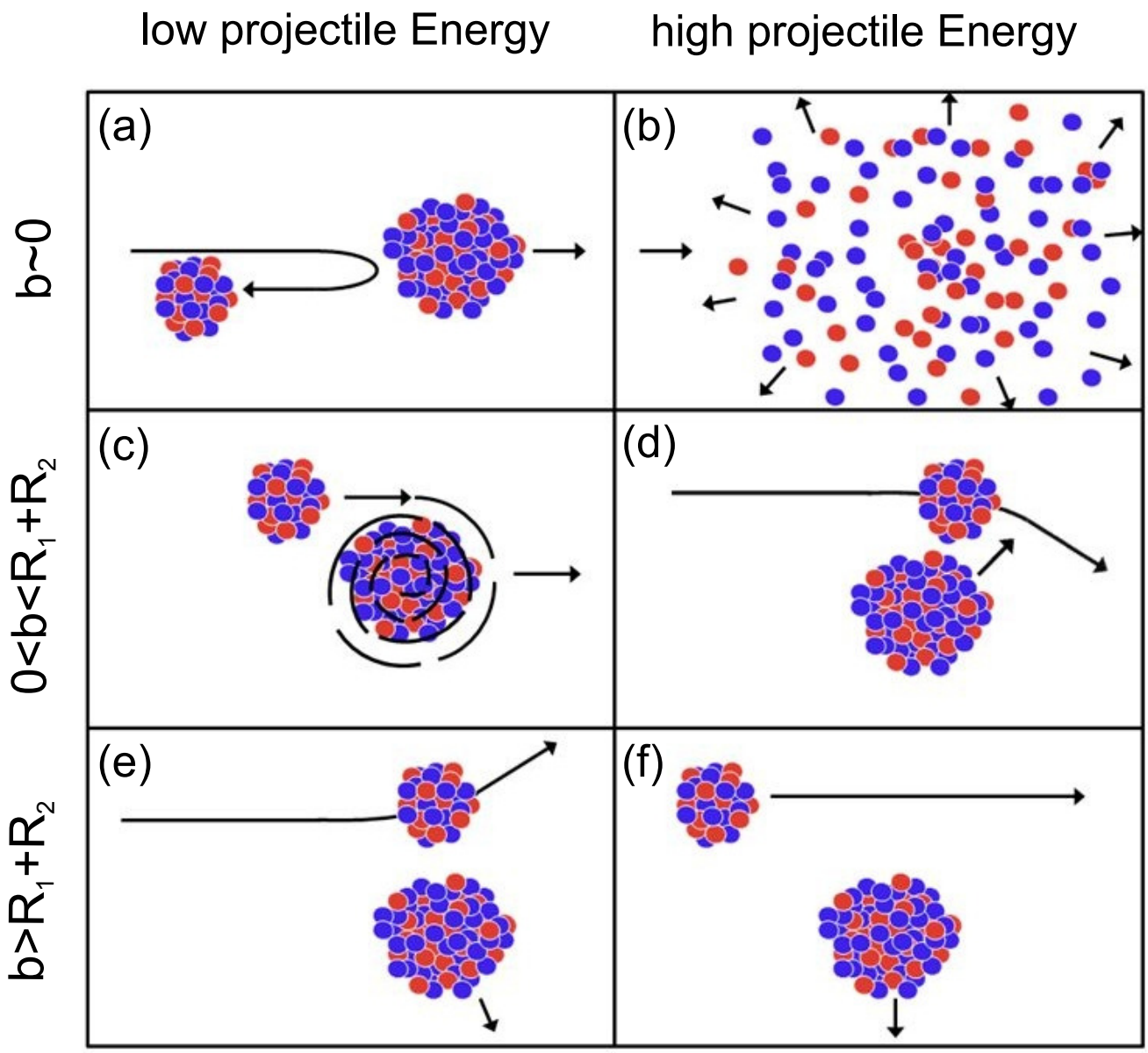

Figure 1.3: Schematic representation of reaction processes arranged according to impact parameter, b, and projectile energy. Illustrated reactions include (a) reflection (b) fission (c) fusion/capture (d) nuclear scattering (e) Coulomb scattering and (f) target deflection.

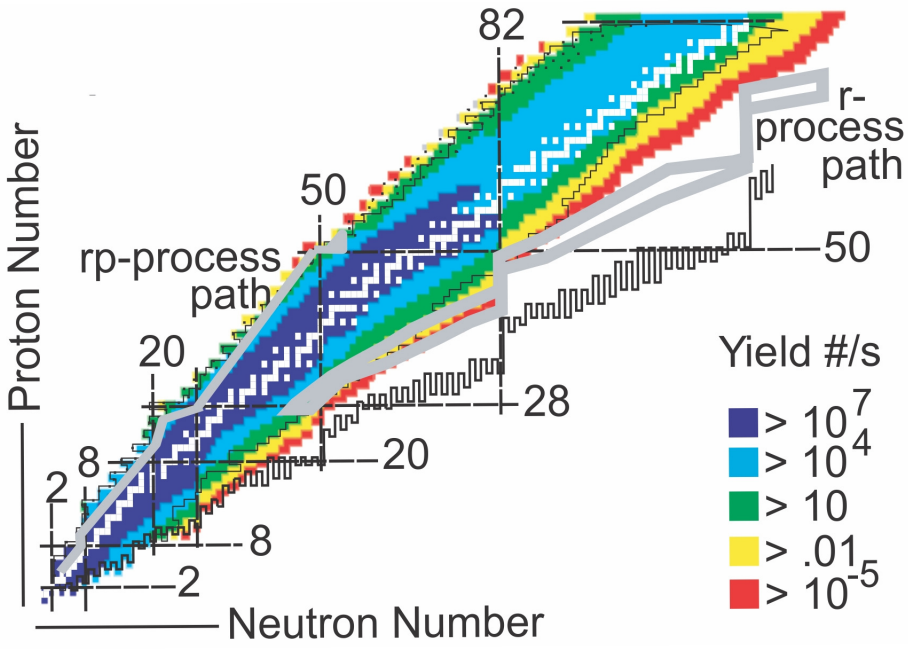

Figure 1.4: Chart of nuclides. Color/shading indicates the beam rate capabilities of the CCF at the NSCL [3].

A model that is often used to describe fragmentation reaction is the two-step process first outlined by Serber [4]. The first step, called the abrasion step, is a fast process lasting on the order of 10^{-23} seconds, in which the target nucleus sheers off or perhaps knocks out some nucleons from the projectile nucleus. The resulting projectile-like fragment continues in a very similar trajectory to the original projectile, most likely in a highly excited state. The second step, called the ablation step, is slower lasting 10^{-16} to 10^{-18} seconds. During this period, the excited fragment decays to the ground state through statistical emission of single particles and/or particle clusters, and gamma-rays. The nucleus that remains after the decay step can be observed and analyzed, typically using a magnetic spectrometer or used in a secondary reaction.

Various observables are available to probe the underlying fragmentation mechanism but few have been studied with a systematic approach covering a broad distribution of projec-

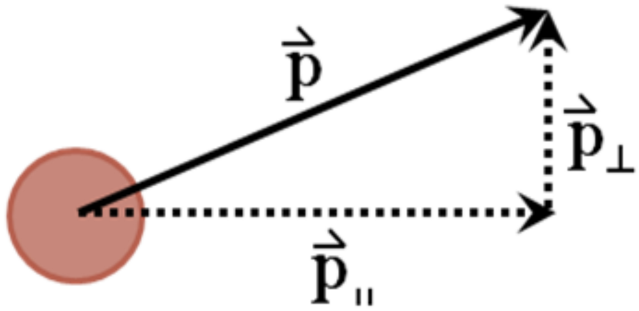

Figure 1.5: Linear momentum vectors of final fragments with the parallel component in the same direction as the beam axis.

tiles, energies and target masses. One observable that has been studied extensively is the fragment cross sections and isotopic distributions of produced fragments over a large range of projectile energies as well as for multiple projectile and target combinations [5–11]. Models for predicting cross sections have been developed, applicable to a wide range of fragmentation cross sections , [12, 13], and are used in the day-to-day operation of secondary beam facilities. Another observable that has been studied is the linear momentum distribution of the fragmentation products. The next section will discuss the linear momentum observable in detail including previous measurements, empirical descriptions, and insights this observable can provide into the fragmentation mechanism.

1.3 Linear Momentum Distributions

The conservation of momentum in a nuclear reaction can be used to relate the measured momentum distributions of the outgoing final fragments to the reaction process between the original projectile and target. The vector components of the linear momentum distribution of an outgoing fragment, shown in Figure 1.5, can be measured using the dispersive properties of a magnetic spectrometer and position sensitive detectors. The majority of published

results of momentum distributions, and the accompanying descriptions, have focused on the parallel, or longitudinal momentum component, $p_{\parallel}$, which is by far the largest fraction of the linear momentum associated with typical projectile fragmentation reactions. Published results for the perpendicular, or transverse, momentum component, $p_{\perp}$, are scant [14–16]. In general, experimental momentum distributions are well described by a Gaussian function and values of the distribution widths and peak positions have been reported in the literature [8, 17–20]. Descriptions of the variations of the widths and peak values of the distributions have also developed [17, 19, 21, 22]. The widths of the distribution have been found to depend on the fragment mass, or the projectile and fragment masses, but not on the target mass. Details of experimental results and models that have been developed for each component of the linear momentum will be presented in the following sections.

1.3.1 Parallel Momentum

The parallel, or longitudinal, component of the momentum distribution for fragments produced from projectile fragmentation reactions has been measured and modelled extensively and has been described as a function of projectile and target mass, projectile energy, and fragment mass. Results for the parallel momentum distributions of fragmentation products span a wide range of projectile species from ^{12}C to ^{238}U, of projectile energies from 22 MeV/nucleon to 2.1 GeV/nucleon, and target species from beryllium to lead [7,17,19,20,23]. The plethora of experimental data has allowed the development of empirical descriptions of the linear parallel momentum distributions of fragments. The first and most often applied description of the width of the distribution was proposed by Goldhaber [24]. Goldhaber as-

sumed a one-step sudden fragmentation process to produce the final fragment. The width, σ, of the distribution in the Gaussian function, $exp(-p^2/2\sigma^2)$, is described by the expression:

$$\sigma^2_{p_\parallel} = \sigma^2_o \frac{K(A-K)}{A-1}, \tag{1.1}$$

where K is the fragment mass, A is the projectile mass, and the coefficient σ_0, also called the reduced width, is estimated the mean square momentum, $< p^2 >$, as:

$$\sigma_o = \frac{< p^2 >}{3}, \tag{1.2}$$

and the approximation of the mean square momentum following the Fermi momentum, p_F, of the uncorrelated nucleon in the projectile:

$$< p^2 >= \frac{3p_F}{5}. \tag{1.3}$$

Equations 1.2 and 1.3 can be combined to get a final description of the coefficient σ_0:

$$\sigma_o = \frac{p_F}{\sqrt{5}}. \tag{1.4}$$

The value of p_F can be determined from electron scattering measurements on the nucleus of interest [25, 26]. The data used to develop the expression in Equation 1.1 came from measurements with the relatively light ^{12}C and ^{16}O beams at energies of 1.05 and 2.1 GeV/nucleon, respectively, on targets ranging from beryllium to lead [17]. Many comparisons of experimental results for the parallel momentum distributions have applied Goldhaber's model with varying success [20, 23, 27, 28]. The range in values for the reduced width was summarized by Blumenfeld *et al.* [7] and Murphy *et al.* [29]. An updated version of their summaries is presented in Figure 1.6 [5, 7, 17, 20, 23, 29–35].

A second description of the width of the parallel momentum distribution by Morrissey [36] treated the fragmentation process as two steps (abrasion and ablation) and reduced the

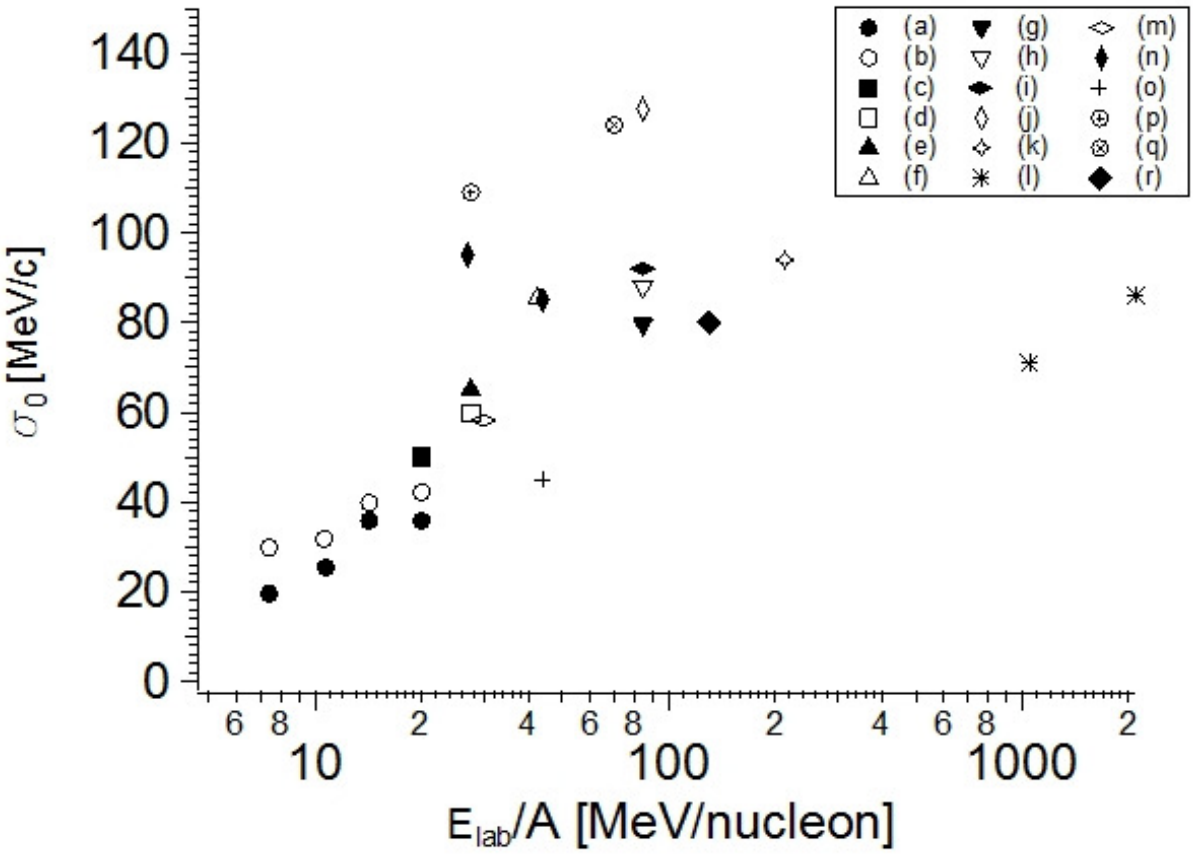

Figure 1.6: Compilation of reduced width values as a function of projectile energy. (a) ^{197}Au(^{20}Ne,^{16}O) [30] (b) ^{197}Au(^{20}Ne,^{12}C)[30] (c) ^{208}Pb(^{16}O,^{12}C) [31] (d) ^{197}Au(^{9}Be,^{7}Li) [29] (e) ^{197}Au(^{9}Be,^{6}Li) [29] (f) ^{181}Ta(^{20}Ne,X) [32] (g) ^{12}C(^{12}C,^{6}Li) [33] (h) ^{12}C(^{12}C,^{7}Li) [33] (i) ^{12}C(^{12}C,^{7}Be) [33] (j) ^{12}C(^{12}C,^{10}B) [33] (k) ^{232}Th(^{40}Ar,X) [5] (l) Be-Pb(^{16}O,X)[17] (m) Ni,Ag,Au(^{20}Ne,X) [34,35] (n) ^{40}Ca(^{40}Ar,X) [7] (o)^{208}Pb(^{20}Ne,X) [7] (p) ^{68}Zn(^{40}Ar,X) [20] (q) ^{27}Al(^{86}Kr,X) [23] (r) This Work ^{9}Be,^{197}Au(^{76}Ge,X).

expression for the width to only the difference in mass between the fragment and the original projectile:

$$\sigma_{p_{||}}^2 = \sigma_o^2 \sqrt{\Delta A}, \tag{1.5}$$

where $\Delta A = A_{projectile} - A_{fragment}$ and σ_o^2 is a constant determined from data. The data used to develop the expression in Equation 1.5 included fragment species originating from both projectile and target fragmentation processes.

The average parallel momentum shift or transfer, $\langle p_{||} \rangle$, which describes the average momentum needed to remove one nucleon in the fragmentation process has also been studied by Morrissey and others [23, 36]. The relationship of the momentum transfer as a function of mass loss of the fragment, ΔA, was observed to be linear for fragments originating from the projectile and target in MeV/c/nucleon:

$$\frac{\langle p_{||} \rangle}{\Delta A} = -8. \tag{1.6}$$

As mentioned previously, the projectile energy influences the probability of the nuclear reaction mechanism. At the lowest energies of a few MeV/nucleon, nuclear reactions are blocked by the Coulomb barrier. At slightly higher energies, the fusion of two nuclei becomes possible, but as the energy increases the nuclei can not thermalize the incident energy and momenta and the projectile and target retain their identities except in the most central collisions. The momentum distribution results in previous publications reflects this influence of the projectile energy. Friedman *et al.* [19] concluded Coulomb scattering reduced width values for momentum distributions of fragments in the transition energy region of 10-20 MeV/nucleon. Transfer reactions were cited as the major production reaction for fragments with scattering angles near or below the grazing angle, defined as the maximum

scattering angle associated with Coulomb scattering, in multiple experimental reaction conditions [7, 27, 28]. The distortion of the Gaussian distribution shape of parallel momentum distributions with a low energy tail was attributed to the presence of dissipative processes in addition to fragmentation [23]. Both Blumenfeld *et al.* [7] and Rami *et al.* [20] concluded that the widths of the momentum distributions for fragment species near the projectile mass had to be described separately, with different coefficients than fragments with masses further away from the projectile mass. The breadth of the participating reaction mechanisms, in addition to fragmentation as discussed in previous publications, is an indication of the complexity involved in studying projectile fragmentation via final fragment momentum distributions.

1.3.2 Perpendicular Momentum

The perpendicular, or transverse, component of the linear momentum distribution for fragmentation products have been measured less often and only one empirical equation has been developed in an attempt to describe the width of the observed distributions. Experimental data for perpendicular momentum are currently limited to heavy projectiles with energies above 200 MeV/nucleon [14–16]. The only empirical equation for describing the widths of the perpendicular momentum distributions, $\sigma_{p_\perp}$, was proposed by Van Bibber *et al.* [18] and follows a similar approach to that taken by Goldhaber for the parallel distributions:

$$\sigma^2_{p_\perp} = \sigma^2_o \frac{F(A-F)}{A-1} + \sigma^2_1 \frac{F(F-1)}{A(A-1)}. \tag{1.7}$$

Here A = projectile mass, F = fragment mass, and σ_1 is the variance of the transverse momentum of the projectile:

$$\sigma_1^2 = \frac{1}{2}\langle p_\perp^2 \rangle. \tag{1.8}$$

The first term in Equation 1.7 is identical to Goldhaber's description of the width of the parallel momentum distribution. Van Bibber *et al.* suggested the second term to account for the additional orbital deflection of the projectile due to Coulomb repulsion from the target. The experimental data used to derive Equation 1.7 included fragments with A>3 produced from fragmentation of ^{16}O at 90 and 120 MeV/nucleon.

1.4 Motivation for this work

The motivation of this work was two-fold; one scientific and one technical. The scientific motivation was to measure complete momentum distributions of projectile fragmentation reactions to better understand the underlying reaction mechanism, and the technical motivation was to construct a new scintillation detector that would improve particle identification of fragments in the NSCL S800 spectrometer. Details regarding the methods, measurements, and results that went into the successful realization of these two goals are detailed in the following sections.

1.4.1 Momentum Distribution Measurements

The main motivation of this work was to provide new data for the complete momentum distributions of projectile fragments. As mentioned previously, projectile fragmentation reactions are one of the two means for producing rare, unstable isotope beams for the nuclear

science community. As the drive to produce ever more exotic beam species continues, the details of the reaction process must be clearly understood to be able to have a reliable method to predict yields of the rare reaction products, including both cross sections and kinematics. The trend toward using projectile beams with higher masses and higher energies will test the empirical models established based on data collected for low A beams. More specifically, two components of the fragment linear momentum have not been investigated equally, and as such the perpendicular momentum component and its systematic behavior remains largely unknown and untested.

1.4.2 Improved Particle Identification

The second motivation of this work was to improve the particle identification capabilities of the S800 magnetic spectrometer detector system located at NSCL by adding a detector system capable of identifying the atomic charge-state of the detected particles. Complete particle identification (A,Z,q) is critical to experiments utilizing the S800 spectrometer, and the trend over time of using higher mass rare isotope beams will make knowledge of q all the more important. The combination of two high mass species in a reaction generally results in the increased likelihood of the production of fragments with multiple atomic charge states. Identification of the atomic charge state is required to eliminate particle identification ambiguities, a concern in any experiment analysis.

Prior to this work, particle identification of the incoming particles in the S800 spectrometer was limited to two quantities; atomic number, Z, which was obtained from an energy loss measurement, $\frac{dE}{dx}$, and the mass-to-charge ratio, $\frac{m}{q}$, of the incoming particle which was

deduced from the magnetic rigidity and time-of-flight:

$$\frac{m}{q} = \frac{B\rho}{\beta\gamma}. \tag{1.9}$$

Here Bρ is the magnetic rigidity of the particle and is calculated from the particle's position at the focal plane of the S800 and the measured Bρ of the spectrometer, Bρ_O:

$$B\rho = B\rho_O\,(1+\delta)\,, \tag{1.10}$$

where $\delta = \frac{\Delta p}{p} = \frac{\Delta x}{x_0}$ is the fractional deviation of the particle from the center position of the spectrometer [37]. β in equation 1.9 is the ion velocity relative to the speed of light, c, γ is the Lorentz factor, both calculated from the time-of-flight (TOF) of the particle [37]. The addition of a total kinetic energy measurement, TKE, can be combined with the deduced mass-to-charge ratio to independently determine the atomic charge, q, state of the particles using the following relationship [37]:

$$q = \frac{TKE}{u(\gamma-1)(A/q)}, \tag{1.11}$$

where u is the atomic mass unit. This relation can be derived from the kinetic energy relation:

$$TKE = (\gamma-1)mc^2. \tag{1.12}$$

The approximation, $m \approx Au$, which disregards the nuclear binding energy, is a valid approximation after considering the integer mass resolution of the spectrometer, and setting c=1, was combined with the measurement of the mass number A as the ratio A/q with the spectrometer. Equation 1.12 now looks like:

$$TKE(q) = (\gamma-1)u(A/q), \tag{1.13}$$

which can be re-arranged to get equation 1.11. Before this work, the ions came to rest in a thick plastic scintillator, which provided a low resolution measurement of the total residual energy. As part of this work a new high resolution detector was constructed and tested with the goal of improving the energy resolution to be able to distinguish atomic charge states.

1.5 Dissertation Outline

The goal of the present work was to obtain new data on the full linear momentum distributions of projectile fragments to improve understanding of projectile fragmentation reactions. As indicated above, there is little information on the transverse momentum distributions. In addition, a new detector will be installed in the S800 focal plane to provide a measurement of the atomic charges. The details of the equipment used during the experiment are given in Chapter 2, including details of the development of a new hodoscope necessary for improving particle identification at the S800 focal plane. The focus of Chapter 3 is on the specifics of the data analysis used to extract the momentum measurements and the characterization of the hodoscope. Chapters 4 and 5 present and discuss relevant results, and Chapter 6 contains a summary of this work.

Chapter 2

Experimental Details

The experimental measurements discussed in this dissertation were performed during NSCL experiment number 10501, which was carried out during a 24-hour period on March 24, 2010. This chapter focuses on the practical aspects of the experiment. Details of the set-up, of the equipment used to perform the experiment, and the execution are discussed.

2.1 Primary Beam Production

A $^{76}Ge^{32+}$ stable ion beam was used in the experiment, and was provided by the Coupled Cyclotron Facility (CCF) at the National Superconducting Cyclotron Laboratory (NSCL) at Michigan State University. Details of the primary beam production are discussed below.

2.1.1 Ion Source

The first step in producing a primary beam at the CCF is to obtain ions from a stable material, typically a gas or a solid metal. Ions are produced at NSCL using one of two electron cyclotron resonance sources (ECRs) that are labelled in Figure 2.1 as "ion sources".

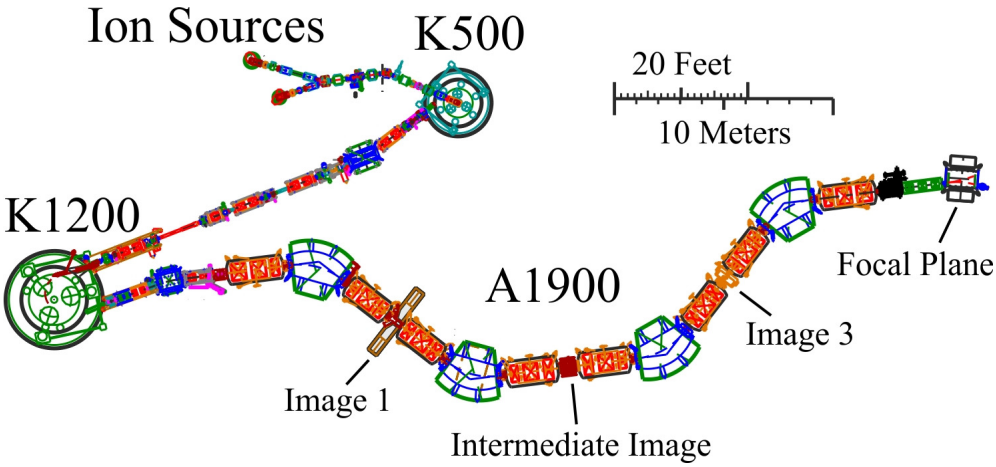

Figure 2.1: Schematic layout of the NSCL ion sources, coupled cyclotron facility and A1900 fragment separator. The ion sources produce stable isotope ions for injection into the coupled cyclotrons, K500 and K1200, which accelerate the ions to the desired energy [39].

The ECRs produce ions by volatilizing stable atoms, which are then ionized by a weak plasma in a "magnetic bottle" that holds the ions in place using magnetic fields to allow further ionization by bombardment with electrons heated by microvave radiation. The ion source used in the experiment was the superconducting source for ions (SuSI) [38]. After the initial ionization to a charge state of 12+, the ions are transported into the K500 cyclotron.

2.1.2 Coupled Cyclotrons

The CCF at NSCL consists of two cyclotrons, shown schematically in Figure 2.1, the K500 and K1200, with the number designating the acceleration capability of each cyclotron to accelerate a proton to either 500 MeV or 1200 MeV, respectively. The K500 cyclotron provided the first stage of acceleration. The ^{76}Ge beam exited the K500 with an energy of 11.6 MeV/nucleon and a charge state of 12+. The ions then pass through a carbon stripper foil to remove electrons and increase the charge state of the ions. The ions were then accelerated to the desired final energy in the K1200 cyclotron which in the present case was 130

MeV/nucleon, with a charge state of 30+. A second stripper foil was placed at the exit of the K1200 to remove the two remaining electrons and achieve a final charge state of 32+ for delivery to the experiment. The used of a fully stripped ion beam simplified the magnetic alignment before and after the plastic scintillator located at the object position of the S800 spectrometer because no electrons are present to be stripped off the beam by the scintillator.

2.1.3 A1900 Fragment Separator

The 130 MeV/nucleon $^{76}Ge^{32+}$ beam was tuned through the A1900 fragment separator which is shown schematically in Figure 2.1. The A1900 fragment separator, which is a combination of four dipole and eight quadrupole triplet superconducting magnets, is typically used to separate a desired secondary beam from the unreacted primary beam and other reaction species that are produced in a target at the A1900 object position [39]. The first two dipole magnets separate desired ion species from the original beam ion species based on the relation between the magnetic rigidity, Bρ, and the momentum, p, and the atomic charge, q, of the ions:

$$B\rho = \frac{p}{q}. \tag{2.1}$$

At the intermediate image two position, the beam is fully dispersed in momentum and a wedge can be used to provide additional separation based on energy loss when combined with the final pair of dipoles [40]. The quadrupole triplet magnets in the A1900 focus or defocus ions as necessary. Momentum acceptance of the A1900 is 5% and the solid angle acceptance is 8 msr. Since the beam used in NSCL experiment 10501 was a stable beam produced by the coupled cyclotrons, the A1900 was not operated as a fragment separator

but was simply used for beam transport. However, the A1900 was used to measure the momentum spread of the beam from the K1200. The spread was found to be 0.076%.

2.2 S800 Spectrometer

The $^{76}Ge^{32+}$ beam was transported from the A1900 to the analysis beam line of the S800 spectrometer, shown schematically in Figure 2.2. The analysis beam line contains an object box, four dipoles, five quadrupole triplets, and four sextupole superconducting magnets. The S800 spectrometer itself consists of a quadrupole doublet followed by two large dipole superconducting magnets [41]. The two dipole magnets each have a 75 degree bending angle and a nominal maximum magnetic rigidity of 4 Tm. The S800 spectrometer has a momentum acceptance of 5% and a solid angle acceptance of 20 msr. The S800 spectrometer disperses the beam in the vertical direction with a large acceptance in the horizontal direction. The targets in the present work were placed at the pivot point of the spectrometer. Two separate targets were used, either a 99.8 mg/cm^2 ^{9}Be target or a 50.73 mg/cm^2 ^{197}Au target.

The ion optics of the beamline and spectrometer can be operated in two modes, dispersion-matching mode and focus-mode. The focus-mode is the usual mode of operation for the majority of scattering experiments for the spectrometer and was used for this experiment. Focus-mode requires that the S800 analysis beam line be achromatic with focus points at the object box and the target position, see labelling in Figure 2.2. The momentum acceptance of the analysis line is ±2% in focus-mode operation, with a momentum resolution of approximately 1 part in 10000 per mm of beam spot size [41]. Particles entering the spectrometer are separated by their momentum-to-charge ratio. Those with the appropriate Bρ, based on mass and energy, will be transported to the S800 focal plane. A fast plastic

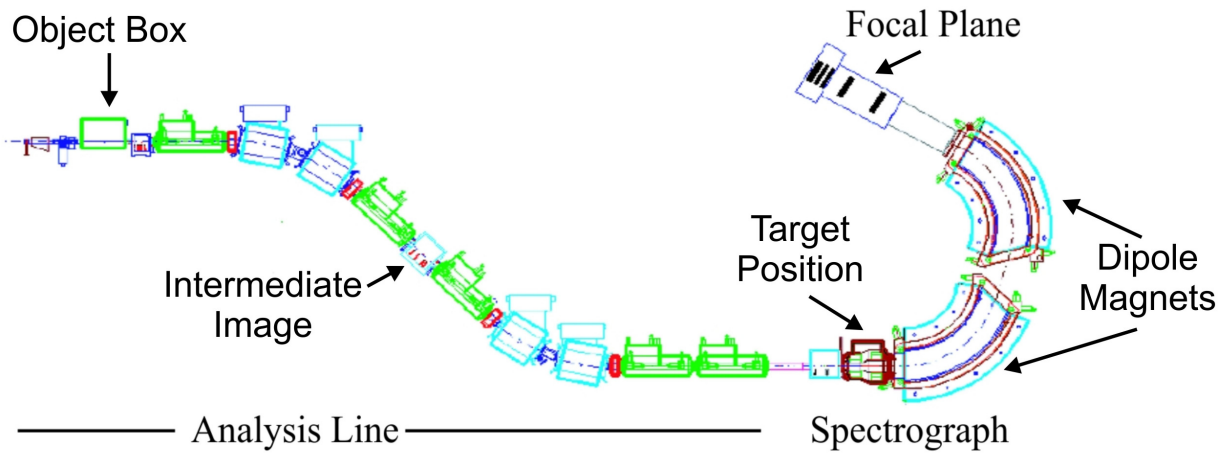

Figure 2.2: Schematic layout of the S800 analysis beam line and spectrometer [41].

scintillator located in the object box of the beam analysis line provided a time-of-flight signal to the experiment that acted as the 'stop' timing signal. Since the S800 is an uncorrected spectrometer, with respect to magnetic corrections, off-line software techniques are use the measured velocity vector of the ions at the focal plane must be to determine the magnetic rigidity.

2.3 Focal Plane Detectors

The S800 focal plane box contains five detectors for measuring various observables of the forward-focused outgoing components of the reaction of interest. A mechanical drawing of all the detectors is shown in Figure 2.3. The most upstream detectors were two cathode readout drift chambers (CRDCs) separated by approximately 1 m for position and angle measurements [42]. The next downstream detector was a gas-filled ionization chamber for measuring the energy loss of the particles. Immediately downstream of the ionization chamber was a thin plastic scintillator, used for time-of-flight measurements. Finally, a new 32

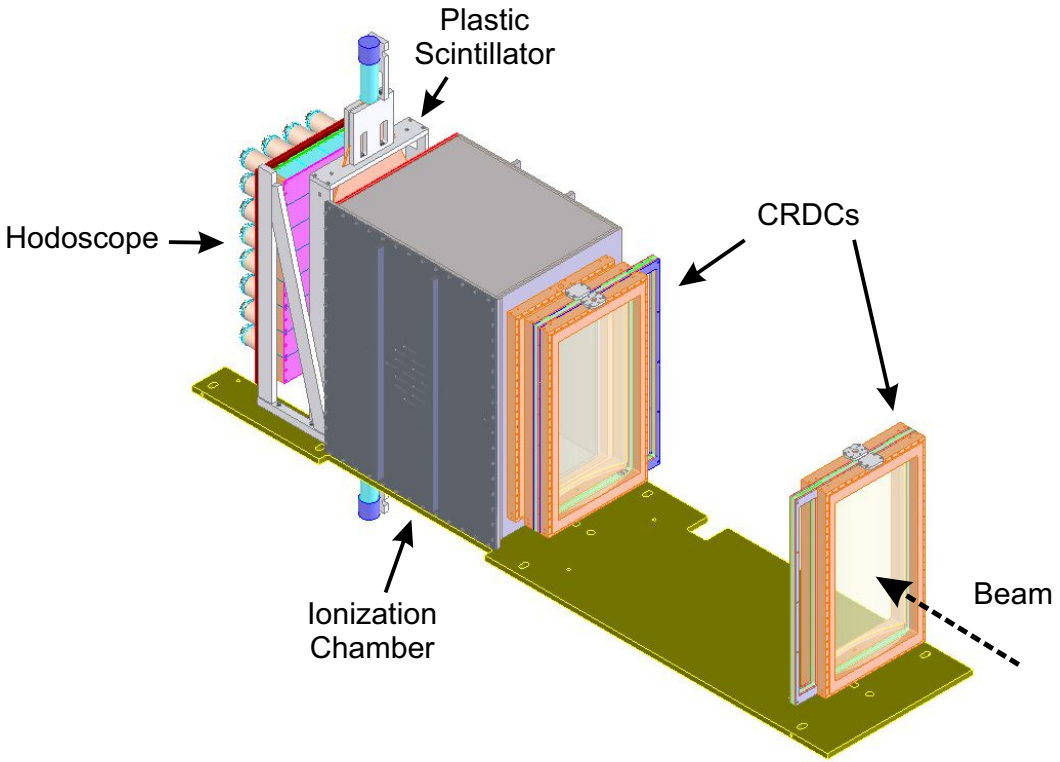

Figure 2.3: Schematic drawing of the particle detectors in of the focal plane box. The dashed black arrow indicates the beam direction. The detectors in the order the beam encounters them were two Cathode Readout Drift Chambers (CRDCs), an ionization chamber, a plastic scintillator and an array of cesium iodide crystals.

CsI(Na) crystal hodoscope was used to measure total kinetic energy. Prior to the present work, the final detectors in the focal plane were two plastic scintillators. The total energy signal from the scintillators was needed to identify the atomic charge of the stopping ions. The energy resolution was not sufficient in the initially deployed plastic detectors to treat heavy ions (A≥10). One of the motivations of the present work was to build and test the hodoscope that was expected to have a better resolution than the plastic scintillators and provide necessary atomic charge state determination. The following sections provide details on each detector in the focal plane.

2.3.1 Cathode Readout Drift Chambers

Two gas-filled CRDCs were located in the most upstream portion of the focal plane detector box of the S800 spectrometer. The two detectors were separated by 1.073 m and each had an active area of 30 cm by 59 cm and an active depth of 1.5 cm. The CRDCs were used to determine position and angle of particles at the focal plane. Each detector contained 80% CF_4 and 20% C_4H_{10} gas at 140 torr [42]. A particle passing through the gas created an ionization track. The ionized electrons drifted to the anode wire, which was positioned at one side of the detector, by an electric field generated by a potential gradient applied to a set of wires located perpendicular to the beam direction. The electrons were multiplied due to the anode wire, which also induced a signal on cathode readout pads located on each side about 7 mm away from the anode wire. The pads had a pitch of 2.54 mm, so that the induced charge was generally distributed over several pads. The dispersive (x) position was taken to be the peak of the charge distribution on the cathode pads. The non-dispersive (y) position was calculated from the drift time obtained from the timing signal associated with the cathode

pads. The resulting position resolution was generally 0.4 mm in both the dispersive and non-dispersive dimensions [42]. In Figure 2.4 is given a schematic drawing of the components of a CRDC. The two CRDC detectors provided x and y position information at two positions along the beam axis to calculate the corresponding dispersive (afp) and non-dispersive (bfp) angles in the focal plane (fp):

$$\begin{aligned} afp &= \arctan\left[(x2 - x1)/1073\right] \\ bfp &= \arctan\left[(y2 - y1)/1073\right] \end{aligned} \tag{2.2}$$

where *x1*, *x2* were the measured x and y positions in CRDC1 *y1*, *y2* were the measured x and y positions in CRDC2, and 1073 is the distance between the two CRDCs in millimeters. The resulting angular resolution was generally $\leq$ 2 mrad [41].

2.3.2 Ionization Chamber

An ionization chamber was located in the focal plane of the S800 spectrometer to measure the energy lost by each particle. The chamber was 0.41 m thick in the z (beam) direction and was filled with P10 gas at a pressure of 300 torr. The chamber volume was divided into 16 segments by alternating cathode and anode plates oriented perpendicular to the beam direction. The plates were constructed from 70 mg/cm^2 polypropylene with 0.05 μm of aluminium evaporated on each side. The entrance and exit windows of the chamber were made of 14 mg/cm^2 Mylar with an overlay of kevlar filaments and epoxy for added strength [43]. A photograph of the 32 cathode and anode plates is depicted in Figure 2.5. Similar to the CRDCs, the particles that passed through the gas created an ionization track. The sixteen sets of anodes and cathodes were used to collect the resulting ionized electrons to obtain a cathode signal, which was proportional to the energy deposited in the gas. Each

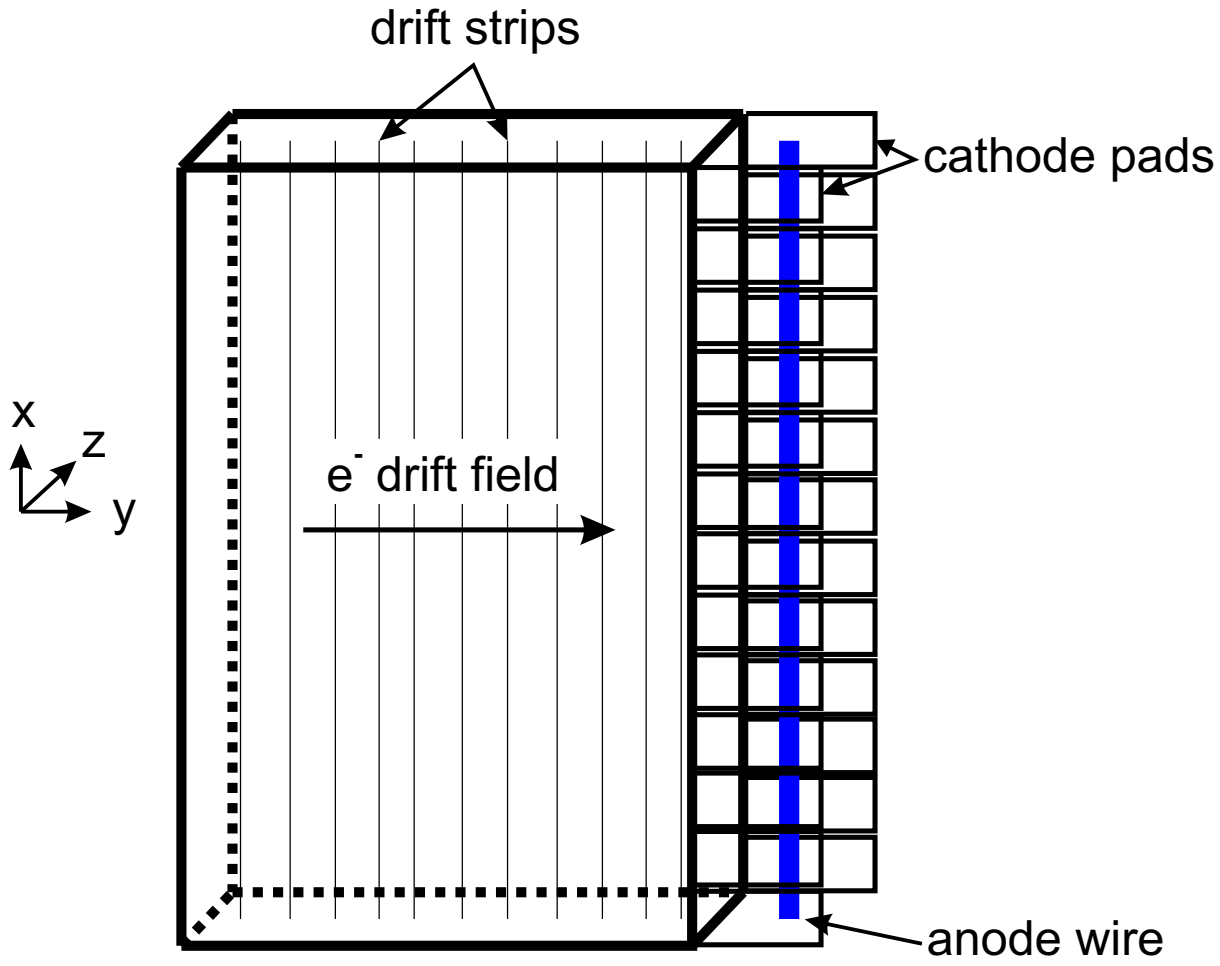

Figure 2.4: Schematic drawing of a cathode readout drift chamber (CRDC). The beam travels in the positive z-direction. Note that the components are not to scale.

Figure 2.5: Photograph of the alternating cathode and anode plates of the ionization chamber. Plates are oriented perpendicular to the beam axis.

cathode signal corresponded to the energy lost by the particle. The $-\frac{dE}{dx}$ was determined with the well-known Bethe-Bloch formula, assuming a fully-stripped ion with atomic number and velocity Z and ν in a medium with atomic number z, ionization poential I, and number density, N [44]:

$$-\frac{dE}{dx} = \frac{4\pi e^4 Z^2}{m_0 \nu^2} N z \left[\ln \frac{2 m_0 \nu^2}{I} - \ln \left(1 - \frac{\nu^2}{c^2} \right) - \frac{\nu^2}{c^2} \right]. \tag{2.3}$$

In Equation 2.3, e is the electronic charge, m_0 is the rest mass of an electron, and c is the velocity of light. The high alternating cathode-anode structure of the chamber reduced the electron drift time compared to the original design [42]. The sixteen cathodes were biased to +100 V and the signals were combined in the analysis to determine an overall energy loss value for each particle.

2.3.3 Plastic Scintillator

The detector immediately downstream of the ionization chamber was a 1-mm thick plastic scintillator. This thin scintillator was used to deduce the particle time-of-flight (TOF) when compared to a signal from a plastic scintillator upstream in the beamline. An impinging particle interacted with the electrons in the plastic, causing the atoms to become excited. When the atoms decay back to the ground state, they emit photons, which propagate through the plastic and light guides to the photomultiplier tubes (PMTs). The light from the scintillator was converted to current using PMTs at the top and bottom of the scintillator and each PMT was read out. The TOF of each particle was calculated from the average time of the two PMTs (PMT_1 and PMT_2) and the signal from the PMT at the object position in the S800 analysis line (PMT_{obj}) (which is relative to the cyclotron frequency) using the following equation:

$$TOF = \frac{PMT_1 + PMT_2}{2} - PMT_{obj}. \tag{2.4}$$

The final TOF was used to generate the master gate for the data acquisition system during the experiment.

2.3.4 Hodoscope

A new hodoscope detector was built, tested off-line, and installed prior to NSCL experiment 10501. The hodoscope consisted of 32 individual crystals made of sodium-doped cesium iodide, CsI(Na). The details of the detector design and the accompanying electronic readout are provided below. The pre-installation tests and installation into the focal plane of the S800 spectrometer are also discussed.

2.3.4.1 Hodoscope Design

The CsI(Na) hodoscope was designed to replace the thick plastic scintillators (10 and 20 cm) [42] in the focal plane of the S800 spectrometer. The most downstream detectors were used to measure the residual total kinetic energy of the particles that reached the focal plane. The new hodoscope was composed of an array of crystals, shown schematically in Figure 2.6, with the goal of improving the resolution of the total kinetic energy measurement at the S800 focal plane. The desired criteria for the new hodoscope was to be able to deduce the individual atomic charge states. Such a request dictates that an energy separation of 290 MeV be achievable, for example, at Z=31, A/q=2.325, and Bρ=3.5 Tm. Another option for measuring the total kinetic energy of the particles is silicon detectors but the large area required of the detector makes this option prohibitively expensive.

The 32 crystals of the new hodoscope were manufactured by ScintiTech [45] and were arranged in an array 8 crystals high by 4 crystals wide. Each crystal was 7.6 cm by 7.6 cm on the front face and was 5.1 cm thick. The total active area of the array was 1848 cm^2, which covers approximately the same solid angle as the CRDC detectors that are upstream of the hodoscope in the S800 focal plane. The hodoscope array was located at the most downstream location in the focal plane detector box as shown in Figure 2.3. Each CsI(Na) crystal was attached to a Hamamatsu model R1307 PMT (chosen for its optimization of the pulse-height resolution) and a mu-metal magnetic shield was placed around the PMT. The photo cathode of the PMT was a bi-alkali material with a transmission peak at 420 nm. The remaining five sides of each crystal were covered with two 150 μm thick layers of a white Teflon reflective material. This covering provided light shielding between the crystals without sacrificing the desired close packing to minimize 'dead' space between the crystals.

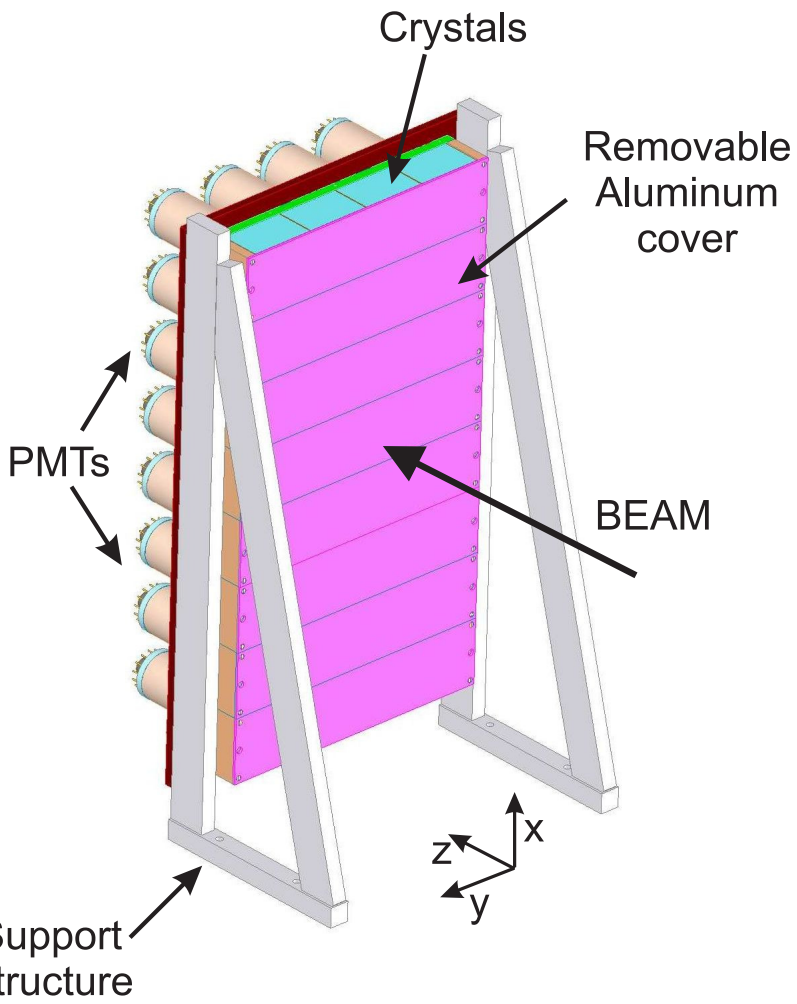

Figure 2.6: Schematic drawing of the CsI(Na) hodoscope array. The hodoscope consists of 32 crystals arranged in an eight-by-four (x-by-y) array. The numbering scheme for the detector is shown more clearly in Figure 2.13

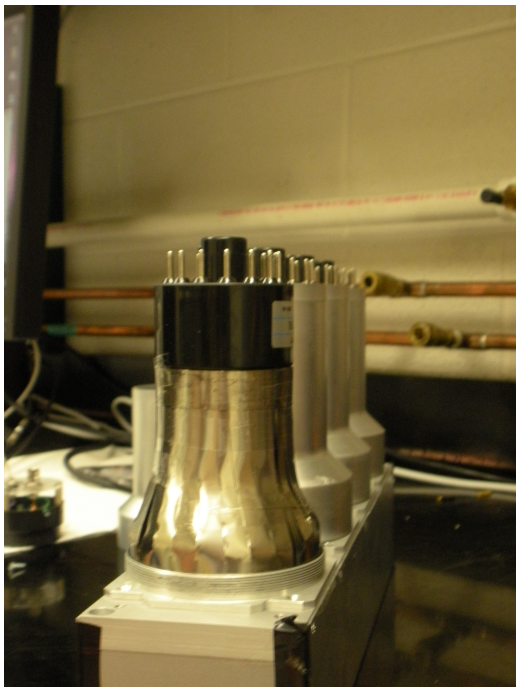

Figure 2.7: Photographs of a row of four crystals. The cover on the nearest crystal has been removed so the mu-metal magnetic shielding can be seen.

The crystals were packaged by the manufacturer in units of four crystals, shown in Figure 2.7, to keep the weight manageable and to make possible future maintenance or replacement of a failed crystal a relatively simple process.

2.3.4.2 Hodoscope Testing and Installation

Prior to installation into the focal plane of the S800 spectrometer, each crystal was tested by observing the response to the 662 keV γ ray from an uncollimated ^{137}Cs source. This testing provided important information on each crystal and corresponding PMT including proper operation and γ ray energy resolution of each crystal was as specified in the manufacturing agreement. During the tests, the ^{137}Cs source was placed 25 cm from the center of the front face and then from the side face of each crystal, as shown in Figure 2.8. A

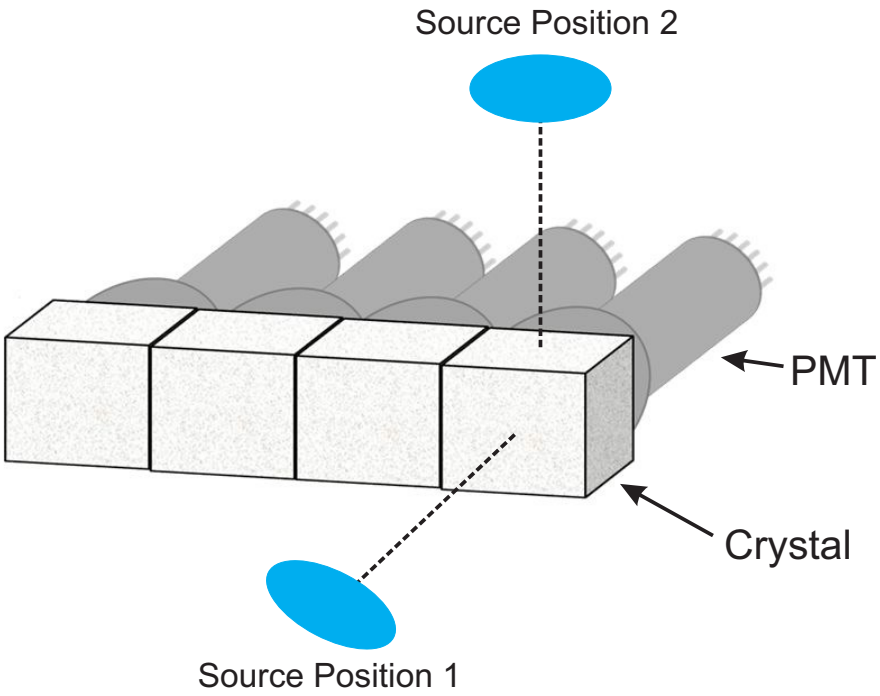

Figure 2.8: Relative orientation of the γ ray source during of the test set-up for each crystal. The source was placed at two positions, labelled 1 and 2, to verify each crystal's functionality and γ ray energy resolution.

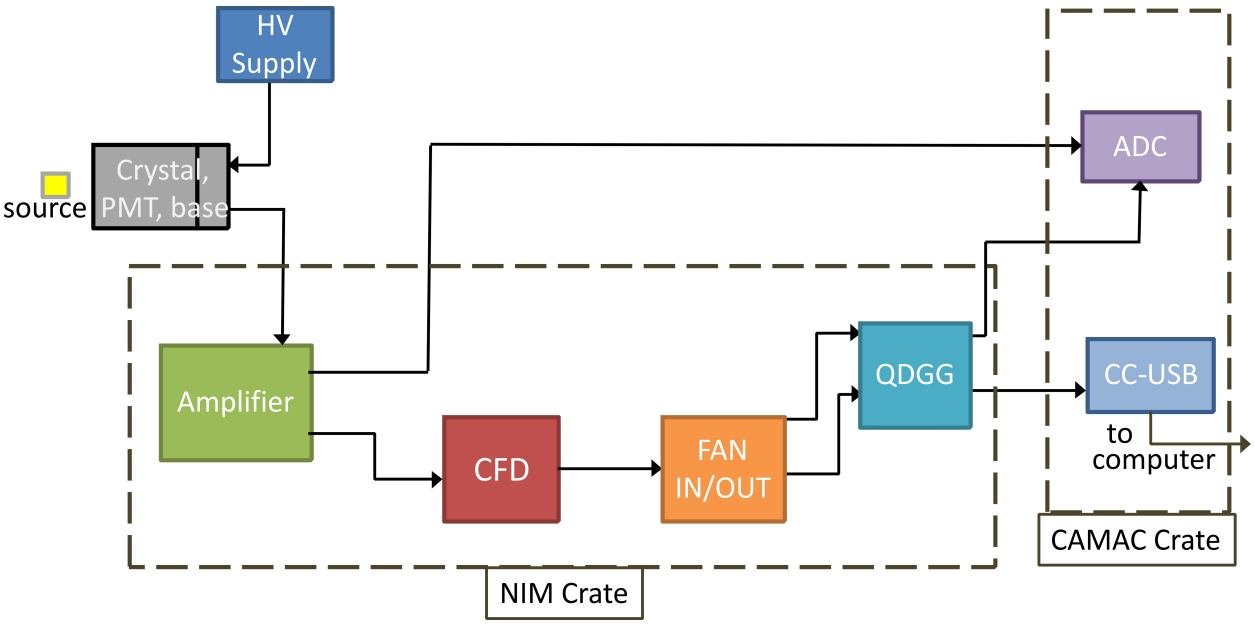

Figure 2.9: Schematic diagram of the electronics used in test set-up for each crystal.

schematic diagram of the electronics used in the set-up for the detector acceptance tests is diagrammed in Figure 2.9. A Canberra model 13002D high voltage supply was used to power the PMTs, which were operated at +800 V. The signal from the crystal induced by a 662 keV γ ray interaction was processed first by a shaping amplifier, TC model 241S, with a 6.0 μs shaping time. The fast signal from the amplifier was used as an input to a constant fraction discriminator (CFD), Ortec model 473, after a 50 ns delay cable and created a trigger for the conversion of the slow signal. The NIM output logic signal from the CFD next went to a FAN IN/OUT module, where the signal was split into two signals and sent to two different inputs of a quad delay-and-gate generator (QDGG). One of the QDGG gates was set to a width of 10 μs wide and was used to gate the analogue to digital converter (ADC) module, that accepted the slow signal from the shaping amplifier. The second QDGG gate was set to 100 ns wide and was sent to the USB (CC-USB) CAMAC crate controller to trigger data acquisition. The γ spectra were collected for 10 minutes for each source location for each crystal. The resulting spectra were analyzed to deduce the peak resolution, R, at 662 keV using the following definition:

$$R = \frac{FWHM}{x_0}, \tag{2.5}$$

where x_O is the peak position in the spectrum and FWHM is the full width of the distribution at one-half the height of the peak. Results from the γ ray testing of crystal 23 is shown in Figure 2.10. All the deduced resolution values are reported in Figure 2.11. The average energy resolution of the front face of the hodoscope was found to be 7.09±0.10 % and side face had a similar average energy resolution of 7.13±0.16 %. These values are better than the specifications requested from the manufacturer and agreed with the energy resolution test results performed by the manufacturer before shipment.

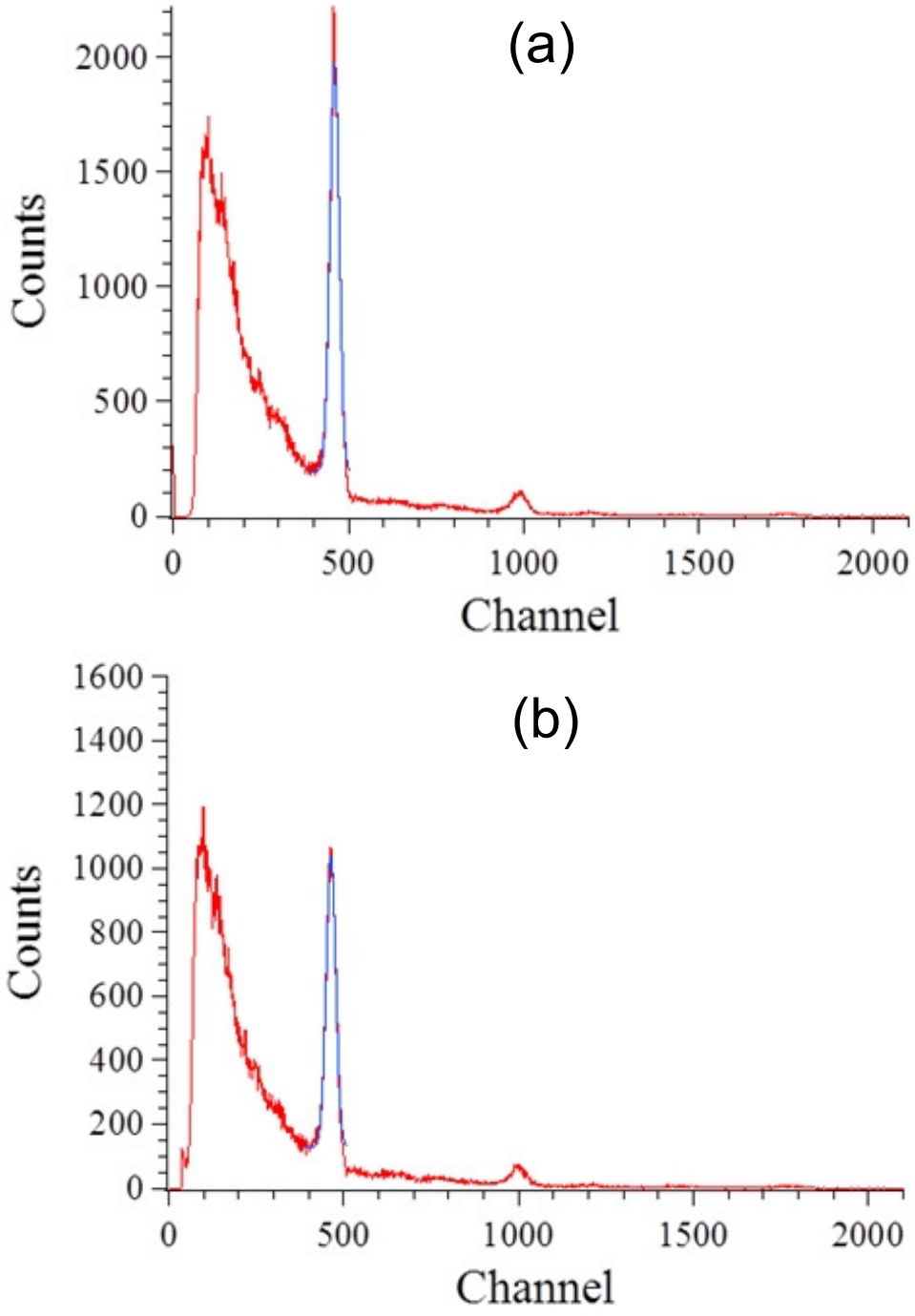

Figure 2.10: Raw spectra from the γ ray testing of the crystal 23 using a 662keV γ ray. (a) front face and (b) side face.

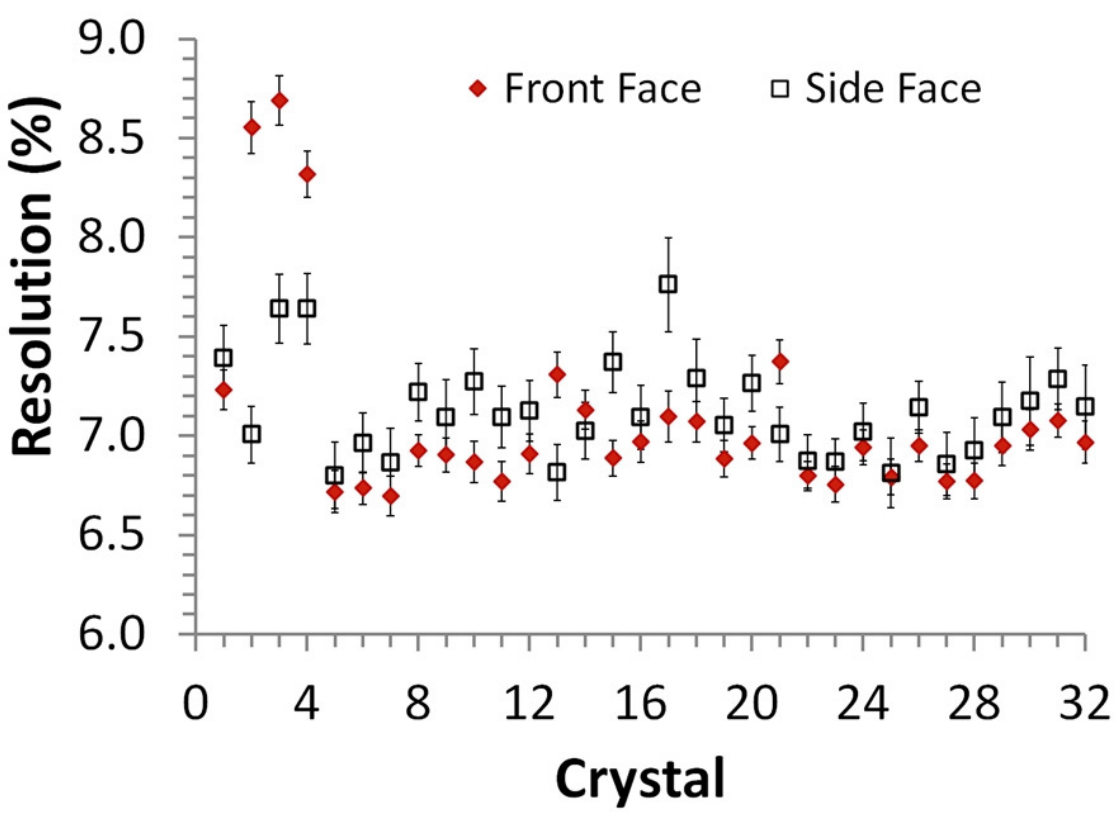

Figure 2.11: Energy resolution for a 662 keV γ ray for each of the 32 crystals in the hodoscope. Resolution values obtained for both front (diamonds) and side (squares) faces are given. See the text for additional details.

Prior to installation of the crystal array into the focal plane of the S800 spectrometer, the support structure and all cabling was evaluated for operation in vacuum. The high voltage divider base of the PMT and the adjoining magnetic shielding had 0.25-inch holes drilled in them to be sure that the high voltage connections were not at a pressure that could induce sparking or discharge and allow for out-gassing. Cables for both the high voltage supply and outgoing detector signal were made with an outer Teflon covering to prevent hardening of the cable, a common occurrence for cables under vacuum. Finally, the full array was assembled on its support structure (shown in Figure 2.3) before installation in the focal plane to ensure proper alignment of all the crystals and supporting components.

The final assembly of the array in the most downstream position in the S800 focal plane was initiated by placing the support structure in position 14.3 cm downstream of the fast timing scintillator. Next, the crystals were mounted row-by-row, starting with the bottom row and working upwards. An aluminium cover of thickness 812.8 μm was placed over the entire crystal surface to ensure the crystals did not shift when the array was tilted at the 30 degree operating angle of the focal plane. This cover was eventually removed after the current experiment after verifying that the crystals did not shift when inclined at 30 degrees. In Figure 2.12 are shown photographs of the front of the hodoscope with and without the aluminium cover, as well as the back of the hodoscope, as the device is currently installed in the focal plane. A γ ray source was placed in front of the aluminium cover and the cable connections were verified by monitoring the hodoscope output signals. The signal from each crystal's PMT served as an input to a Caen model N568B shaping amplifier. The slow signal from the amplifier was input to a Phillips 7164H 12-bit ADC. Each crystal was powered by a high voltage supply, Wiener model Iseg EDS 201 30p 504. The voltage values were set based

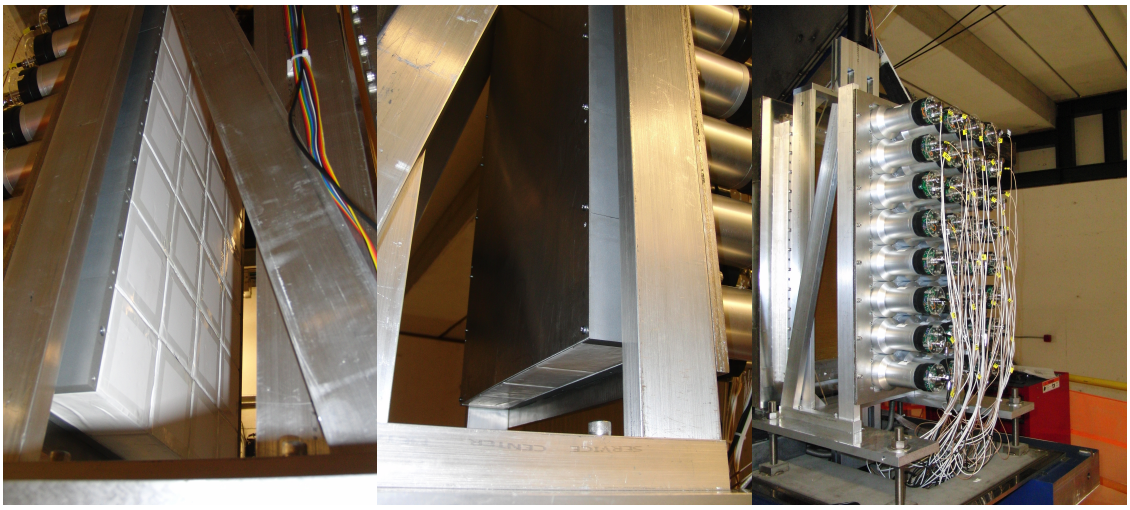

(a) (b) (c)

Figure 2.12: Photographs of the front face (a) without and with (b) aluminium cover and (c) back faces of the hodoscope as installed in the S800 focal plane.

Table 2.1: Typical matched voltage settings for the hodoscope crystals. The values shown are for detection $^{76}Ge^{32+}$ beam particles and are representative of all voltage values used in experiment 10501.

Crystal	Voltage [V]	Crystal	Voltage [V]	Crystal	Voltage [V]	Crystal	Voltage [V]
1	330	9	330	17	350	25	320
2	310	10	350	18	350	26	310
3	350	11	340	19	360	27	350
4	350	12	330	20	300	28	350
5	340	13	350	21	340	29	350
6	310	14	360	22	350	30	330
7	370	15	340	23	360	31	310
8	320	16	320	24	380	32	330

on the outgoing signal's position in the raw ADC spectrum with the general goal that all the signals were approximately matched in pulse height. An example of the applied voltage values, after gain-matching to a 'middle' position in the ADC (between 0 and 4096), for the hodoscope crystals is shown in Table 2.1 for the implantation of $^{76}Ge^{32+}$ beam particles.

2.4 Target Position Mapping

A powerful characteristic of the S800 spectrometer and focal plane is the ability to relate the position and angular measurements taken in the focal plane by the CRDC detectors to corresponding position and angle values at the target position. The reconstruction of the trajectory of a particle through the spectrometer is accomplished using a inverted matrix or 'inverse map' of the dipole magnets and quadrupole magnets. The inverted matrix, shown to first order in Equation 2.6, used the measurements of the magnetic fields of dipole magnets to relate the kinematic parameters of position and angle from the focal plane back to the target position. The COSY INFINITY code [46] was used to calculate the inverse map up to fifth order and includes correction terms for magnetic field aberrations.

$$(ata, yta, bta, dta) = \begin{pmatrix} ata|xfp & ata|yfp & ata|afp & ata|bfp \\ yta|xfp & yta|yfp & yta|afp & yta|bfp \\ bta|xfp & bta|yfp & bta|afp & bta|bfp \\ dta|xfp & dta|yfp & dta|afp & dta|bfp \end{pmatrix} \begin{pmatrix} xfp \\ yfp \\ afp \\ bfp \end{pmatrix} \tag{2.6}$$

Equation 2.6 is the matrix equation relating initial and final kinematic parameters on an event-by-event basis. The *-fp* variables refer to the focal plane or final position, *-ta* variables refer to the target or initial position, x- are dispersive positions, a- are dispersive angles, y- are non-dispersive positions, b- are non-dispersive angles, and dta is the fractional energy between the energy of the event, E, and the energy of the particle traversing the central trajectory of the spectrometer, E_O:

$$dta = \frac{E - E_O}{E_O} \tag{2.7}$$

where the central energy, E_0, is calculated using the following equation:

$$E_O = (mass)\,(amu)\left(\sqrt{1+\left[\left(\frac{charge}{mass}\right)\left(\frac{B\rho_O}{3.107}\right)\right]^2}-1\right). \tag{2.8}$$

Here, *mass* and *charge* are the mass (A) and charge (Z) of the particle along the central trajectory, $amu = 931.5$ MeV is the atomic mass unit in MeV, $B\rho_O$ is the measured magnetic rigidity along the central trajectory, 3.107 is a unit conversion factor. The four kinematic parameters *ata*, *yta*, *bta*, and *dta*, were then used to calculate the physical quantities of momentum, energy, and scattering angle.

2.5 Experimental Running Conditions

The 24 hours of beam-on-target time was divided into three segments with different conditions; the primary ^{76}Ge beam was transported to the S800 focal plane, the ^{76}Ge beam was impinged on 99.8 mg/cm^2 beryllium and 50.2 mg/cm^2 gold targets located at the S800 target position.

During the first stage of the experiment, the primary beam was tuned through the spectrometer and into the focal plane detectors. The goal was to observe the response of each of the 32 crystals of the hodoscope to the ^{76}Ge beam particles. To achieve this goal, the current exciting the quadrupole magnet at the entrance of the spectrometer was set to defocus the beam by reducing the current to near zero. This defocusing step, along with the step-wise variation of the dipole magnetic rigidity values, shown in Table 2.2, allowed for the primary beam to implant in each of the 32 detectors of the hodoscope array. The average beam intensity on the plastic scintillator located at the object position in the S800 analysis line was limited to 1 kHz during these measurements to minimize dead time of the focal

plane detectors. For reference, the maximum available beam rate from the CCF for the ^{76}Ge beam was 156 GHz. The fact that the beam intensity could be easily controlled was exploited during this experiment to probe the rate capabilities of the hodoscope crystals. Data were briefly collected with the hodoscope elements with incident ^{76}Ge beam rates of 1, 2, 6, and 20 kHz. The normal beam rate during the experiment was approximately 1 kHz. Some of the results are presented in Figure 2.13, obtained with the different Bρ settings overlayed on a grid representing the 2D crystals matrix. Data with the ^{76}Ge beam were collected from all 32 crystals for detector characterization which will be described in Chapter 3.

Table 2.2: Magnetic rigidity settings of the S800 spectrometer for ^{76}Ge beam into the hodoscope.

Run	Bρ [Tm]	Run	Bρ [Tm]
1	4.1376	8	3.9956
2	4.1170	9	3.9757
3	4.0965	10	3.9559
4	4.0761	11	3.9363
5	4.0558	12	3.9167
6	4.0357	13	3.8972

The rest of the experimental time was used to react the ^{76}Ge beam in the two different reaction targets: ^{9}Be and ^{197}Au. Five S800 magnetic rigidity settings, listed in Table 2.3, were used to collect data to obtain reaction products in a total momentum range of 12.5%. The five Bρ values were chosen to ensure overlap of each momentum distribution in the different settings. Chapter 3 focuses on detector calibrations, the analysis methods used to characterize the hodoscope array, and obtain the fragment momentum distributions from the projectile fragmentation process described in Chapter 1.

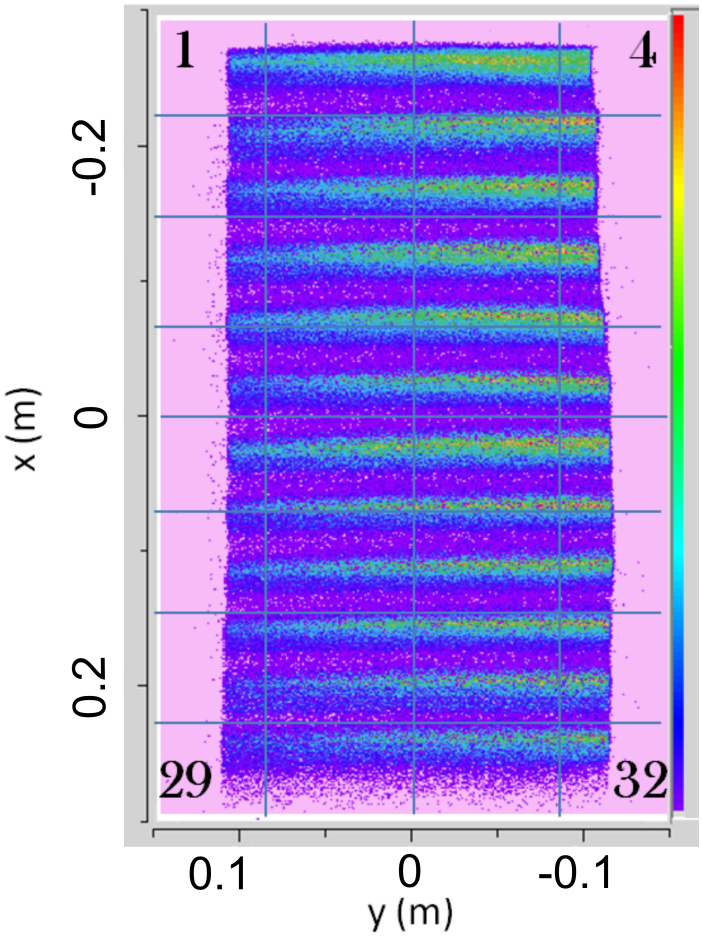

Figure 2.13: Image of the hodoscope array face with data from the Ge beam data obtained with 13 different S800 Bρ settings. The numbering scheme of the array is indicated by the numbered corner crystals. Color online indicates the number of Ge ions deposited in each crystal.

Table 2.3: Magnetic rigidity settings of the S800 spectrometer used to observe reaction products with the beryllium and gold targets.

	Be target	Au Target
Setting	Bρ [Tm]	Bρ [Tm]
1	3.8085	3.8840
2	3.7133	3.7869
3	3.6181	3.6922
4	3.5229	3.5927
5	3.4276	3.4956

Chapter 3

Data Analysis

This chapter focuses on the conversion of the experimental measurements into physical quantities of interest such as the kinetic energy and momentum of the observed ions. The analysis procedures included detector calibrations, particle identification, characterization of the hodoscope energy measurement and atomic charge-state resolution capabilities, and the reconstruction of the vector components of the linear momentum distributions of produced fragments. The tools utilized to accomplish this analysis were a C++ based program, SpecTcl [47], and the commercial program Igor Pro [48].

3.1 Detector Calibrations

Each detector used during the experiment required calibration prior to evaluation of the collected data. This section focuses on the transformations applied to the data recorded from the CRDCs, ionization chamber, time-of-flight plastic scintillators, and the hodoscope.

The CRDC tracking detectors required three separate calibrations. The first transformation for the CRDC detector data was a pedestal subtraction procedure which identified the

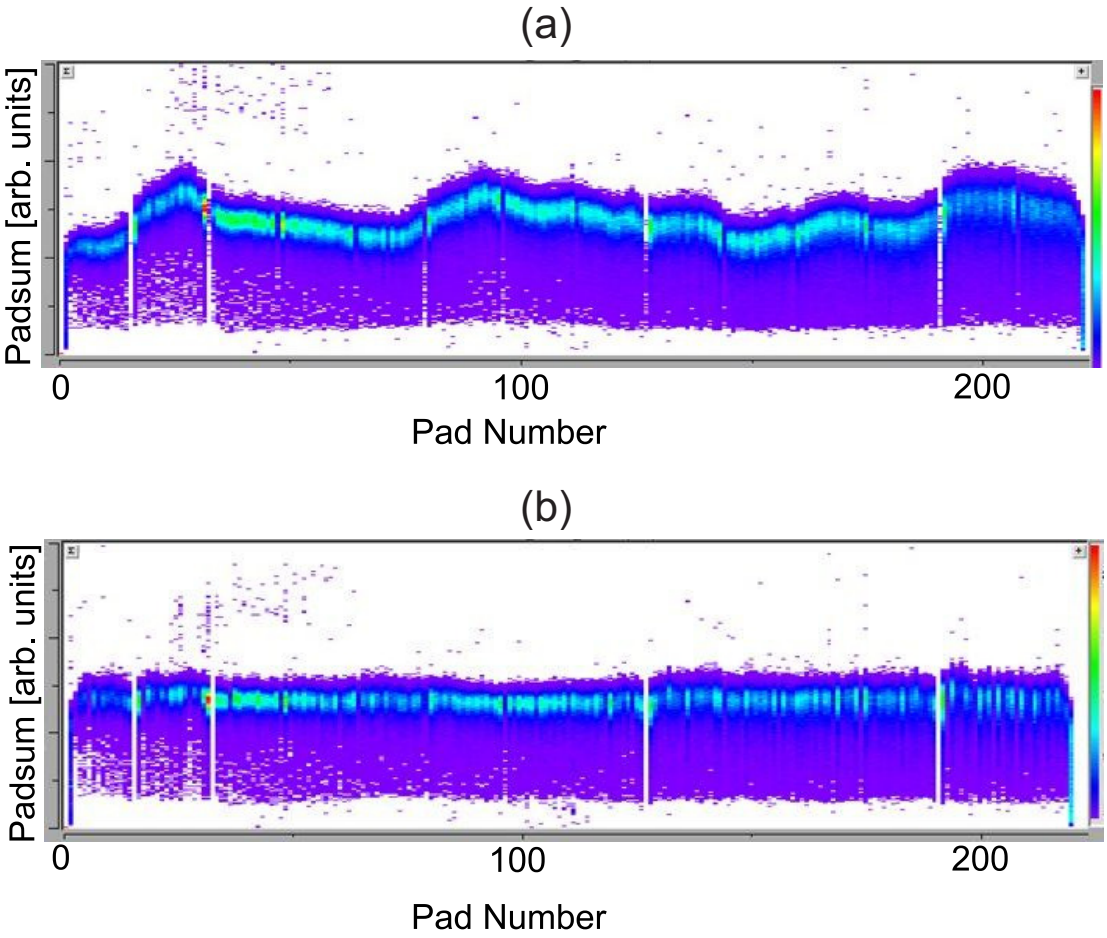

Figure 3.1: CRDC1 padsum calibration. (a) raw and (b) calibrated padsum values obtained for all active pads of CRDC1.

channel offset associated with noise. The electronic pedestal (ADC channel without data) was established for each channel by collecting CRDC data while running the CRDCs at the experimental settings without any charged particles incident on the detectors. The baseline or pedestal values were recorded and subsequently subtracted from experimental data. The second correction step to the data from the CRDC detectors was a gain-matching. Gain matching of the 224 charge collection pads in each CRDC was important to ensure the resulting calculations of velocity and momentum were accurate. The raw and calibrated values of the "padsum", a summation of all active collection pads, are shown in Figure 3.1. Several dead pads were identified in each detector where a zero or very low padsum value

was registered in the raw spectra, and these pads were removed from further analysis. The middle pad, pad 112, was chosen as the reference pad and the padsum value for this pad was normalized to one. All other active pad slopes were in reference to the middle pad such that each pad had approximately the same padsum value for a monoenergetic signal. The result of the normalization is depicted in Figure 3.1. The third data transformation for the CRDC data relied on a position calibration obtained with a mask. In Figure 3.2 is shown the mechanical layout of the mask that was placed in front of each CRDC detector. The mask, made of 0.4336-inch thick tungsten [49], prohibits particles from reaching the tracking detectors except through the holes, represented by '+' in Figure 3.2, and vertical slits, which have well-known x and y positions. In Figure 3.3 the corrected position spectra from the CRDC1 tracking detector, using the position mask is shown. The data with the mask was used to establish the slope and offset values for linear transformations of the raw position measurements in both dimensions.

The ionization chamber calibration involved gain-matching the 16 ADC readout channels. The raw peak position of each channel was analyzed using data for the ^{76}Ge primary beam particles implanted directly into the S800 focal plane. Channel zero was removed from further analysis as an abnormally low signal was registered in this channel. The remaining 15 channels were arbitrarily normalized to the values observed in channel three. The final calibrated spectrum of the ionization chamber is shown in Figure 3.4.

The time-of-flight (TOF) measured between the object scintillator located at the entrance of the S800 analysis beamline and the focal plane scintillator has known correlations with the dispersive position and angle of particles that reach the focal plane. The inherent path-length variation of particles travelling through the spectrometer results in a corresponding width in

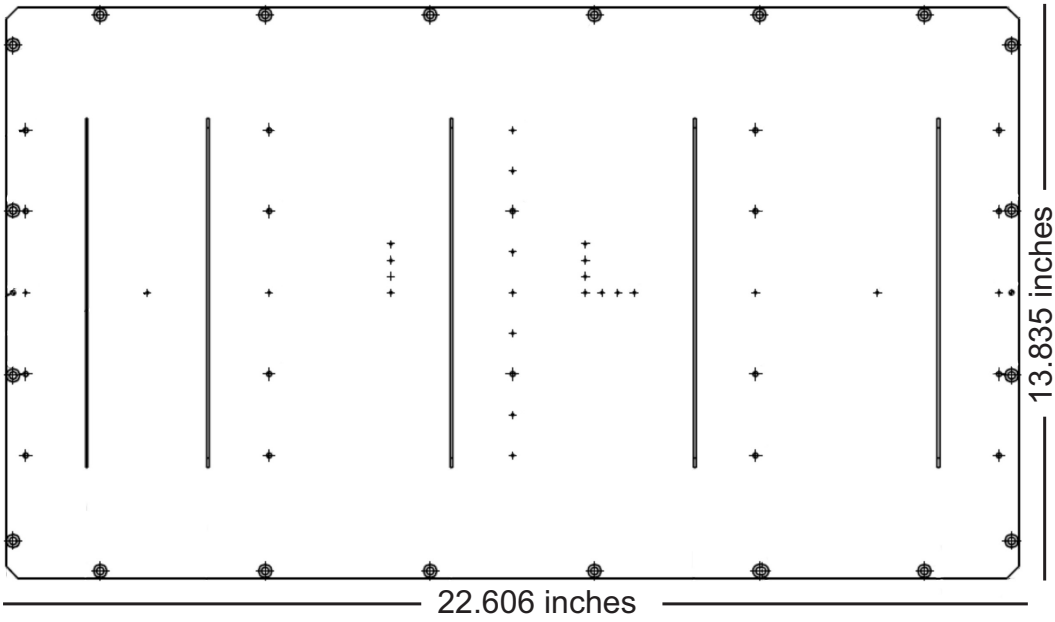

Figure 3.2: Position mask for CRDC position calibrations. The slots and holes (shown as '+'s) allow particles to pass through and provide x and y position references.

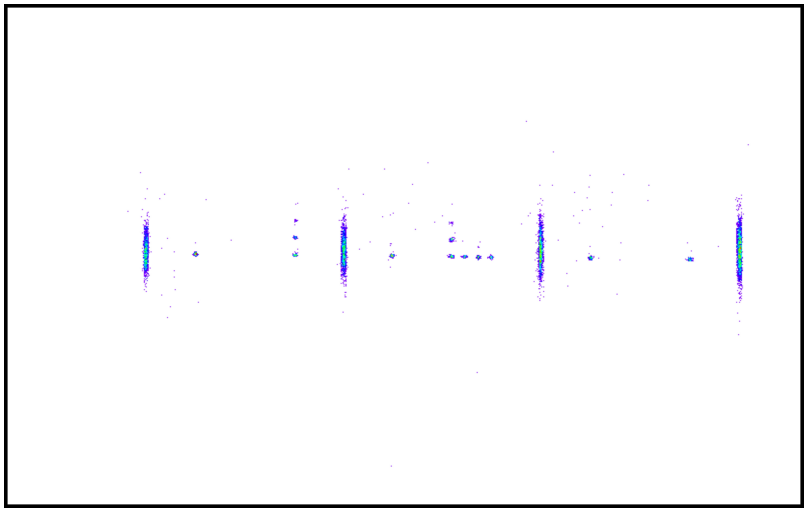

Figure 3.3: CRDC1 x-y spectrum observed with position mask in place.

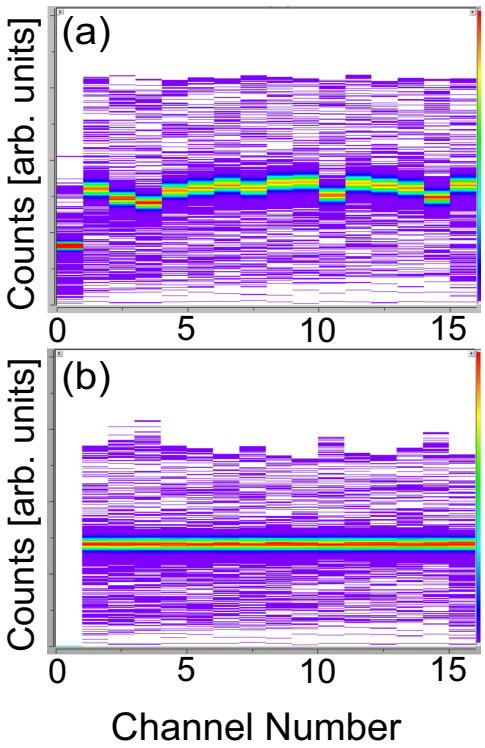

Figure 3.4: Results of the ionization chamber calibration. (a) Uncalibrated individual spectra observed for ^{76}Ge particles. (b) Calibrated spectra for the same particles.

the TOF distribution for identical particles due to differences in velocities and trajectories. The TOF signal was therefore analyzed as a function of both the position and angle at the focal plane and the correlations with both dimensions were removed in a transformed or "corrected" TOF.

Angular dependencies of the incoming beam at the target position were also examined. The inverse map used to calculate the position and angle of the detected particles at the target position assumed the incoming beam was normal to the target. The average measured position and angle of the beam at the target was used to define the zero degree position in the spectrometer.

The final calibration prior to evaluation of the experimental data was the evaluation of the hodoscope crystal dimensions and positions in terms of the measured CRDC positions.

Dispersive and non-dispersive position data from CRDC1 detector were combined with information from the mechanical drawings of the focal plane to determine the CRDC dimensions of each crystal. The raw signal of each hodoscope crystal was used as a gate for the x and y information from CRDC1 to determine the crystal's physical extent. The gated x and y position map from CRDC1 was then extrapolated 2.048 m in the beam (z) direction to the surface of the hodoscope based on the mechanical drawings. In Figure 3.5 is a comparison of the apparent dimensions of each crystal in the x-y plane with an overlying grid. Particles observed in each crystal are displayed individually in the 32 panels shown in Figure 3.5. The dimensions of each crystal were measured to be 8.32 cm in the x-direction and 7.90 cm in the y-direction. The 300 μm Teflon covering and the physical gaps in the crystals are reflected in the x-dimension being slightly larger than the y-dimension. The total area of the crystals extended beyond the acceptance of the spectrometer.

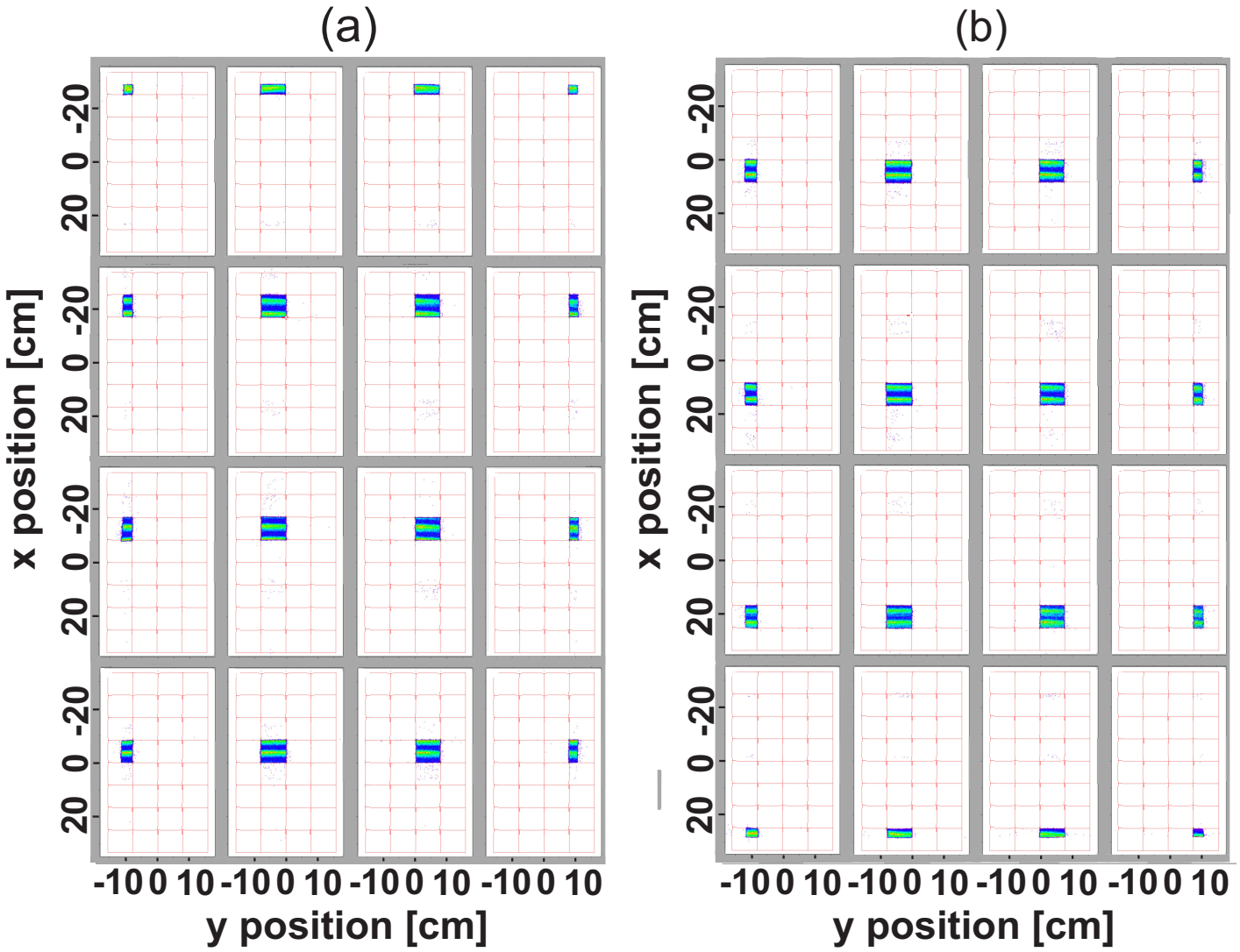

Figure 3.5: Calibrated hodoscope crystal positions in the x-y plane compared to the overlying grid that corresponds to the physical crystal locations. (a) CRDC position calculated for particles striking crystals 1 - 16 and (b) crystals 17 - 32, see the text for an explanation.

3.2 Particle Identification

Corrections to the TOF and energy loss signals from the scintillators and ionization chamber were necessary prior to identification of the particles in the focal plane. Particle identification (PID) plots were then produced as two-dimensional spectra, combining the corrected TOF and energy loss that were used to identify particles. The corrected TOF was also combined with the measured magnetic rigidity of the spectrometer to provide identification of the A/Q of the particles, following equation 1.7, and the energy loss was used to deduce the Z value, as defined in equation 2.2, of each particle. Examples of the PID plots generated as part of the analysis procedure are shown in Figure 3.6. The fragments produced by reaction of the ^{76}Ge beam with each target, Be and Au, for each of the five magnetic rigidities fall into individual oval-shaped groups. The vertical dashed lines overlaying each PID spectra give the N/Z ratios of the fragments. Identical N/Z values in the different PID illustrate the overlap in fragment production in the different spectrometer settings.

3.3 Hodoscope Characterization

The characterization of the hodoscope as a tool for particle analysis required the determination of both the signal output as a function of position and energy resolution capabilities of the detector. The following subsections detail the analysis steps carried out to measure the energy resolution and the response of each crystal to implanted charged particles. The resulting ability to differentiate atomic charge-states of incoming particles will be detailed in Chapter 4.

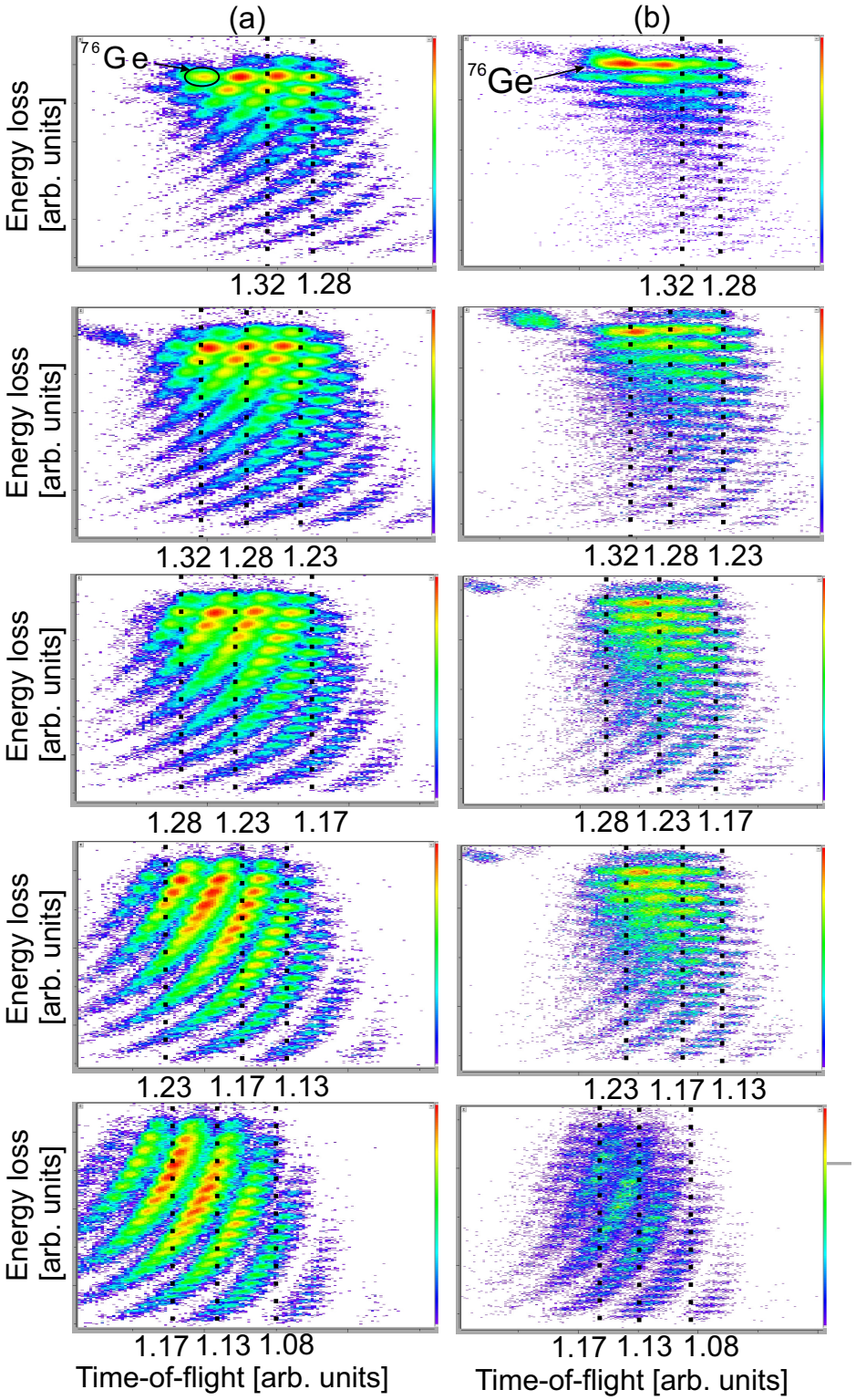

Figure 3.6: Particle identification plots for fragments produced using beryllium (a) and gold (b) targets. The location of the ^{76}Ge beam is indicated with an oval and the N/Z ratios are given with vertical dashed lines that illustrate the progression of the magnetic rigidity of the S800 from the top frame to the bottom frame.

3.3.1 Light and Energy Resolutions

Sodium-doped cesium iodide [CsI(Na)] crystals have been used for decades as scintillation detectors for γ rays and charged particles [44]. While similar to thallium-doped cesium iodide [CsI(Tl)] in regards to the inorganic scintillation properties, CsI(Na) crystals are known to produce light in a two-step decay process and have a light output shifted towards the ultraviolet region compared to the thallium-doped version [44]. The total amount of light produced by the crystal and transmitted to a PMT represents the response of an individual crystal to the energy deposited by a stopping ion. This process assumes the amplification of the signal by the PMT and electronic analysis consisting of a shaping amplifier followed by a peak-sensing ADC is well understood. The raw signals from the crystals in response to stopping of nearly monoenergetic ^{76}Ge beam particles were used to determine both the light and energy resolution of each crystal. Prior to calculation of the raw light peak associated with the ^{76}Ge beam particles, the raw histograms from the ADC were analyzed to determine channel values that corresponded to the first channel above the noise, labeled the minimum channel. Table 3.1 contains a listing of the minimum channel value or pedestal (out of 4096 available channels) for all 32 crystals. A multiplicity signal was created that counted the number of crystals 'hit' during one event. Data used for all further analysis were restricted to events with a multiplicity of one.

An important feature of the histograms shown in Figure 3.8 are the smaller peaks at high channel values on the side of the main peak. One expects that the monoenergetic beam particles should produce a single peak. The presence of a second peak, although reduced in intensity, was unexpected and subsequently was excluded from the data during evaluation of the resolution. The source of the unexpected peak was investigated by taking advantage

Table 3.1: ADC channel minima and linear slope calibration in MeV/channel.

Crystal	Min. Channel	Linear Slope	Crystal	Min. Channel	Linear Slope
1	40	4.18	17	50	4.47
2	40	4.32	18	50	4.36
3	40	4.17	19	50	4.29
4	40	3.96	20	50	4.40
5	40	4.28	21	40	4.23
6	40	4.38	22	40	4.14
7	50	4.22	23	40	4.34
8	40	4.04	24	50	4.48
9	40	4.45	25	30	4.34
10	50	4.29	26	50	4.34
11	40	4.41	27	30	4.35
12	40	4.24	28	30	4.09
13	50	4.33	29	30	4.36
14	50	4.54	30	30	4.40
15	50	4.54	31	30	4.40
16	80	4.15	32	20	4.47

of the high resolution position information from the CRDC detectors to map the surface of each crystal. A correlation between the raw light signal from a crystal and the crystal position was found. The secondary peak at higher channel value and lower in intensity originated from particle interactions at the edges of the crystal. Illustrated in Figure 3.7 is a correlation between the raw signal from a crystal, impinged by a monoenergetic beam, versus the x and y dimensions. The x and y dimensions shown in Figure 3.7 cover the full height and width of the crystal. The portion of each dimension that corresponds to the small peak is approximately 2 mm on each edge or 5% of the total height or width of the crystal. The transition between the edge region and the rest of the crystal appears to be sharp, suggesting the surfaces of the crystal were prepared differently or possibly have a different crystal structure from the bulk of the crystal material. The correlation could be corrected through calibration procedures in future data sets collected using the hodoscope,

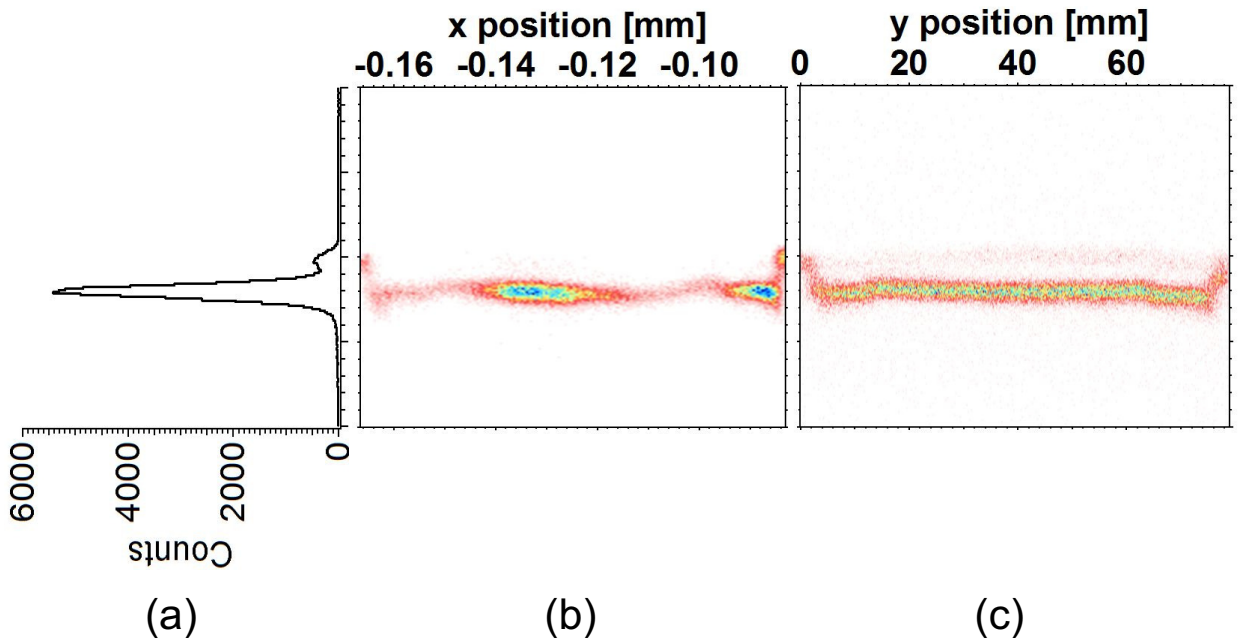

Figure 3.7: Correlation between (a) raw light signal on the vertical axis and (b) x and (c) y dimensions of a hodoscope crystal.

although in the present work particles that struck the edges of the crystals were rejected in the off-line analysis procedure.

3.3.2 Crystal Response Function

An initial analysis of the crystal response produced a linear correlation between the light output of the crystal and the deposition of nearly monoenergetic ^{76}Ge beam particles into the crystals. This response was used to construct a first-order energy calibration of the crystals, assuming that zero energy deposition is equal to zero light output. The energy deposited into a crystal by the beam was calculated from the measured position of the beam in the dispersive direction and the Bρ setting of the spectrometer. Using these values, along with relativistic kinematics, the kinetic beam energy was calculated to be 9.78 GeV. The energy width of the beam was measured to be 0.152 % at the Image2 location of the A1900.

The detectors upstream of the hodoscope as well as the aluminium sheet placed in front of the hodoscope, degraded the beam energy prior to implantation in the hodoscope elements. The calculated energy loss was 2.17 GeV (with negligible energy straggling), resulting in a final kinetic energy of 7.61 GeV deposited into each hodoscope crystal. The implanted beam energy has a corresponding range of ≈3.3mm in the crystal and a photon production of ≈3x10^5 per MeV (using results from [50]). A linear slope value in GeV/channel was deduced for each crystal using the raw light peak mean value, <x>, and calculated beam kinetic energy value of 7.61 GeV and are given in Table 3.1. In Figure 3.8 the raw light and corresponding energy histograms of two crystals in the hodoscope using the linear calibration is displayed.

However, the response of the hodoscope crystals to the incident charged particles will also depend on the particle mass and nuclear charge, in addition to particle energy. In the present work, the wide range of fragments produced by reaction of the ^{76}Ge beam in the ^{9}Be target was used to characterize the crystal response as a function of energy, mass, and nuclear charge similar to previous studies of scintillation crystals [50–57].

Before an appropriate response function for the hodoscope crystals was determined, each fragment species deposited in a particular crystal must be identified. To ensure implanted particles were properly identified, a gate in momentum space, i.e. focal plane position, was generated that matched the physical dimension of each crystal. The 8.32-mm dimension of a crystal in the dispersive direction corresponded to a 0.84% slice in Bρ, which was then applied to the PID spectra for the fragments produced when the ^{76}Ge beam was incident on the ^{9}Be. Example PID plots with the appropriate Bρ gate for crystal number ten are shown in Figure 3.9. The number of fragments species that satisfy the selection criteria was

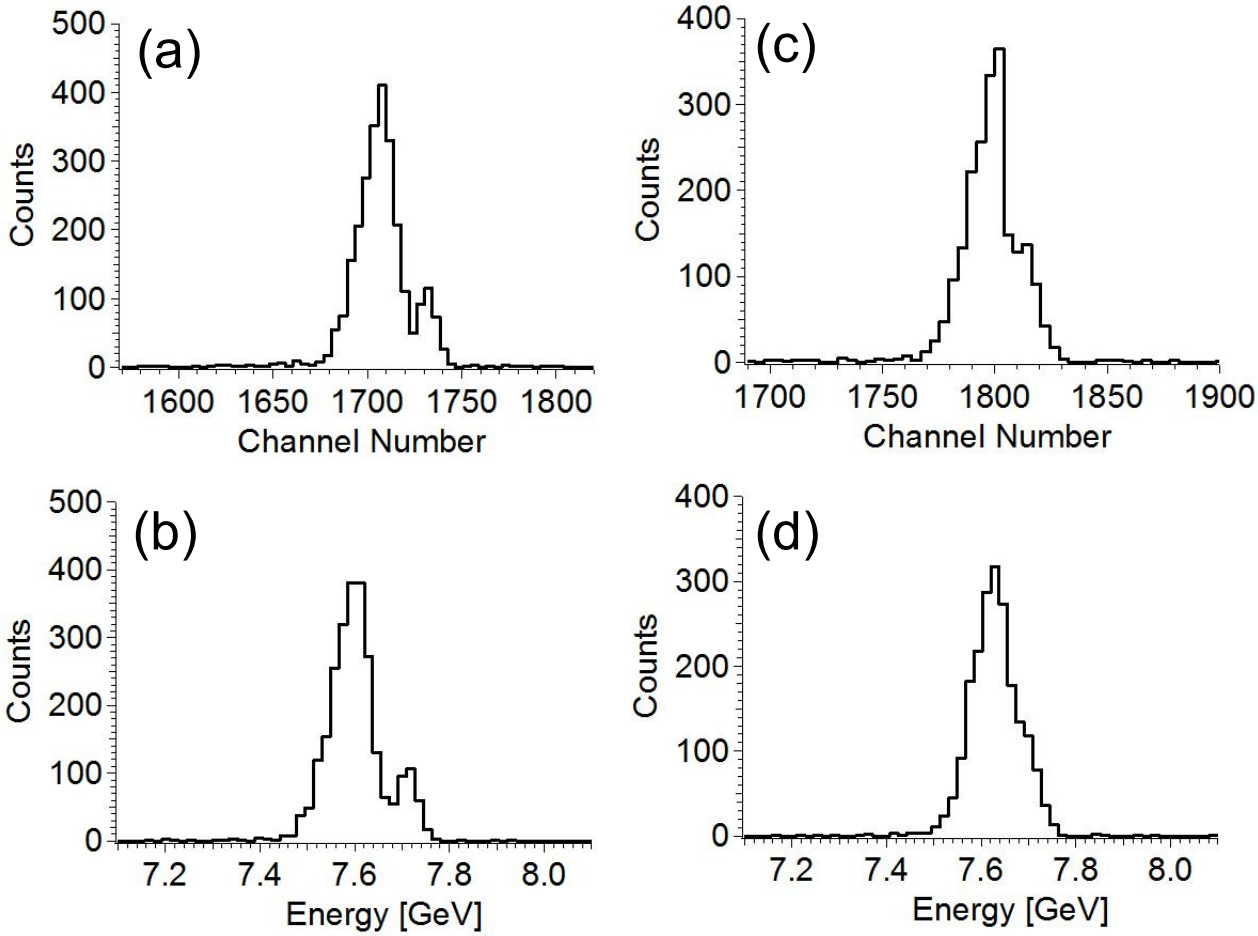

Figure 3.8: Part of the linear energy calibrations of two crystals. Similarly, raw light (a) and calculated energy (c) histograms of crystal 9. Raw light (b) and energy (d) histograms of crystal 12.

significantly reduced based on the slice in Bρ associated with the dispersive dimension of each crystal. A set of fragment species were selected for the next step of the gating process and a gate for each selected fragment was created on the PID figure. Events satisfying the two gating criteria were then taken to be the raw light output associated with one specific energy, mass, and nuclear charge (E,A,Z). Sixty different fragment species were analysed in a similar manner, and the light output from each crystal was recorded for its peak value. The final component needed to determine the response of a crystal was a calculation of each fragment's energy deposition into the crystal. LISE++ [58] was used to calculate the total kinetic energy (TKE) for each fragment at the surface of the hodoscope acccounting for energy losses in all upstream detectors. The Bρ value corresponding to the center of the crystal was calculated and used along with the fragment mass and charge values to deduce the TKE using the following relation:

$$TKE = \frac{[(B\rho)q]^2}{2m} \tag{3.1}$$

where TKE is the total energy of the particle, $B\rho$ is the magnetic rigidity, q is the charge of the fragment (set equal to Z), and m is the mass of the fragment. In Table 3.2 are listed the fragments used in the analysis of the response function of crystal number ten. Twenty fragments were selected that were well separated in each PID spectrum are shown in Figure 3.9. Note that some fragment species are listed more than once in Table 3.2. The repetition of fragment species is due to S800 magnetic rigidity values and the overlapping momentum distributions, which allowed for some fragment species to be probed multiple times.

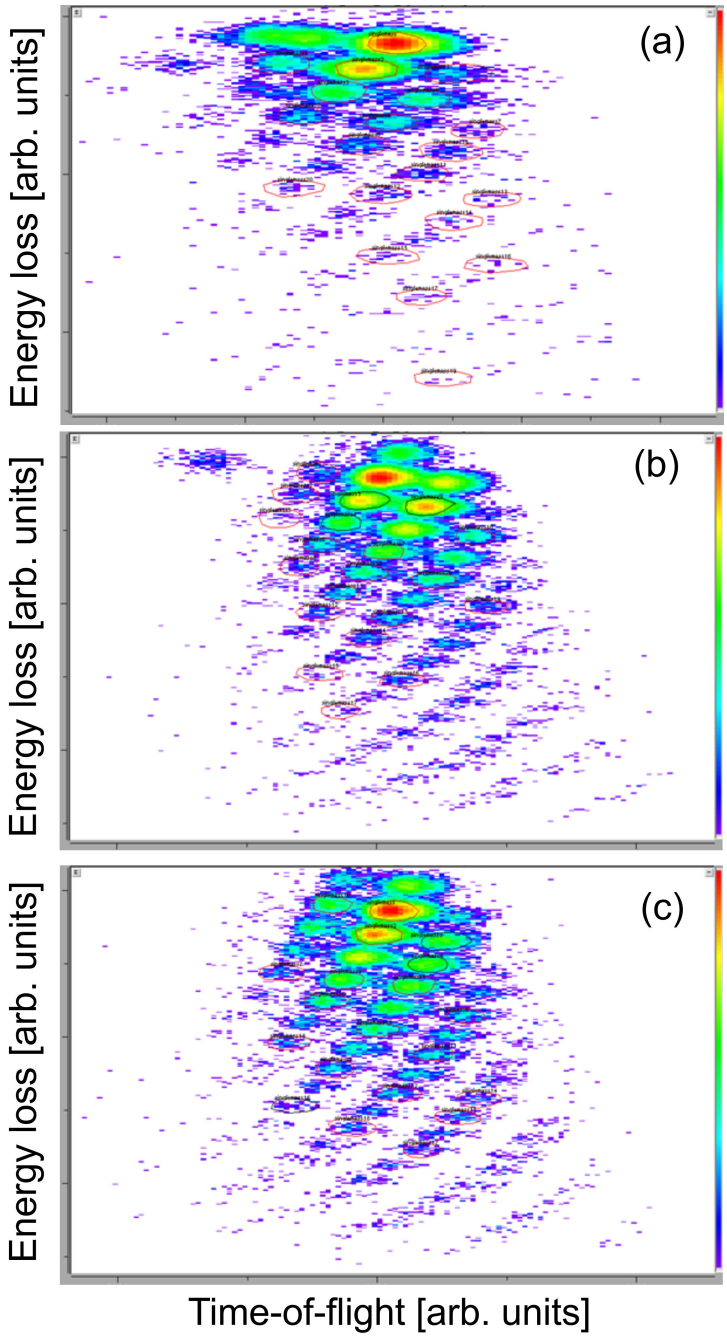

Figure 3.9: Three (a,b,c) PID spectra used to select fragment species for use in analysis of crystal response to charged particles in crystal number 10.

Table 3.2: Data set of fragment species used to determine response function of crystal ten.

PID a			PID b			PID c		
Fragment	Energy [MeV]	Light [ch]	Fragment	Energy [MeV]	Light [ch]	Fragment	Energy [MeV]	Light [ch]
^{75}Ge	7587.8	1727.6	^{75}Ge	7133.6	1692.9	^{73}Ge	6927.0	1667.6
^{74}Ga	7220.2	1714.5	^{73}Ga	6906.4	1682.2	^{72}Ge	7051.9	1678.9
^{73}Ga	7343.8	1723.0	^{72}Ga	7028.5	1693.6	^{70}Ga	6836.9	1673.7
^{72}Ga	7469.3	1730.4	^{71}Ga	7153.1	1703.2	^{69}Ga	6962.4	1683.5
^{71}Zn	7098.4	1715.5	^{71}Zn	6677.5	1669.4	^{67}Zn	6744.8	1679.0
^{70}Zn	7222.9	1724.4	^{70}Zn	6798.8	1685.2	^{67}Cu	6282.0	1646.2
^{69}Cu	6851.6	1707.5	^{68}Zn	7047.0	1708.5	^{66}Cu	6402.4	1659.6
^{68}Cu	6974.3	1717.8	^{68}Cu	6566.6	1676.3	^{65}Cu	6525.5	1673.0
^{67}Cu	7099.5	1730.8	^{67}Cu	6688.4	1689.2	^{64}Ni	6182.7	1652.2
^{66}Ni	6724.7	1709.8	^{66}Ni	6333.4	1667.7	^{62}Ni	6428.2	1679.1
^{65}Ni	6848.0	1719.7	^{65}Ni	6453.4	1680.5	^{61}Co	6080.7	1659.0
^{63}Co	6594.8	1712.7	^{64}Ni	6576.2	1684.7	^{60}Fe	5737.1	1634.4
^{62}Fe	6219.7	1685.7	^{63}Co	6216.6	1674.2	^{58}Fe	5977.2	1663.6
^{61}Fe	6340.2	1700.8	^{61}Co	6461.4	1698.2	^{57}Mn	5628.7	1640.4
^{60}Fe	6463.6	1716.6	^{61}Fe	5978.3	1661.3	^{54}Cr	5518.6	1645.2
^{58}Mn	6205.4	1705.1	^{60}Fe	6098.2	1675.7	^{53}Cr	5639.6	1660.2
^{54}V	5685.0	1680.6	^{58}Mn	5856.2	1666.2	^{51}V	5406.0	1652.4
^{53}V	5806.3	1695.2	^{54}V	5368.0	1644.1	^{53}V	5169.7	1615.7
^{49}Sc	5276.5	1674.4	^{53}V	5485.8	1659.1	^{50}Ti	5052.6	1624.8
^{37}S	4151.2	1635.9	^{49}Sc	5276.5	1636.4	^{47}Sc	4933.0	1633.0

The process of isolating a particular fragment species deposited in a crystal and the subequent determination of the implanted energy was repeated for fifteen other crystals in the hodoscope array. The fragment and energy ranges used in the corresponding response analysis are given in Table 3.3. The remaining sixteen crystals were not analyzed for response functions due to the insufficient number of fragments deposited in the crystals.

After identification of the fragments deposited in the hodoscope crystals and calculation

Table 3.3: Ranges of fragment species and energies used to calculate the charged particle response for sixteen hodosocpe crystals.

Crystals	Fragment range	Energy range [MeV]
2,3	^{75}Ge - ^{43}K	6956.7 - 4286.2
6,7	^{76}Ge - ^{43}K	7309.2 - 4369.3
10,11	^{75}Ge - ^{37}S	7587.8 - 4151.2
14,15	^{75}Ge - ^{37}S	7743.5 - 4225.9
18,19	^{75}Ge - ^{37}Cl	7899.7 - 4350.1
22,23	^{74}Ge - ^{37}Cl	8187.0 - 4427.2
26,27	^{74}Ge - ^{38}Cl	8345.6 - 4381.6
30,31	^{73}Ge - ^{40}Ar	8639.4 - 4995.9

of the deposited energy, the next step of the analysis procedure was to determine the appropriate description of the crystal response. The response of organic scintillators to charged particles was first described by Birks [59] and subsequently extended to inorganic scintillators by Birks [60]. The relationship between the fluorescence energy emitted per unit length, $^{dL}/_{dx}$, and the specific energy loss per unit length,$^{dE}/_{dx}$, is given by

$$\frac{dL}{dx} = \frac{S(^{dE}/_{dx})}{1 + kB(^{dE}/_{dx})}, \tag{3.2}$$

where S is a scintillation efficiency and kB is the quenching factor, commonly referred to as 'Birks' constant' and usually evaluated through a fit to experimental data. The specific

energy loss, $^{dE}/_{dx}$, was defined by the first term in Equation 2.3. The application of equation 3.2 to the response of CsI(Tl) scintillators to charged particles up to ^{12}C at 437 MeV was performed by Horn *et al* [51]. Integration of Equation 3.2 results in the light output over the range of a particle to be:

$$L = a_0 + a_1 \left\{ E - a_2 A Z^2 ln \left| \frac{E + a_2 A Z^2}{a_2 A Z^2} \right| \right\} \tag{3.3}$$

where E is the energy of the particle, m is the mass of the particle, Z is the nuclear charge of the particle, a_0 is a zero-offset term in units of channels, $a_1 = gS$ in units of channels/MeV with g the electronic gain factor for the scintillation efficiency, and $a_2 = ckB$ in units of MeV. Equation 3.3 was applied to the hodoscope crystals using the light output determined for the unique fragments implanted into the sixteen hodoscope elements. A single global fit of the Horn function (equation 3.3) was performed for each crystal to obtain values for the coefficients a_0, a_1, and a_2. The results of this global fit procedure will be presented in Chapter 4 and discussed in Chapter 5.

3.3.3 Charge-State Analysis

As part of the effort to evaluate the adequateness of the hodoscope detectors to independently identify the charge-state of incoming particles, the production rates of various atomic charge-states were calculated using LISE++ [58]. For example, the fragments $^{72}_{31}$Ga^{31+} and $^{70}_{31}$Ga^{30+} have similar mass-to-charge ratios, 2.32 and 2.33 respectively, and would overlap in time-of-flight to the S800 focal plane and would therefore be indistinguishable in $^{m}/_{q}$. The estimated production rates of the fully stripped and hydrogen-like ion were 7.6 and 0.054 pps, respectively for a ^{76}Ge primary beam rate of 1.5x10^{-4} pnA impinging the Au target.

3.4 Momentum Distributions

The final section of the this chapter is devoted to a description of the analysis steps performed to deduce the momenta of fragmentation products produced during NSCL experiment 10501. The analysis of the momenta of the fragments included the reconstruction of the total linear momentum, the parallel and perpendicular momentum components of each fragment, as well as determination of the parallel momentum transfer associated with each fragment.

3.4.1 Total and Parallel Momentum Distribution Reconstruction

The process of calculating total and parallel momentum distributions of fragmentation products from the experimentally measured parameters first required the conversion of parameters calculated for the ions at the target position of the S800 into physically meaningful values for each identified fragment. The kinematic parameters at the target position are shown schematically in Figure 3.10. The dispersive (ata) and non-dispersive (bta) angles (defined in section 2.3.1) were used to deduce the scattering angle (θ) of an event at the target position using the following relation:

$$\theta = \arcsin\left[\sqrt{(\sin(ata))^2 + (\sin(bta))^2}\right], \tag{3.4}$$

and p, the total linear momentum, is deduced using the following equation:

$$p = E\sqrt{1 + \frac{2\,(mass)\,(amu)}{E}}, \tag{3.5}$$

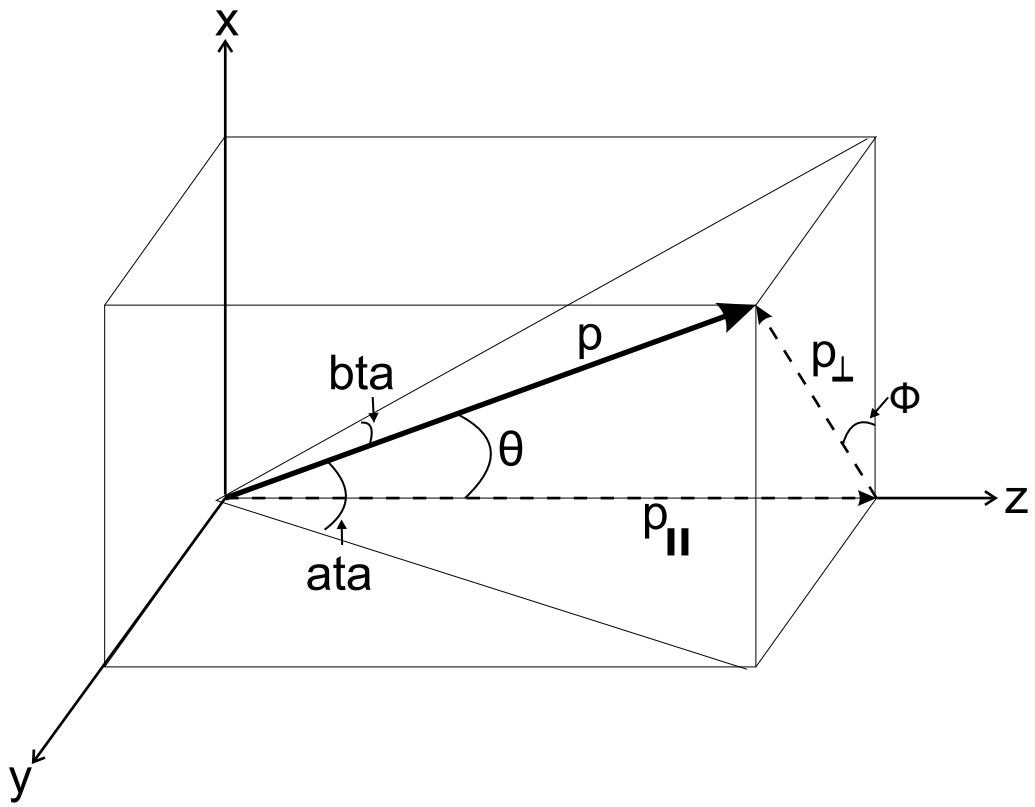

Figure 3.10: Schematic of the physical parameters associated with the target position of the S800.

where $E = mass * amu(\gamma - 1)$ is the energy of the particle, *mass* is the mass (A) of the particle (set during off-line analysis), *amu* is the atomic mass unit in MeV. The parallel and perpendicular components of the total linear momentum were deduced from θ and p using the trigonometric relationships:

$$\begin{aligned} p_{||} &= p\cos(\theta) \\ p_{\perp} &= p\sin(\theta) \end{aligned} \tag{3.6}$$

After determining $p_{||}$ and $p_{\perp}$, the three momentum values, p, $p_{||}$, and $p_{\perp}$ were transformed from the laboratory frame into the reference frame of the fragment.

The process of identifying fragment species that might be suitable for full momentum reconstruction, the PID spectra shown in Figure 3.6 and the corresponding five Bρ settings

for each target species were analyzed further. To be suitable for momentum reconstruction, essentially all portions of the total and parallel distributions must have been measured during data collection. The majority of the momentum distributions were contained in three Bρ settings of the spectrometer, but some extended to a fourth and occasionally a fifth Bρ setting particularly for low mass fragments. After identification of the Bρ settings necessary for a full reconstruction, separate Bρ data sets were normalized using the following equation:

$$NormalizedCounts = \frac{counts_{scint}}{livetime} \tag{3.7}$$

where $counts_{scint}$ was the number of events collected by the thin scintillator at the object position of the S800 analysis line during the run and *livetime* was defined as:

$$livetime = \frac{liveclock}{rawclock} < 1, \tag{3.8}$$

where *liveclock* was the gated clock and *rawclock* was the free clock, both recorded by scalers during each run. The appropriate bin size for proper histogramming of the momentum distribution of each data set was chosen such that counts in adjacent bins agree to within statistical error. The final bin size chosen for all momentum data sets was 35 bins over a range of 1500 MeV/c.

The final step in the momentum reconstruction was the combining of the data sets to build the full momentum distributions. As an example, in Figure 3.11 the data sets used to assemble the full parallel momentum distribution for ^{53}Cr fragments produced from the interaction of the ^{76}Ge beam in the Au target are shown. The three symbols in Figure 3.11 attribute the data to one of the three different Bρ settings of the spectrometer. Finally, the total and parallel momentum distributions were evaluated using a Gaussian fit to the distribution, where the peak position and the width, σ, were unconstrained parameters of

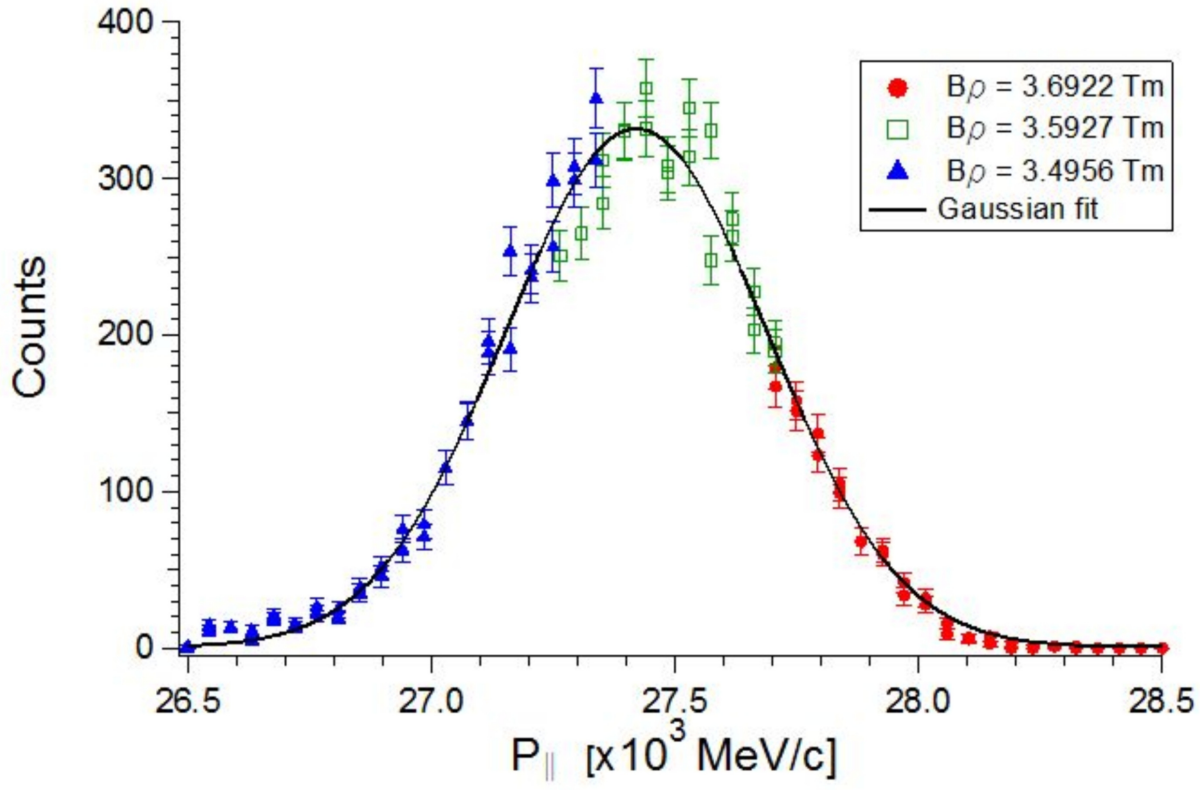

Figure 3.11: Parallel momentum distribution of ^{63}Cu fragments reconstructed from the data sets collected with four Bρ spectrometer settings.

the fit routine. The contribution to the momentum width from the target thickness was calculated by considering the two extreme cases of fragment production; at the upstream and downstream faces of the target. For example, the difference in outgoing momenta of a ^{69}Zn fragment produced at the upstream and downstream edges of the gold target is only 10 MeV/c. The momentum difference at the opposite faces of the beryllium target is 30 MeV/c. The differential momentum losses increase with increasing mass and charge loss of the projectile fragments.

3.4.2 Perpendicular Momentum Distribution Reconstruction

The reconstruction of the perpendicular momentum distributions for the identified fragments was accomplished by first identifying the Bρ setting that contained the peak of the parallel momentum distribution for that fragment. In Figure 3.12 is shown an example of the correlation of the parallel and perpendicular momenta. The width of the perpendicular momentum distribution varied by approximately 70 MeV/c when deduced from the three data sets (corresponding to three different average Bρ settings) that were combined to form the full parallel momentum distribution. The Bρ data set that contained the peak in parallel momentum was also used to calculated the differential cross section in counts per steradians as a function of perpendicular momentum using Equation 3.9 and Equation 3.6. Note that the differential cross section in the proper units of barns per steradians was not calculated because the beam current was not measured during the experiment.

$$\frac{d\sigma}{d\Omega} = \frac{d\sigma}{d\theta \sin\theta} \tag{3.9}$$

The final step of the perpendicular momentum distribution analysis was to fit the distribution with a Gaussian function to obtain the peak centroid and width, σ.

3.4.3 Parallel Momentum Transfer Measurement

After reconstruction of the parallel momentum distributions for the fragmentation products, the centroid of the Gaussian distribution was obtained and the momentum transfer of each fragment was then deduced using the following equation:

$$-\langle p_{\parallel transfer} \rangle = p_{\parallel beam} - p_{\parallel fragment} \tag{3.10}$$

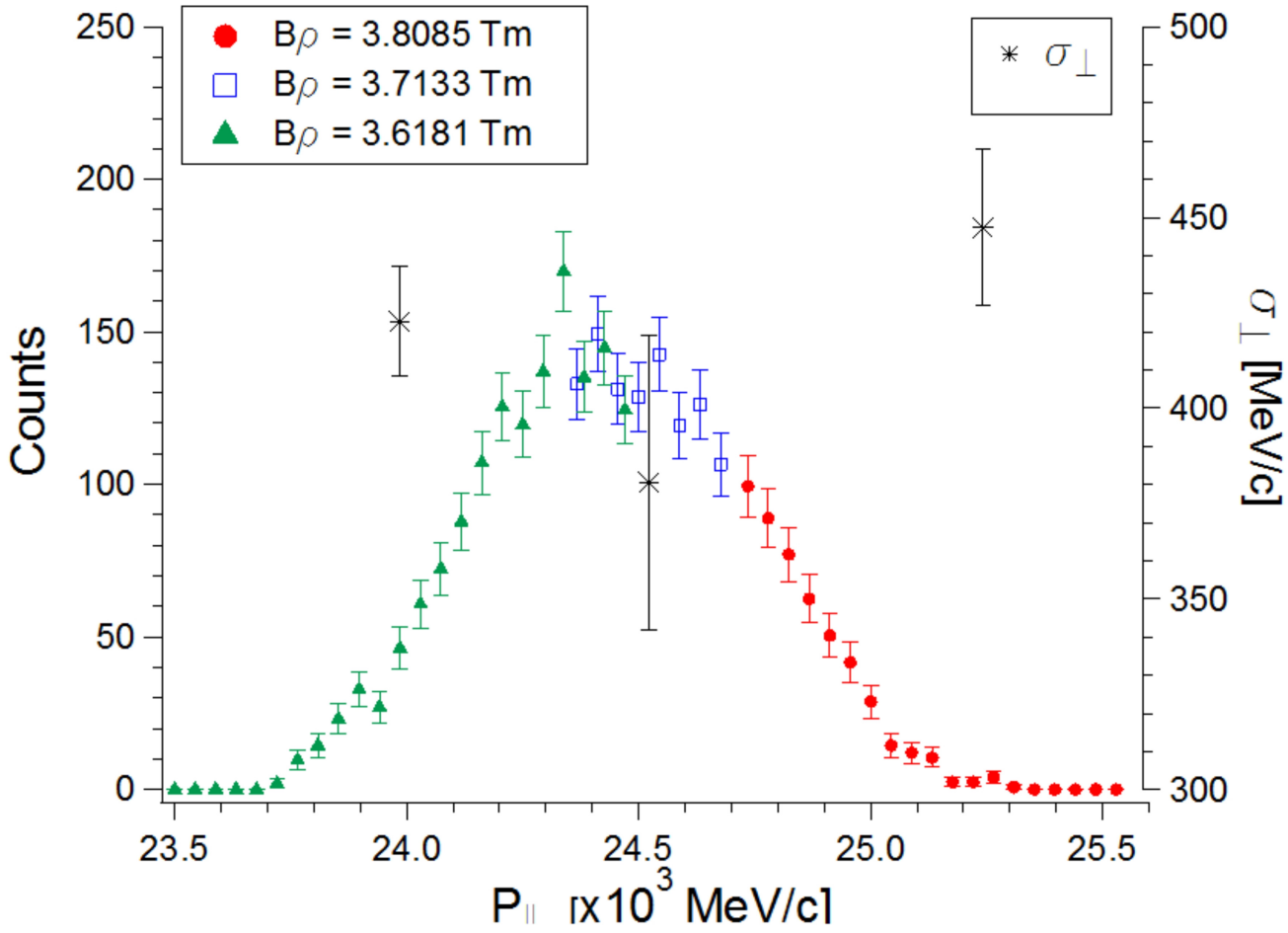

Figure 3.12: Parallel momentum distribution of ^{57}Mn fragments reconstructed from the data sets collected with four Bρ spectrometer settings and the corresponding widths for the perpendicular momentum distribution calculated from each data set.

The results of the calculation of the momentum transfer associated with all analyzed fragments will be presented in Chapter 4.

Chapter 4

Results

This chapter presents the results of NSCL experiment 10501, details of the new hodoscope array's capabilities with regard to energy measurement, and atomic charge state identification. The results of the analysis of experimental linear momentum distribution measurements will also be presented. In particular the two components of the linear momentum,the parallel and perpendicular distribution data, will be presented in full.

4.1 Hodoscope Characteristics

The goal of installing the new hodoscope array in the S800 focal plane was to improve the measurement of the residual total kinetic energy of impinging particles so that the atomic charge-state of each particle could be readily deduced. The resolving power was used to evaluate the performance of each of the hodoscope crystals in this regard. A response function was developed to accurately describe the light output from each crystal to incoming particle energy, mass, and nuclear charge.

4.1.1 Light Resolution

The resolution of the light output from each crystal was analyzed using data from the implantation of monoenergetic ^{76}Ge beam particles implanted into each crystal. In Figure 3.8 is shown the spectra of the raw light output from crystals #10 and #11. Similar spectra were collected for the other 30 crystals. A Gaussian function was used to fit each raw light peak. The resolution (defined in equation 2.4) of each peak was calculated from the results of the Gaussian fit and the raw light resolution values are summarized in Figure 4.1 for all 32 crystals. The average resolution for the light output from the ^{76}Ge beam particles

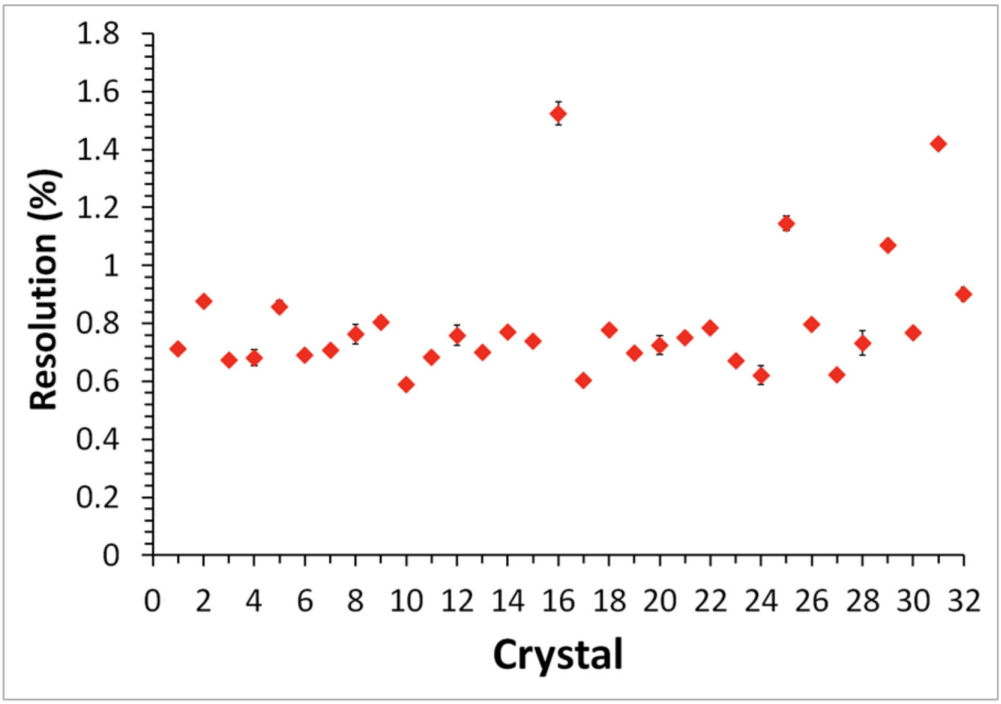

Figure 4.1: Resolution of raw light signals from ^{76}Ge beam particles in the 32 crystals of the hodoscope array.

was 0.80±0.21%. These measured light resolution values presented in Figure 4.1 represent a folding of the beam resolution and the intrinsic resolution of the crystals. The measured momentum spread of the beam of 0.076% was transformed into a range value of 3.124±0.0231

mm into the CsI(Na) material. The light output from scintillators is generally proportional to the range for highly ionizing particles, so this resolution of the range, 0.74%, was equated to the resolution of the light output of the crystals. Unfolding the light resolution associated with the beam from the measured resolution results in an average intrinsic resolution of 0.30%. The energy straggling associated with the focal plane detectors upstream of the hodoscope is negligible.

The light resolution of sixteen crystals (2, 3, 6, 7, 10, 11, 14, 15, 18, 19, 22, 23, 26, 27, 30, 31) was also analyzed for ^{55}Cr fragments produced from the interaction of the ^{76}Ge beam in a Be target. The fragment species ^{55}Cr was chosen because it was implanted into the largest number of crystals (distributed most broadly in the S800 focal plane). The resulting light output spectra were also fitted with a Gaussian function. The resolution of each peak was deduced using equation 2.4 and the resolution values are summarized in Figure 4.2. The average resolution for the light output from the ^{55}Cr particles was 1.35±0.82%. The decrease in resolution compared to the ^{76}Ge particle signals can be attributed to the increase in energy spread of the ^{55}Cr fragment compared to the ^{76}Ge energy spread. The removal of the deduced intrinsic energy resolution of the crystals from the measured resolution of the ^{55}Cr fragments results in an average resolution of 1.32%. This resolution is comparable to the 1.68% energy width of the crystal. An improved energy resolution could be achieved by combining the crystal signal with sub-crystal position information using the CRDCs.

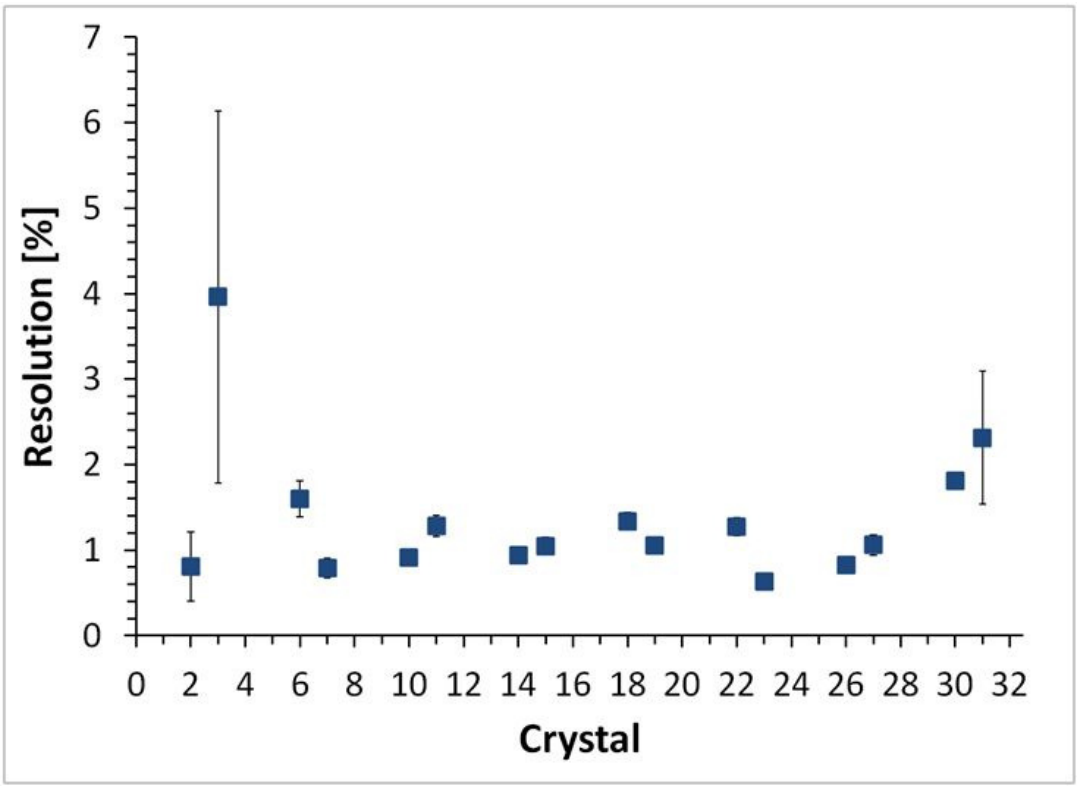

Figure 4.2: Resolution of raw light signals from ^{55}Cr particles in sixteen crystals of the hodoscope array. Large error bars for crystals 2,3, and 31 are due to very low statistics.

4.1.2 Crystal Response Function

To assess the improvement to energy measurements over the thick plastic scintillators the new hodoscope replaced, the light output of the crystals was characterized on an event-by-event basis as a function of incoming particle energy, mass, and nuclear charge (E, A, and Z). The development of the response function to the sixteen crystals in the hodoscope, which were impinged with fragment particles with sufficient statistics, was detailed in Chapter 3. The response function represents a unique global expression for the light output for each crystal. The energy, mass, and charge regions available to the application of the response function was 3.60 - 7.60 GeV in the fragment reference frame, 37 - 75 amu, and 17 - 33, respectively. The light response as a function of energy is presented in the upper panels of

Figures 4.3 and 4.4 for crystals 2, 3, 6, 7, 10, 11, 14, and 15 and 18, 19, 22, 23, 26, 27, 30, and 31, respectively. The residual values for the difference between the experimental light output and the value generated by the response function are shown in the lower panels in Figures 4.3 and 4.4.

The values of the three coefficients (a_0, a_1, a_2) in the response function deduced for each crystal are listed in Table 4.1 for crystals 2 ,3, 6, 7, 10, 11, 14, 15, 18, 19, 22, 23, 26, 27, 30, and 31. The values of each coefficient are in general agreement for the different crystals, indicating similar response of the crystals to the impinging particles. The low values of the residuals also support the choice of response function. The residuals for each crystal center at or near 0% with no residual value exceeding ±3%. Nonetheless, a range of response values are seen for the crystals. A few crystals are relatively insensitive to the mass and charge, i.e. #2, whereas others are very sensitive to the particle type, e.g. #31.

Future experiments measuring particles with energy, mass, or charge values outside the ranges probed by the current experiment are required to validate the derived response function outside the range of the present energy, mass, and nuclear charge parameters. The sixteen crystals for which a response function could not be generated due to insufficient fragmentation data did respond similarly to gamma-rays. It may be expected that the response functions for these crystals will be similar to the sixteen crystals that were characterized with the response function.

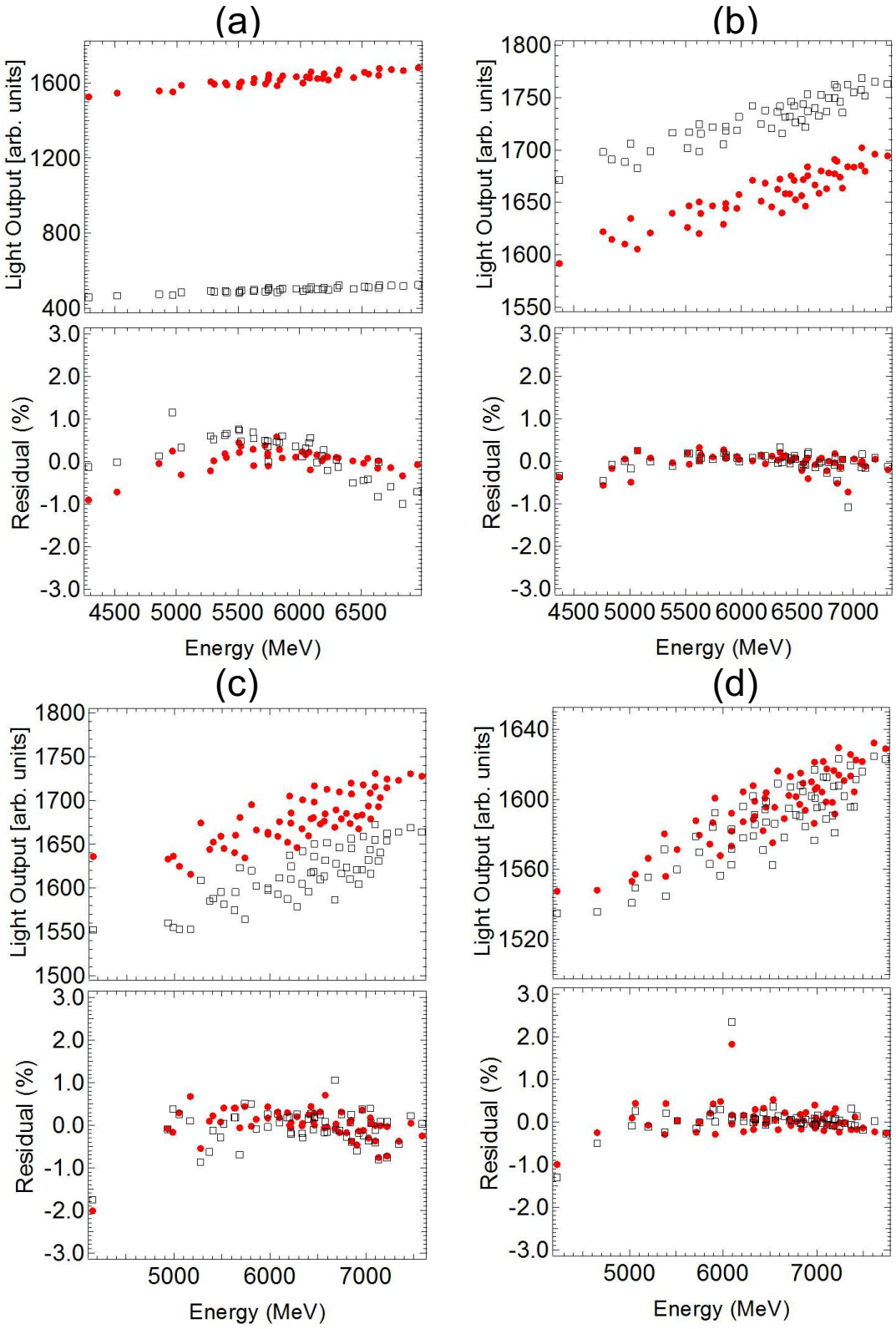

Figure 4.3: Light response as a function of particle energy (upper plot) and corresponding residual values (lower plot). (a)crystals 2 and 3 (b)crystals 6 and 7 (c)crystals 10 and 11 (d)crystals 14 and 15. Even numbered crystals are represented by solid circles and odd numbered crystals by open squares. Error bars are smaller than symbols.

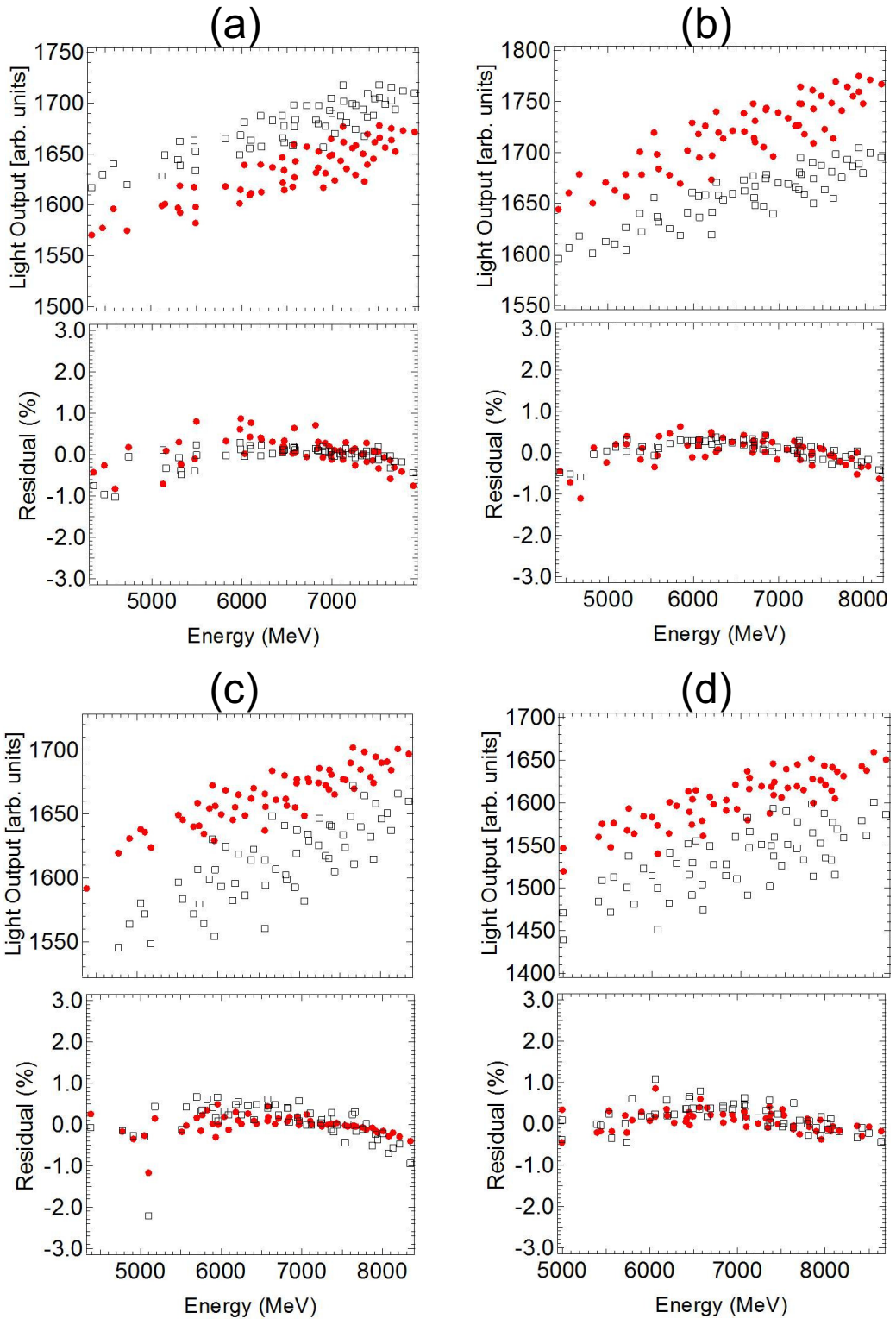

Figure 4.4: Light response as a function of particle energy (upper plot) and corresponding residual values (lower plot). (a)crystals 18 and 19 (b)crystals 22 and 23 (c)crystals 26 and 27 (d)crystals 30 and 31. Even numbered crystals are represented by solid circles and odd numbered crystals by open squares. Error bars are smaller than symbols.

Table 4.1: Coefficient values from global fits to the light response expression in equation 3.3 for sixteen hodoscope crystals. Values are in units of channels, channels/MeV, and MeV, respectively.

Crystal	a_0 [channels]	a_1 [channels/MeV]	a_2 [MeV]
2	920.64 ± 0.54	0.16816 ± 0.00096	0.01765 ± 0.00287
3	206.01 ± 0.10	0.73386 ± 0.00025	0.02061 ± 0.00003
6	1217.6 ± 1.0	0.10583 ± 0.00031	0.02186 ± 0.00006
7	1326.4 ± 1.2	0.09789 ± 0.00042	0.02238 ± 0.00011
10	1185.9 ± 1.1	0.12158 ± 0.00031	0.02661 ± 0.00006
11	1074.9 ± 2.1	0.12980 ± 0.00061	0.02458 ± 0.00012
14	1271.3 ± 0.7	0.07241 ± 0.00020	0.02140 ± 0.00006
15	1167.2 ± 1.4	0.09919 ± 0.00040	0.02649 ± 0.00009
18	1216.6 ± 1.0	0.09980 ± 0.00031	0.03070 ± 0.00008
19	1269.5 ± 1.0	0.09567 ± 0.00030	0.02904 ± 0.00008
22	1214.7 ± 1.1	0.12161 ± 0.00035	0.03511 ± 0.00009
23	1215.2 ± 0.6	0.10816 ± 0.00017	0.03676 ± 0.00003
26	1330.6 ± 0.4	0.07681 ± 0.00052	0.03289 ± 0.00013
27	992.56 ± 1.09	0.15658 ± 0.00049	0.04411 ± 0.00032
30	1058.2 ± 1.9	0.12681 ± 0.00057	0.03855 ± 0.00015
31	790.92 ± 3.43	0.18580 ± 0.00100	0.04797 ± 0.00024

4.1.3 Energy Resolution

The response functions for the hodoscope crystals provided the necessary analysis tool to determine the energy resolution of the hodoscope as a total energy detector. The same data sets used in the light resolution determination were also used to deduce the energy resolution. The individual response function coefficients were applied to the data from each crystal to transform the light output spectrum into an energy spectrum. The energy resolution found following the transformation of ^{76}Ge monoenergetic beam data into energy are presented in Figure 4.5. The same energy transformation procedure was applied to the ^{55}Cr fragment data and the resulting energy resolutions are presented in Figure 4.6. The average energy

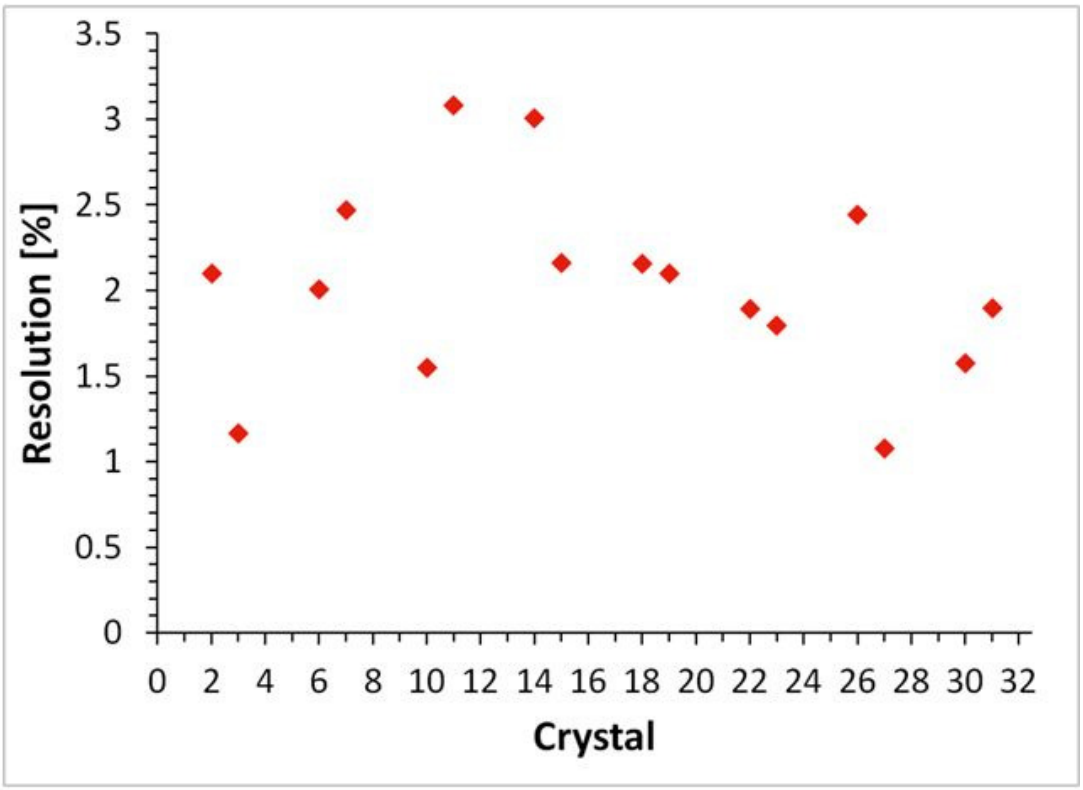

Figure 4.5: Resolution of calculated energy signals from ^{76}Ge particles in sixteen crystals of the hodoscope array. Error bars are smaller than data symbols.

resolution of the ^{76}Ge beam particles is 2.03 $\pm$ 0.56% and the average energy resolution of

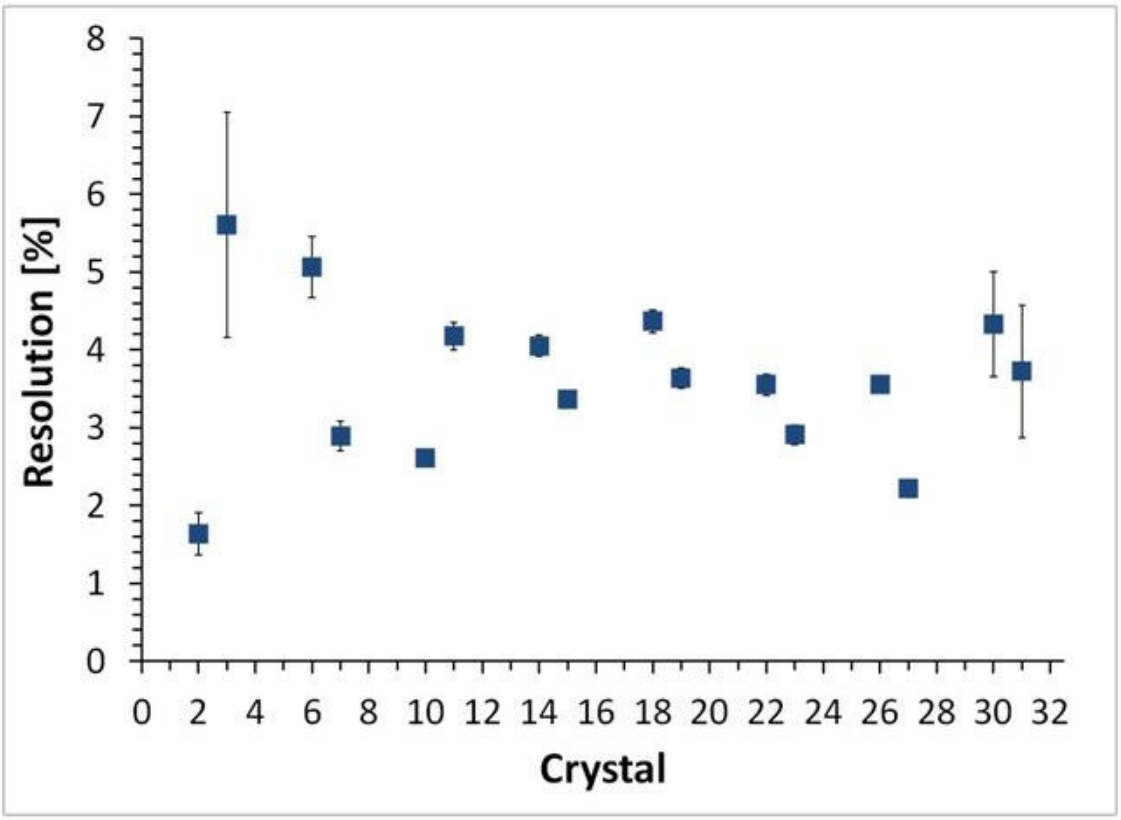

Figure 4.6: Resolution of calculated energy signals from ^{55}Cr particles in sixteen crystals of the hodoscope array. Large error bars for crystals 2,3, and 31 are due to very low statistics.

the ^{55}Cr particles is 3.61 $\pm$ 1.02%. Note that a decrease in resolution between the light output data and the calculated energy spectra by a factor of approximately 2.5.

The energy resolution of 3.61% for the ^{55}Cr fragments represents a significant improvement over previous total kinetic energy resolution values on the order of 20% [61] achieved with the thick plastic scintillators that previously existed as the most downstream detectors in the S800 focal plane. Future experimenters will have the opportunity to measure the residual energy of particles of interest to much higher precision than was previously achievable.

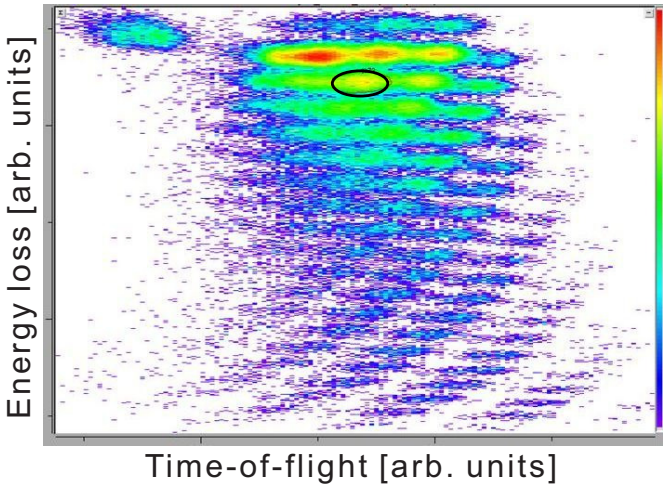

Figure 4.7: Particle identification spectrum used to isolate fragments $^{72}_{30}\mathrm{Ga}^{31+}$ and $^{70}_{30}\mathrm{Ga}^{30+}$ in the location indicated by black oval.

4.1.4 Charge-State Separation

The goal of uniquely identifying the atomic charge-states of incoming particles by measuring the residual kinetic energy signal with the hodoscope was demonstrated using two fragments with different atomic charge-states but overlapping mass-to-charge ratios. The fragment pair selected for charge-state separation analysis was $^{72}_{30}\mathrm{Ga}^{31+}$ and $^{70}_{30}\mathrm{Ga}^{30+}$, which were produced with sufficient rate to permit a meaningful demonstration of separation success. The region of the PID spectrum that contained these fragments was gated to generate a 2-D spectrum of dispersive position (directly related to momentum) vs light output from hodoscope crystal 14. In Figures 4.7 and 4.8 are shown the PID used to gate the fragments of interest and the resulting 2-D spectrum, respectively.

The energy separation between $^{72}_{31}\mathrm{Ga}^{31+}$ and $^{70}_{31}\mathrm{Ga}^{30+}$ calculated with LISE++ code [58] was 3.72%. This separation corresponds to a predicted separation of the light output of 0.96% using the coefficient results from the global response function for crystal 13. The measured separation in light output between the two set of events, shown in Figure 4.8

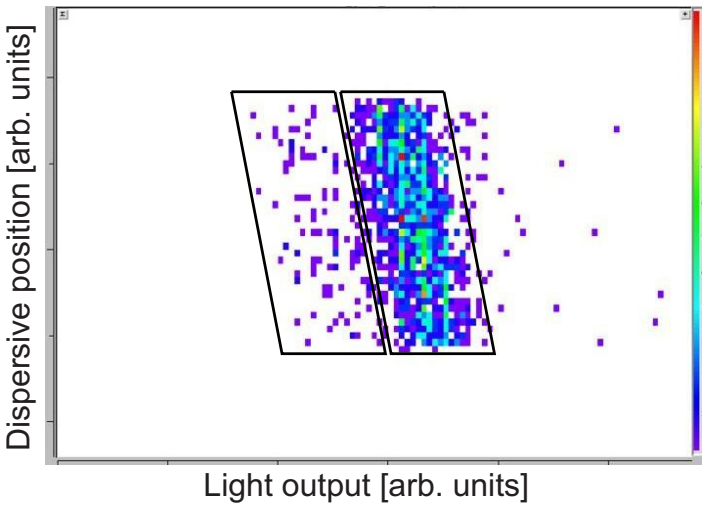

Figure 4.8: Dispersive position vs hodoscope crystal 14 light output for fragments $^{72}_{30}\mathrm{Ga}^{31+}$ (right tilted box) and $^{70}_{30}\mathrm{Ga}^{30+}$ (left tilted box).

by the two boxes, is 1.13%, which indicates that the hodoscope data can be used to readily identify these fragments.

4.2 Linear Momentum Distributions

Parallel and perpendicular momentum distributions have been determined for a wide range of fragments produced by the interaction of ^{76}Ge in either a ^{9}Be or a ^{197}Au target. The complete distributions of 83 unique fragments ranging between ^{75}As and ^{37}Cl and 71 unique fragments ranging between ^{74}As and ^{37}Cl, produced in the Be and Au targets, respectively, were analyzed and the results of the measurements are presented in the following sections. Full distributions and calculated width, σ, values are presented as well as the measured parallel momentum transfer, $-\langle p_{\parallel_{transfer}} \rangle$, for all 154 fragments.

4.2.1 Parallel Momentum Distributions

The parallel momentum distributions of 154 fragments were reconstructed from the momenta measured during NSCL experiment 10501 and the parameters of the distribution were summarized in terms of the width of the distribution and the centroid. As examples, six parallel momentum distributions for ^{71}Ga, ^{65}Zn, ^{60}Co, ^{54}Cr, ^{47}Sc, and ^{39}Cl are presented in Figures 4.9 and 4.10, where the target was Be or Au, respectively.

The parallel momentum distributions of the additional 148 fragments are given in Appendix A, which includes the extent to which the full distributions were constructed for the vast majority of the fragment species analyzed. The extracted longitudinal width,

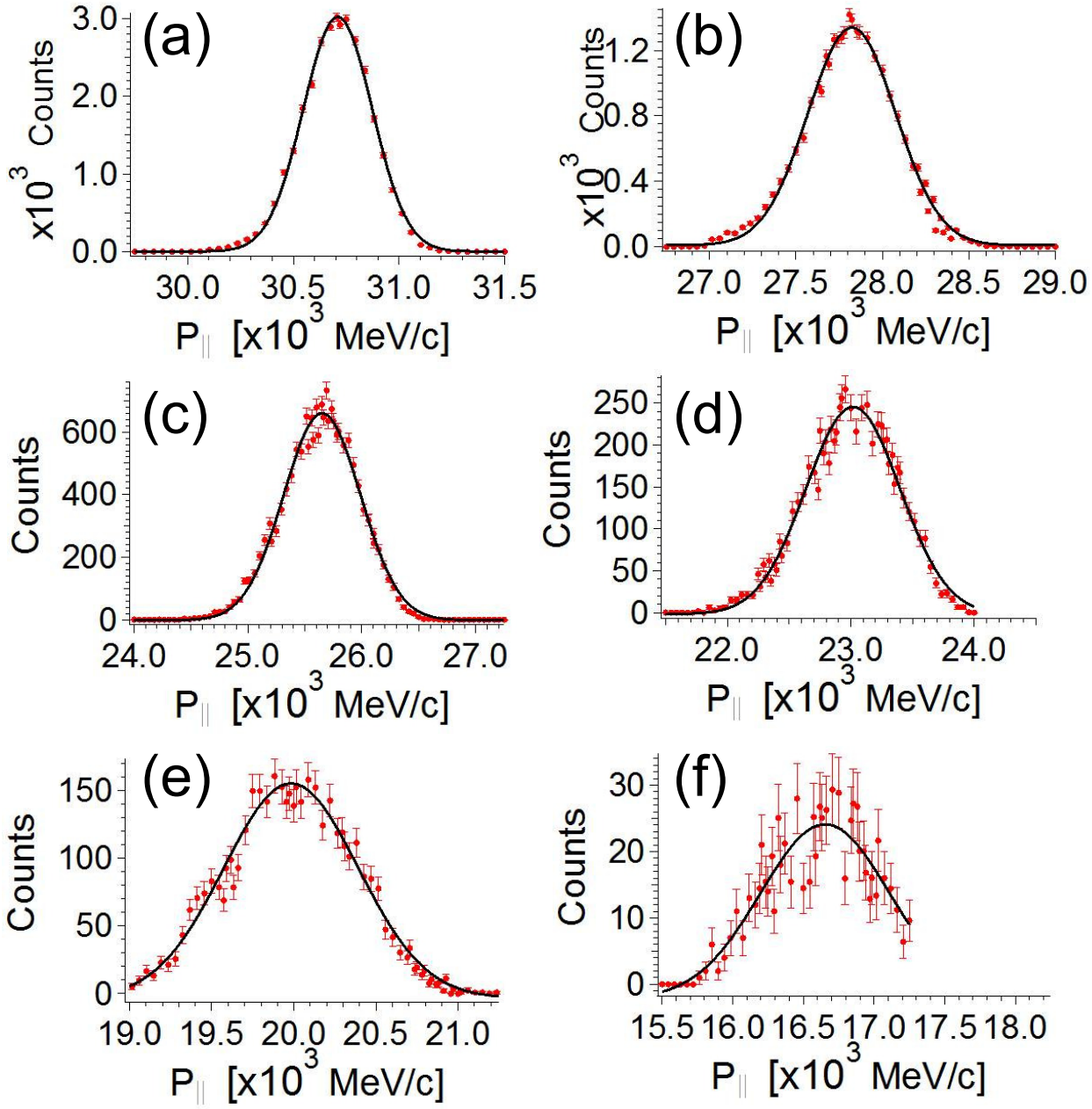

Figure 4.9: Parallel momentum distributions for fragments produced from ^{76}Ge on a Be target. (a) ^{71}Ga (b) ^{65}Zn (c) ^{60}Co (d) ^{54}Cr (e) ^{47}Sc (f) ^{39}Cl.

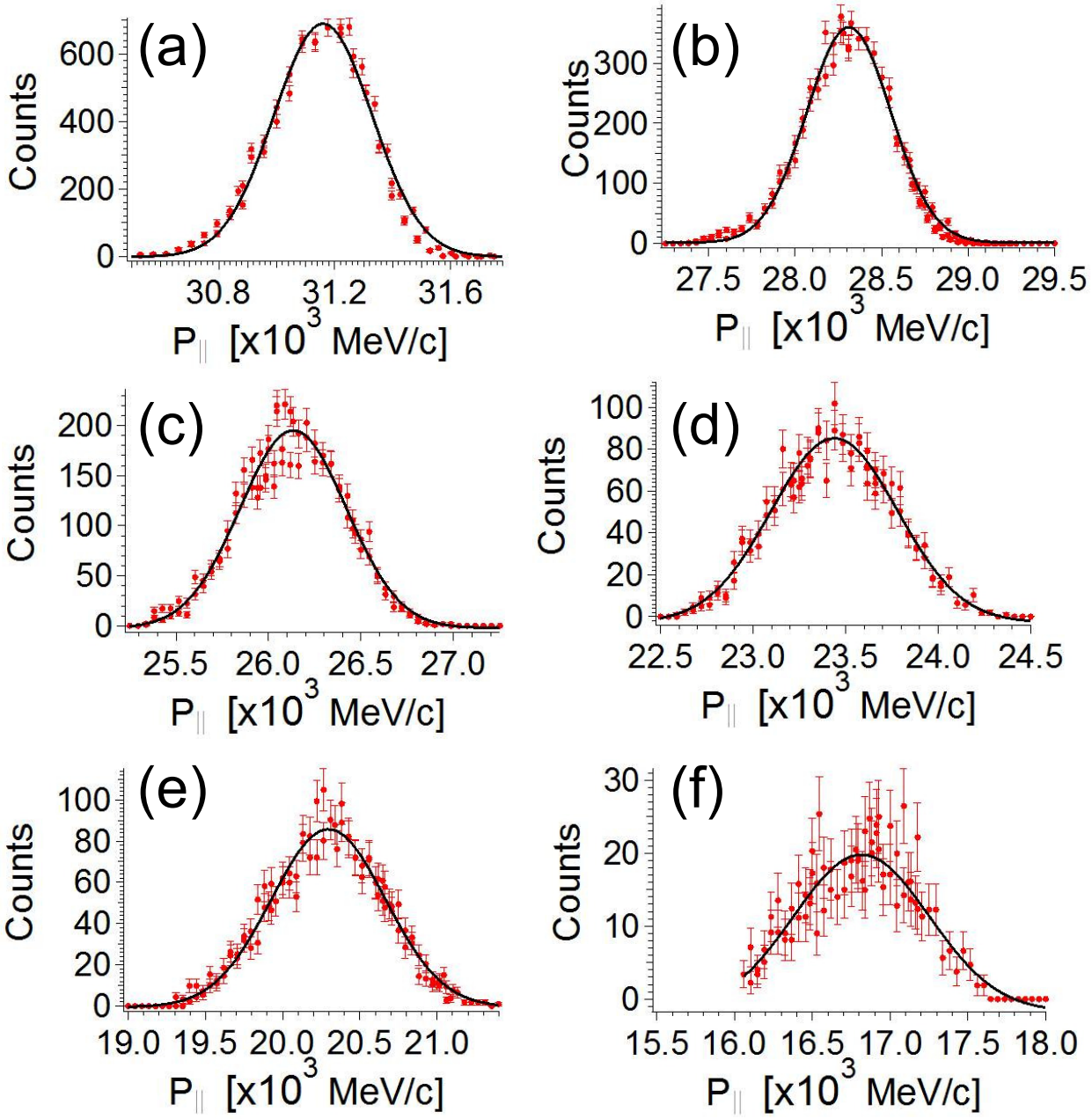

Figure 4.10: Parallel momentum distributions for fragments produced from ^{76}Ge on a Au target. (a) ^{71}Ga (b) ^{65}Zn (c) ^{60}Co (d) ^{54}Cr (e) ^{47}Sc (f) ^{39}Cl.

$\sigma p_{||}$, of each distribution is shown in Figure 4.11 as a function mass loss, ΔA, where $\Delta A = A_{projectile} - A_{fragment}$. Also shown in Figure 4.11 are two best fits to the

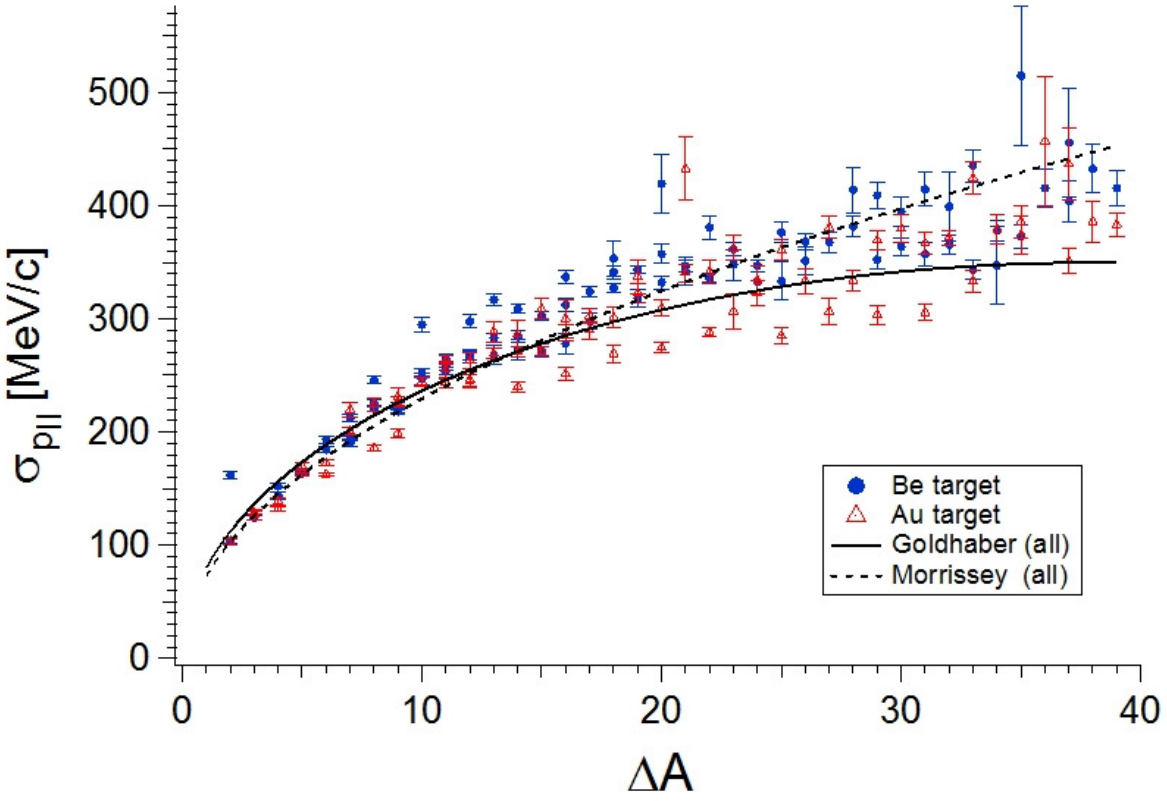

Figure 4.11: Width of the parallel momentum distribution, $\sigma p_{||}$, as a function of the fragment mass loss, ΔA, for two target species, beryllium (circles) and gold (triangles). Solid and dashed lines represent the best fits to the data for Goldhaber and Morrissey models, respectively.

fitted values using the two models by Goldhaber [24] and Morrissey [36], that were described in detail in Chapter 1. The values for the coefficients resulting from each best fit were $\sigma_0 = 80 \pm 1$ MeV/c for the Goldhaber model and $\sigma_0 = 73 \pm 1$ MeV/c for the Morrissey model.

The centroid of each parallel momentum distribution was used to obtain the average parallel momentum transfer associated with each fragment. The momentum loss, or down-shift in parallel momentum, between the fragment and the original projectile parallel momentum is presented in Figure 4.12 for both target data sets as a function of mass loss (ΔA) of the

fragment.

The deduced parallel momentum transfer for the two target data sets were compared to

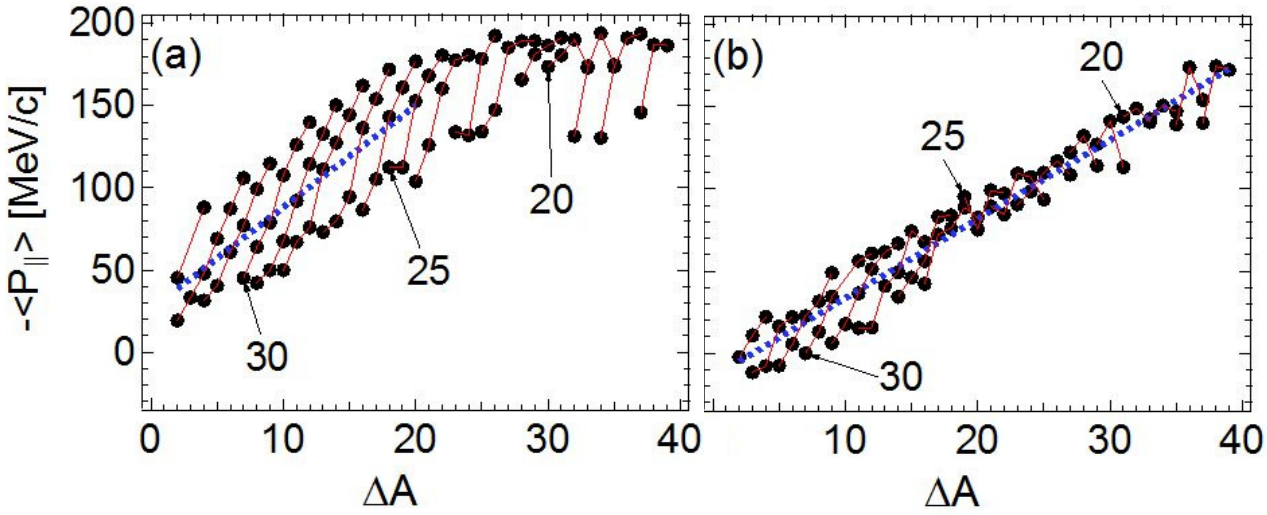

Figure 4.12: Parallel momentum transfer as a function of mass loss (ΔA) for fragments produced using beryllium and gold targets. Dashed lines represent the best linear fits to the data. Solid lines connect isotope chains with the numbers indicating isotope chains Z=30, Z=25, and Z=20. Uncertainties in the data are smaller than the symbols.

a linear best fit described by Morrissey [36]. The slopes of each best fit to the linear model are 6.2 and 4.8 MeV/c for the beryllium and gold targets, respectively. The general trends in parallel momentum transfer for a particular isotope chain are also indicated in Figure 4.12 by a solid line connecting fragments with identical Z in the range Z=17 to Z=33. Isotope chains Z=33 through Z=27 from both target species were found to have similar slopes, and these slope values were larger than the average slope over the entire ΔA range.

4.2.2 Perpendicular Momentum Distributions

The perpendicular momentum distributions of all 154 fragments were also extracted from the data from NSCL experiment 10501. Six example perpendicular momentum distributions

are shown in Figures 4.13 and 4.14 for the same set of fragment species ^{71}Ga, ^{65}Zn, ^{60}Co, ^{54}Cr, ^{47}Sc, and ^{39}Cl produced from interaction with a beryllium and gold target, respectively, that were depicted in Figures 4.9 and 4.10.

The perpendicular momentum distributions of fragments from the Be target and all fragments with a mass loss of $\Delta A \geq 7$ from the Au target were readily described with a Gaussian function, where the centroid falls at zero perpendicular momentum. The perpendicular momentum distributions of fragments from the Au target with a mass loss of $\Delta A < 7$, on the other hand, were better described by a Gaussian function having a non-zero centroid value. In Figure 4.15 is shown the distributions for all the fragments in the $\Delta A < 7$ region from the Au target. The distributions in Figure 4.15 are peaked away from zero perpendicular momentum. The other trend seen in this set of distributions is a gradual shift of the peak position towards zero perpendicular momentum with an increase in mass loss. The peak position is largest for the fragments with masses nearest the original projectile mass of A=76.

The perpendicular width parameter, $\sigma_{p_\perp}$, of each momentum distribution was deduced from the Gaussian fit procedure. The widths for the perpendicular momentum distributions where the peak value held to zero perpendicular momentum ($\Delta A \geq 7$) are shown as a function of mass loss, ΔA, of the fragment in Figure 4.16. The component of the width parameter associated with the angular resolution of the spectrometer is responsible for the increased counts/sr values at small perpendicular momentum values in the measured fragment perpendicular momentum distributions. This component can be estimated and compared to the measured with to determine the width associated with the scattering of the measured fragment. Table 4.2 contains calculation of the two components of the measured width; σ_{res}, which accounts for the angular resolution, and σ_{nuc}, which is associated with the nuclear

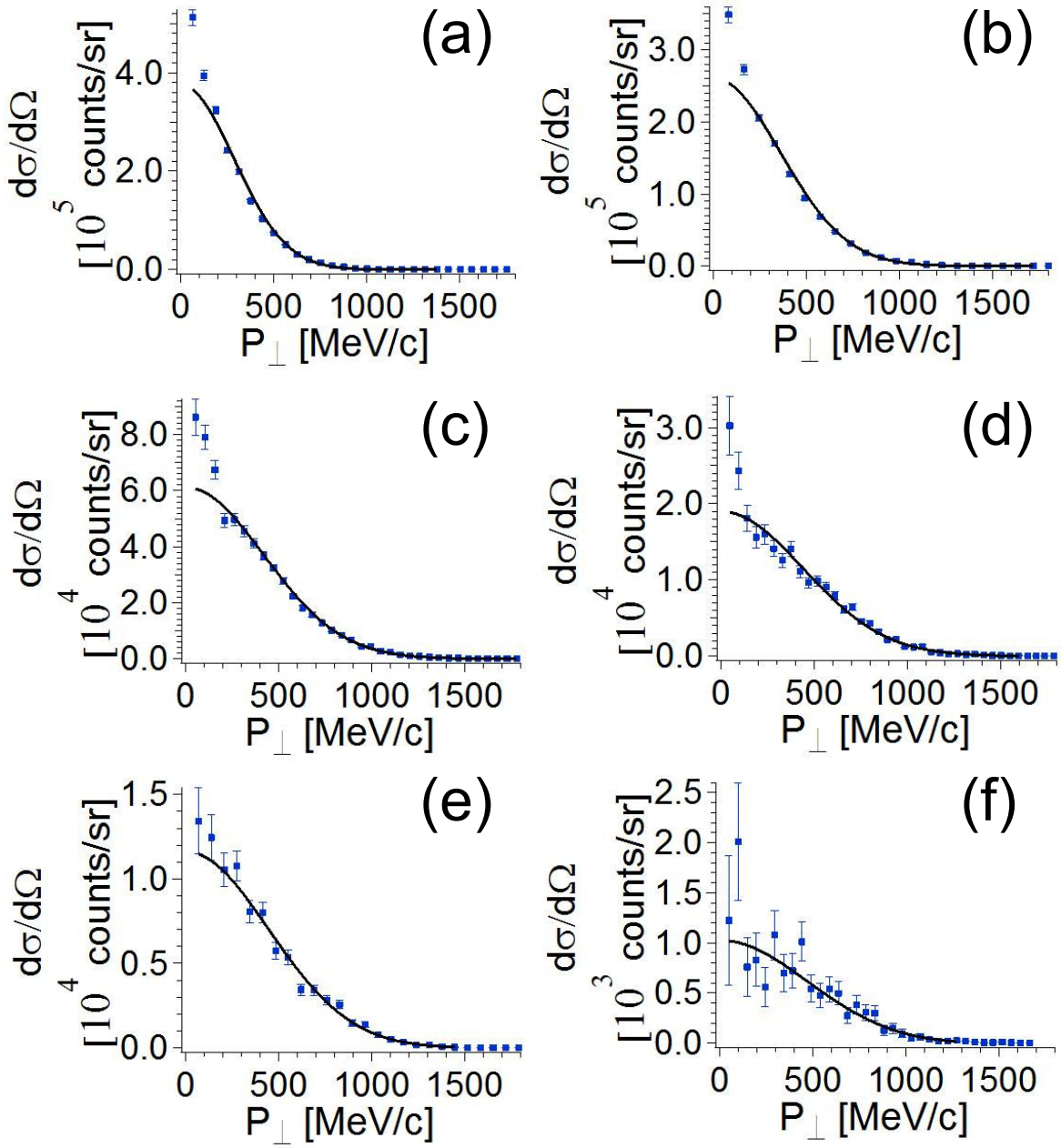

Figure 4.13: Perpendicular momentum distributions for fragments produced from ^{76}Ge on a Be target. (a) ^{71}Ga (b) ^{65}Zn (c) ^{60}Co (d) ^{54}Cr (e) ^{47}Sc (f) ^{39}Cl.

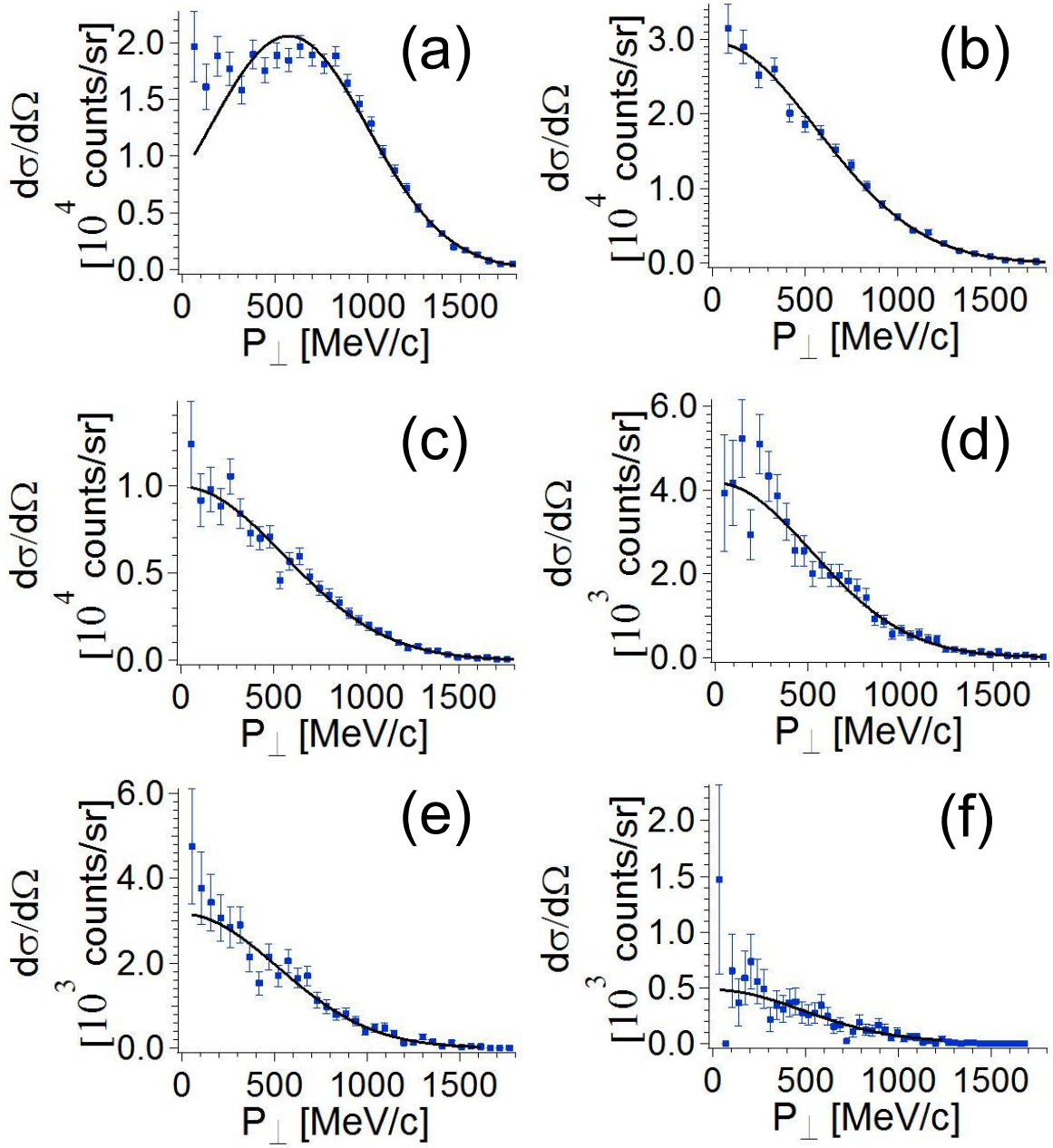

Figure 4.14: Perpendicular momentum distributions for fragments produced from ^{76}Ge on a Au target. (a) ^{71}Ga (b) ^{65}Zn (c) ^{60}Co (d) ^{54}Cr (e) ^{47}Sc (f) ^{39}Cl.

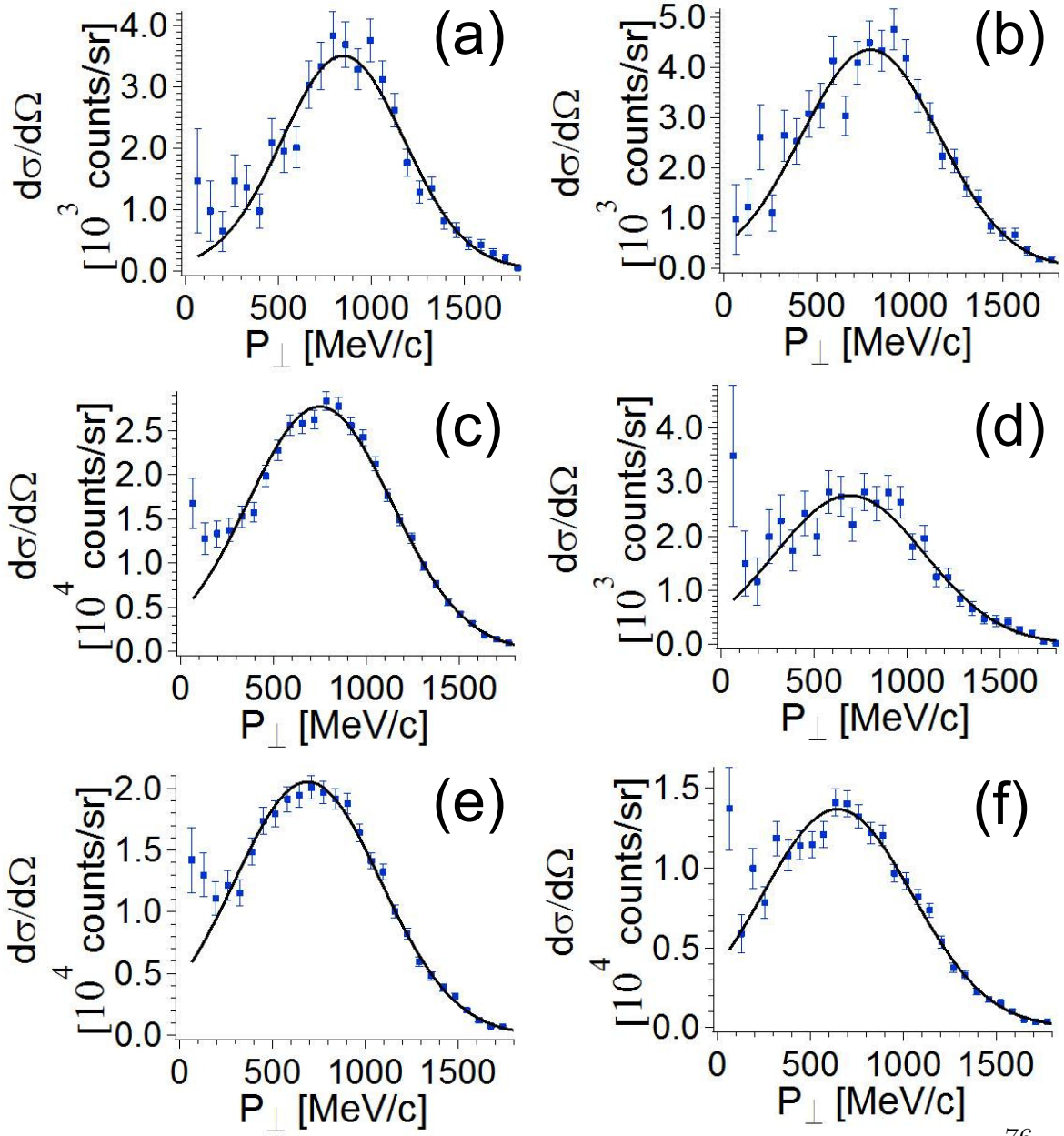

Figure 4.15: Perpendicular momentum distributions for fragments produced from ^{76}Ge on a Au target. (a) ^{74}As (b) ^{73}As (c) ^{73}Ge (d) ^{72}As (e) ^{72}Ge (f) ^{71}Ge.

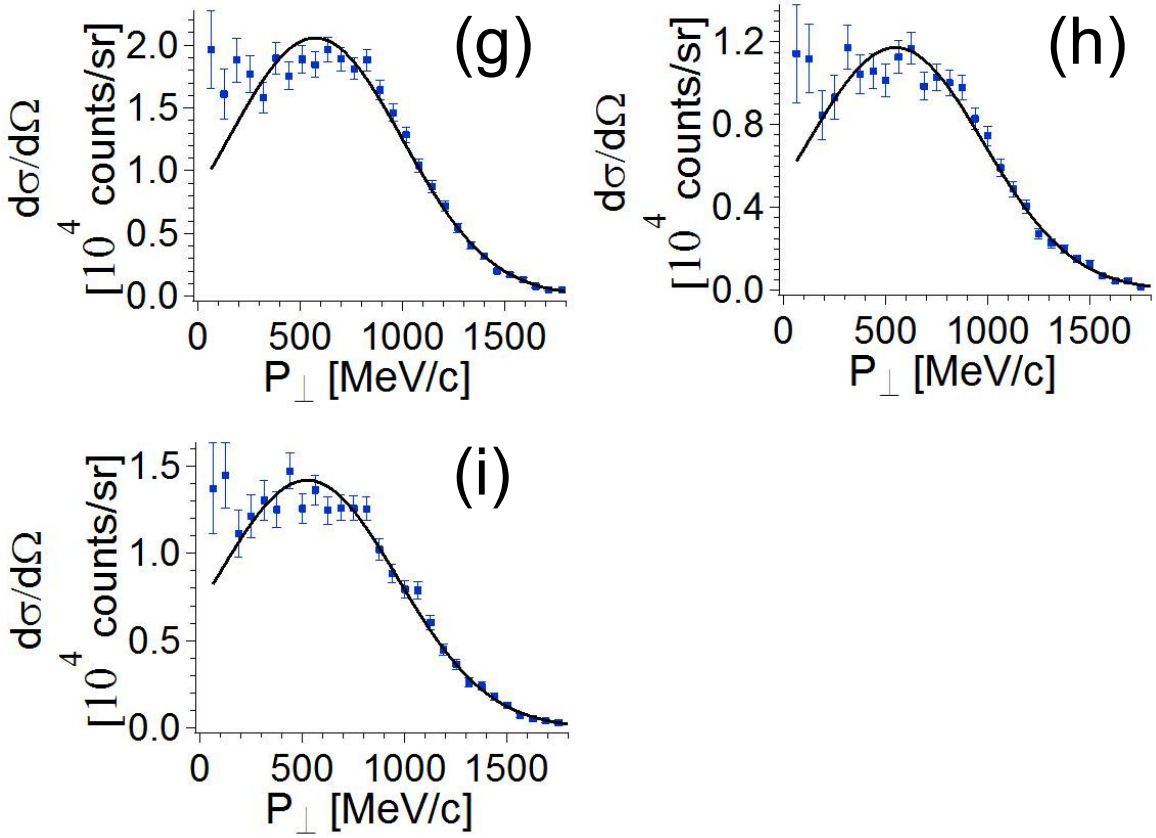

Figure 4.15: continued. Perpendicular momentum distributions for fragments produced from ^{76}Ge on a Au target. (g) ^{71}Ga (h) ^{70}Ge (i) ^{70}Ga.

scattering of the fragment. The relative importance of the angular resolution decreases with increasing fragment mass.

The width values of the perpendicular momentum distributions from the fragments from

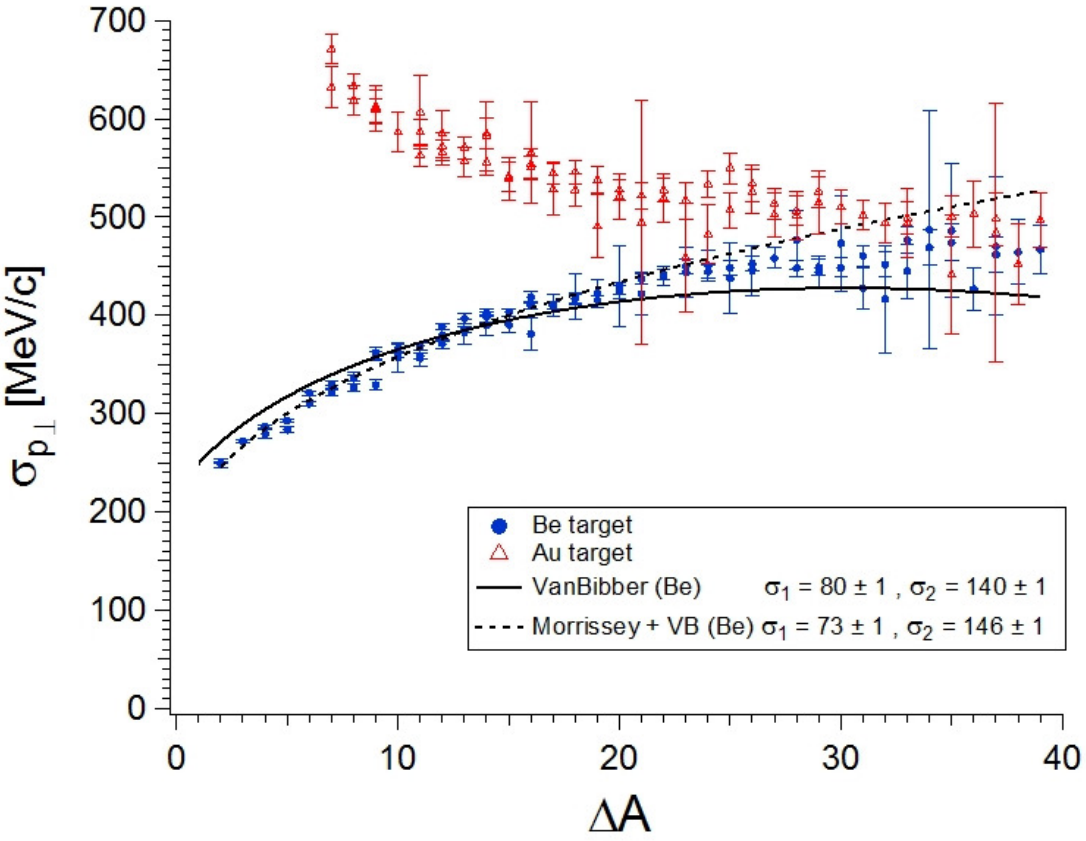

Figure 4.16: Extracted widths of the perpendicular momentum distributions, $\sigma_{p_\perp}$, as a function of the fragment mass loss, ΔA, for two target species, beryllium (circles) and gold (triangles). Solid and dashed lines represent the best fits to the beryllium target data using models from Van Bibber and Morrissey plus Van Bibber's orbital deflection term, respectively, see the text.

the beryllium target data set were compared to two models, that from Van Bibber [18] and Morrissey plus Van Bibber's orbital deflection term. Since the first term in each model is assumed to be a description of the parallel momentum width, the values of the coefficients were held equal to the coefficients from the best fits to the parallel momentum width for each isotope. The resulting values of the the second term of each fitted function were determined

Table 4.2: Components of the measured width, $\sigma_{p_\perp}$, of the perpendicular momentum distributions of a selection of fragments produced with the beryllium target. All values are in units of MeV/c. See text for more details.

Fragment	$\sigma_{p_\perp}$	σ_{res}	σ_{nuc}
^{73}Ge	124	63	106
^{69}Zn	194	60	184
^{60}Co	337	51	333
^{49}Ti	367	42	365

to be $\sigma_1 = 140 \pm 1$ MeV/c for Van Bibber and $\sigma_1 = 146 \pm 1$ MeV/c for Morrissey plus Van Bibber's orbital deflection term.

Chapter 5

Discussion

This chapter presents interpretations of the two main goals of this work; the atomic charge-state identification of fragments by a hodoscope array and the measurement of both components of the linear momentum distribution of the outgoing final products from fragmentation reactions. The performance of the hodoscope in measuring the residual kinetic energy will be discussed in the context of improving the particle identification procedure of S800 experiments by also extracting unique charge states for each element. Two observables used to study fragmentation reactions, the parallel and perpendicular components of the linear momentum of the final products, have been deduced for a large set of fragmentation products produced using both a light mass (Be) and heavy mass (Au) target. Insights gained from the global analysis of the momentum distributions will also be presented.

5.1 Improved Particle Identification

The installation of the hodoscope array provided an important improvement to the particle identification procedure of the S800 spectrograph by adding a third parameter of atomic charge-state based on the measurement of the total residual kinetic energy with the sufficient resolution to uniquely extract q on an event-by-event basis. An energy resolution of better than 3.74% is necessary for evaluating the charge-state separation capabilities of two particles, $^{72}_{31}\mathrm{Ga}^{31+}$ and $^{70}_{31}\mathrm{Ga}^{30+}$, with similar mass-to-charge ratios. The two particles were found to be resolvable using the light and energy resolution capabilities of the hodoscope crystals. As indicated in Chapter 1, the trend of increasing fragment masses studied by experimenters utilizing the S800 increases the likelihood of charge-state production, which will place additional burden for improved particle identification procedure that includes charge-state identification. The new hodoscope was shown to provide the necessary energy resolution to properly extract q for particle identification, thus providing an avenue to separate unwanted charge-states during isotope identification. In Table 5.1 are continued example fragments and their overlapping hydrogen-like intrusion pair for a range of particle masses that should be separable using the hodoscope based on deduced intrinsic crystal resolution of 0.30% in light output.

5.2 Linear Momentum as an observable to fragmentation reactions

The linear momentum of the outgoing fragments from a fragmentation reaction is an important observable that has been studied to understand the reaction mechanism(s) of the

Table 5.1: Example fragment pairs with approximately equal A/q ratios and calculated energy and light separations. Energy separation values calculated with a 3.5 Tm magnetic rigidity. Light separation values calculated with crystal number 10 response function coefficients.

Fragment Pair	A/q	Energy separation (%)	Light separation (%)
$^{72}_{31}Ga^{31+}$, $^{70}_{31}Ga^{30+}$	2.325	3.74	1.31
$^{92}_{40}Zr^{40+}$, $^{90}_{40}Zr^{39+}$	2.3	2.88	1.09
$^{116}_{50}Sn^{50+}$, $^{114}_{50}Sn^{49+}$	2.325	2.30	0.90
$^{78}_{31}Ga^{31+}$, $^{76}_{31}Ga^{30+}$	2.485	3.96	1.32
$^{98}_{40}Zr^{40+}$, $^{96}_{40}Zr^{39+}$	2.455	3.00	1.09
$^{126}_{50}Sn^{50+}$, $^{124}_{50}Sn^{49+}$	2.525	2.44	0.89

fragmentation process. The other orthogonal component of the linear momentum, the perpendicular momentum distributions, have been studied less well than the parallel momentum distribution. Data have been collected for both components for a large number of fragmentation products following the interaction of a ^{76}Ge primary beam in targets of Be or Au.

5.2.1 Parallel Momentum Observables

The parallel momentum distributions of fragmentation products have been deduced and presented in Figures 4.9, 4.10 and Appendix A. The widths of the distributions have been determined based on a fit to a Gaussian function and are shown in Figure 4.11. The widths were first separated by target and no dependence of the width on the target was evident. The target data sets were then combined and compared to the models by Goldhaber [24] and Morrissey [36]. The best fit to each model resulted in σ_0 values slightly smaller than those originally reported by Goldhaber and Morrissey. In Table 5.2 was compared the σ_0 derived in the current work with other published values. The original model by Goldhaber

Table 5.2: Coefficient values in units of MeV/c resulting from application of Goldhaber (G) and Morrissey (M) models to a variety of data sets in the literature. Multiple coefficient values correspond to the multiple target or energies of the corresponding reaction.

Ref	Reaction	Energy/nucleon	σ_0(G)	σ_0(M)
[24]	^{16}O + Be	2.1 GeV	90	
[17]	^{12}C,^{16}O + Be-Pb	1.05,2.1 GeV	71,86	
[19]	data from [17]	data from [17]	103,104	
[20]	^{40}Ar + ^{68}Zn	27.6 MeV	109	
[7]	^{40}Ar + ^{40}Ca	27,44 MeV	95,85	
[7]	^{20}Ne + ^{208}Pb	44 MeV	45	
[23]	^{86}Kr + ^{27}Al	70 MeV	124	120
[36]	data from [17]	data from [17]		94
this work	^{76}Ge + ^{9}Be,^{197}Au	130 MeV	80	73

calculated the coefficient σ_0 from the Fermi momentum of the projectile. The σ_0 value reported in the present work was treated as an independent fitting parameter, similar to past applications of this model [20,23,28], and is approximately 30% smaller than predicted using the Fermi momentum from Moniz [26]. The applied functions described the data equally well for the mass loss range, with no 'best' model based on overlapping reduced χ^2 values. The largest value of ΔA analyzed in this work was $\Delta A = 39$, one value above $A_{projectile}/2$, which is the mass loss value corresponding to the turnover point or maximum width predicted by the Goldhaber model. On the other hand, the description by Morrissey continues to grow with increasing mass loss. Fragments with mass losses above $\Delta A = 39$ where the two models begin to diverge, were not produced in sufficient quantities in this work for the parallel momentum distributions to be analyzed. At the opposite end of the mass loss range, fragments with one more proton than the beam were observed here, and the widths of the

parallel momentum distributions of fragments ^{74}As, ^{73}As, and ^{72}As have been included in Figure 4.11. These fragments were not produced by a pure fragmentation reaction, as projectile fragmentation does not include proton pickup by the projectile. However, the deduced widths are in agreement with the predictions of both empirical models. Finally, an analysis of the momentum width as a function of mass loss, where the fragments were grouped by isobaric chains, showed no dependence of the width to the atomic number, Z, of the fragment.

The parallel momentum transfer or down-shift was determined from the peak value of each parallel momentum distribution and was presented in Chapter 4 for each target. The linear relationship observed for the momentum transfer with mass loss, which matches the previous results from Morrissey [36] and Pfaff [23], reflects the energy necessary to remove the bound nucleons from the projectile. The present slopes of 6.2 and 4.8 MeV/c for the beryllium and gold targets, respectively, are smaller than the value of 8 MeV/c reported by Morrissey and 8.8 MeV/c reported by Pfaff. A "levelling off" of the momentum transfer at larger mass loss is evident for the Be target data, and matches results initially reported by Morrissey. No levelling off was observed in the gold target data set. An analysis of the individual isotopic chains (indicated by the solid lines in Figure 4.12), similar to the analysis performed by Pfaff [23], showed that the slope parameters for individual elements were larger than the overall average slope. This result is similar to Pfaff's observation for proton-rich fragments from ^{86}Kr, where the primary beam was at a lower energy of 70 MeV/nucleon. Also evident in Figure 4.12 was the constant slope values of the isotope chains with atomic numbers Z=33 down to Z=27. However, the offset needed to describe the fragments with more protons than the projectile in Pfaff's work was not observed in this work.

5.2.2 Perpendicular Momentum Observables

The perpendicular momentum distributions of fragmentation products were determined and shown in Figures 4.13, 4.14 as well as in Appendix A. The widths of the perpendicular momentum distributions were also deduced from a Gaussian fit to $p_\perp$ and presented in Figure 4.16. The widths of the perpendicular momentum distributions were also separated based on target species. A clear difference in the $\sigma_{p_\perp}$ was evident for fragments from a beryllium target versus those produced in the gold target. The perpendicular widths from the beryllium target were described well by the empirical models of Van Bibber [18] and Morrissey [36] plus Van Bibber's orbital deflection term. This agreement is depicted in Figure 4.16. The coefficients resulting from the best fits of the models to the data are given in Table 5.3, with 'fixed' coefficients obtained after fixing the σ_0 coefficient value to the value from the parallel momentum distribution and the 'free' coefficients obtained from allowing both coefficient values to remain as free parameters in the fitting process. Allowing 'fixed' or 'free' σ_0 values resulted in similar values for the best fits with each model and implies that the width of the parallel momentum distribution is an important component of the width of

Table 5.3: Coefficient values σ_0 and σ_1 in units of MeV/c resulting from application of models from Van Bibber and Morrissey + Van Bibber's second term (Morrissey + VB). 'Fixed σ_0' coefficient values were obtained after fixing the σ_0 coefficient value to the values obtained in parallel momentum distribution width fitting process. 'Free σ_0' values were obtained after allowing both coefficients to be free parameters in the fitting process.

	fixed σ_0		free σ_0	
Ref	σ_0	σ_1	σ_0	σ_1
Van Bibber	80 ± 1	140 ± 1	86 ± 1	125 ± 1
Morrissey + VB	73 ± 1	146 ± 1	70 ± 1	155 ± 1

the perpendicular momentum distribution.

The perpendicular momentum distributions of fragments produced with the heavier gold target do not agree with Van Bibber's model for mass losses ΔA<20. An assumption made by Van Bibber of a uniform scattering of the fragment around the target periphery implies that the resulting perpendicular momentum distribution should peak along the beam direction. This assumption validated fragments produced in the beryllium target in the present work, and for fragments produced with ΔA>20 in the gold target. However, the $\sigma p_{\perp}$ for fragments with ΔA<7 show an anomaly. The perpendicular momentum distributions for fragments in this mass region presented in Figure 4.15 show two unique characteristics. The peaks of the perpendicular distributions are not centered at zero momentum and the peak positions of the distributions shift systematically to zero momentum as the fragment mass decreases. Both of these characteristics suggest that the assumption of uniform scattering of the fragment on the target made by Van Bibber may not be true for fragments near the projectile.

The scattering process should be reconsidered at these bombarding energies and a model that to better describe the reaction process leading to the production of fragments with ΔA<7 in heavy targets developed. The classical deflection angle, θ, as a function of impact parameter, b, was calculated using the following function from Bertulani and Danielewicz [62] to describe the scattering between the fragment and target:

$$\theta(b) = \pi - 2\int_{R_{ca}}^{\infty} \frac{b}{r^2\sqrt{1 - b^2/r^2 - V(r)/E}} dr. \tag{5.1}$$

In Equation 5.1, r is the radial distance between the fragment and target, R_{ca} is the radius of closest approach which in this case is taken to be the sum of the fragment and target radii, and $V(r)$ is the interaction potential between the two nuclei. The interaction potential used here was the repulsive Coulomb potential and an attractive nuclear potential. The Coulomb

potential follows the well-known equation:

$$V_{Coulomb}(r) = \frac{Z_1 Z_2 e^2}{r} \tag{5.2}$$

where Z_1 is the atomic number of the projectile, Z_2 is the atomic number of the target, and $e^2 = 1.44$ *MeV-fm*. The nuclear potential was approximated by the 'proximity' potential of Blocki *et al* [63] that treats the two nuclei involved as gently curved surfaces separated by a small gap which creates an attractive force between the two surfaces and is determined by the average radius of the two nuclei. The equation for the potential is:

$$V_{proximity}(r) = 4\pi\gamma\overline{R}b\Phi(\xi) \tag{5.3}$$

where $b = 1$ fm is the width of the potential, $\gamma = 0.9517[1 - 1.7826I^2]$ MeV/fm^2 is a surface energy coefficient (where $I = (N - Z)/A$ where N, Z, and A refer to the combined system of the two interacting nuclei, see Reference 28 in [63]), $\overline{R}$ is the mean curvature of the radius of the gap between the interacting nuclei defined as:

$$\overline{R} = \frac{C_1 C_2}{C_{1+} C_2} \tag{5.4}$$

with $C_i = R_i - 1/R_i$ as the central radius of the nucleus i using the parametrization $R = 1.28A_i^{1/3} - 0.76 + 0.8A_i^{-1/3}$. Finally, the 'cubic-exponential' function, $\Phi(\xi)$, is defined differently for different values of ξ (see Reference 27 in [63]):

$$\begin{aligned} \Phi(\xi \leq \xi_1) &= -\frac{1}{2}(\xi - \xi_0)^2 - k(\xi - \xi_0)^3 \\ \Phi(\xi \geq \xi_1) &= -3.437exp(-\xi/0.75) \end{aligned} \tag{5.5}$$

where $\xi_1 = 1.2511$, $\xi_0 = 2.54$, and $k = 0.0852$. The variable ξ_1 represents the transition between the two nuclei approaching and the two nuclei overlapping which also results in the anomaly at approximately r=12 fm in the proximity and total potentials shown in Figure 5.1.

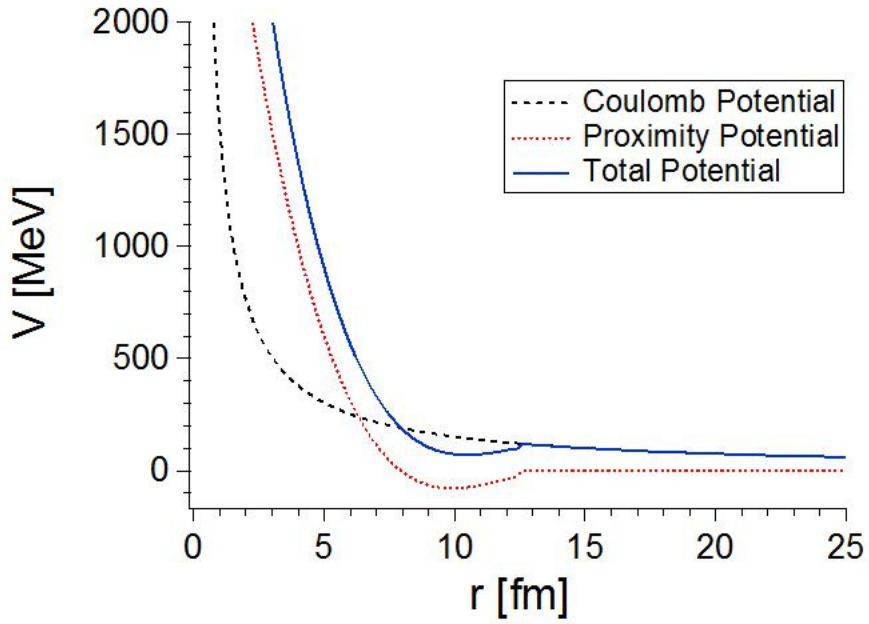

Figure 5.1: Interaction potentials applied in calculation of classical scattering angle of ^{74}As fragment on a ^{197}Au target. Total potential (solid line) is a summation of the Coulomb (dashed line) and the proximity (dotted line) potentials.

Equation 5.3 including the parametrizations listed above and in equations 5.4 and 5.5 were applied by Blocki *et al* to reaction systems similar to the current work including ^{40}Ar+^{121}Sb and ^{84}Kr+^{209}Bi [63].

The Coulomb and proximity potentials were added and inserted into V(r) of equation 5.1. In Figure 5.1 the variation of each potential and the sum as a function of distance, r, between a ^{74}As fragment and the ^{197}Au target is shown. The classical deflection angle was calculated for all fragments with a ΔA<7; ^{74}As, ^{73}As, ^{73}Ge, ^{72}As ^{72}Ge, ^{71}Ge, ^{71}Ga, ^{70}Ge, and ^{70}Ga. The result of each calculation is presented in Figure 5.2 along with the observed peak scattering angle for each fragment. The observed peak scattering angle in Figure 5.2 intersects the classical deflection function three times. However for the occasion the crossover occurs at radii larger than the sum of the two nuclear radii as defined by Blocki $(R_1 + R_2)$ [63]. The two outer points of intersection, labeled 'C' and 'N+C', correspond

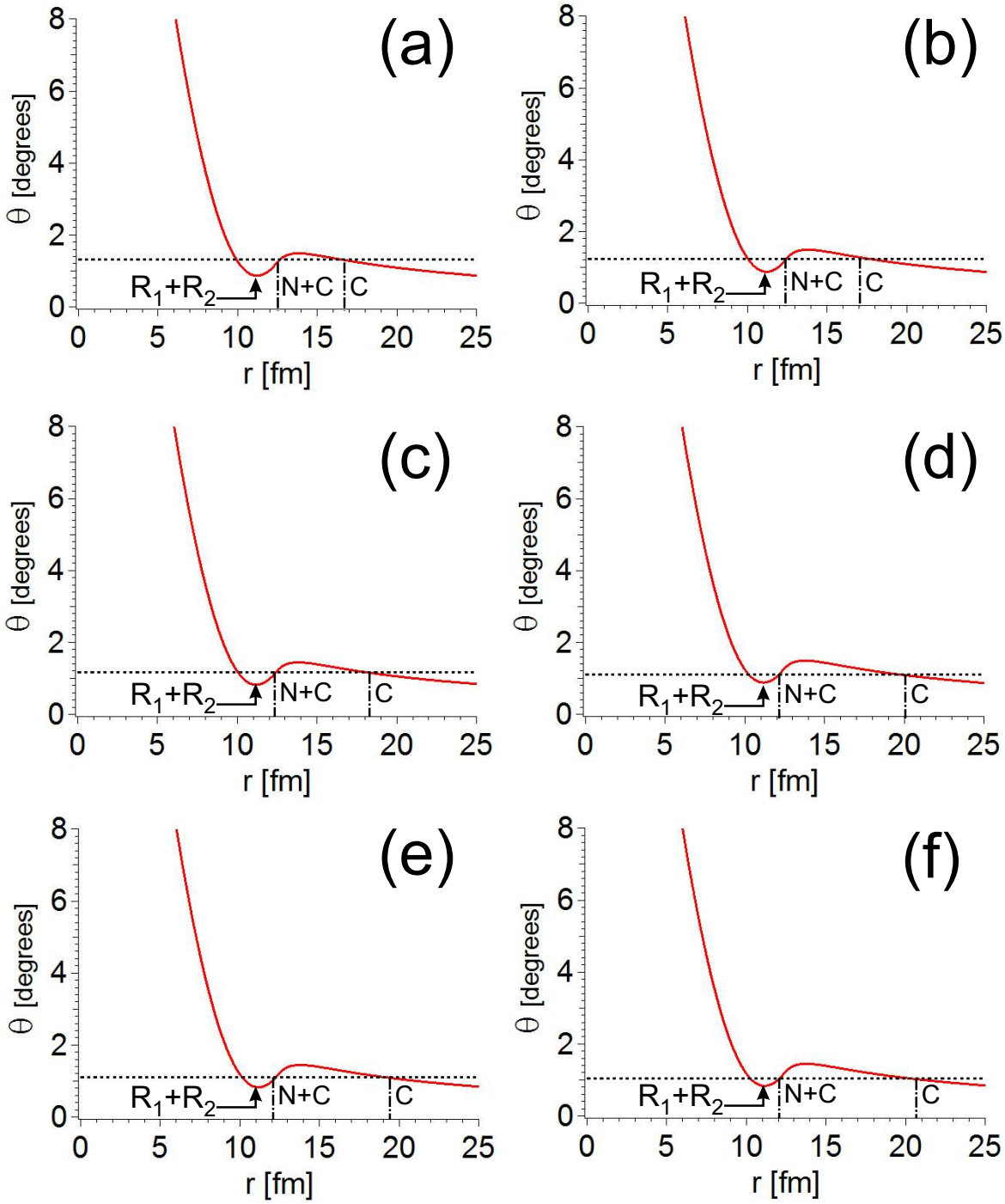

Figure 5.2: Calculated deflection angle as a function of impact parameter (solid lines). The dashed lines are the observed peak scattering angle for each fragment. The 'N+C' and 'C' labels refer to impact parameters associated with nuclear plus Coulomb and pure Coulomb scattering. (a) ^{74}As (b) ^{73}As (c) ^{73}Ge (d) ^{72}As (e) ^{72}Ge (f) ^{71}Ge.

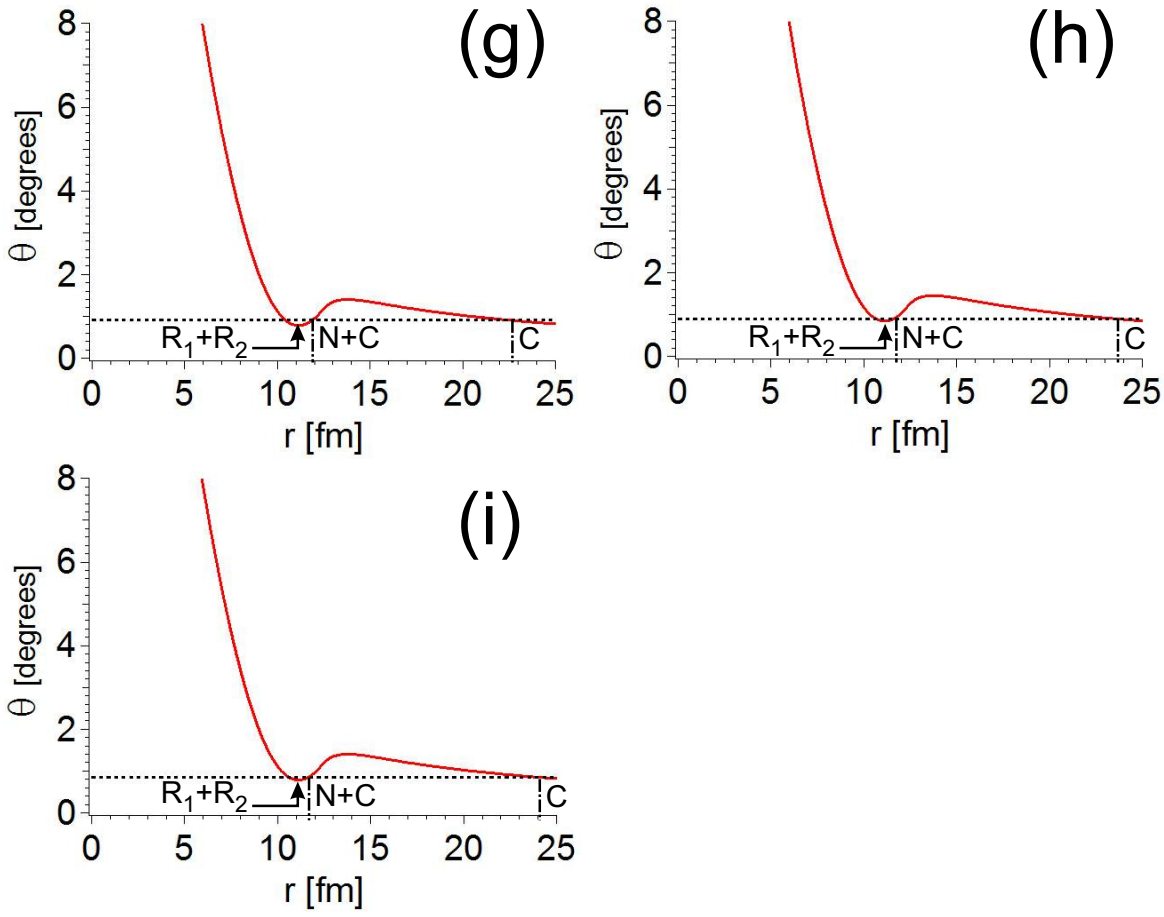

Figure 5.2: continued. Calculated deflection angle as a function of impact parameter (solid lines). The dashed lines are the observed peak scattering angle for each fragment. The 'N+C' and 'C' labels refer to impact parameters associated with nuclear plus Coulomb and pure Coulomb scattering. (g) ^{71}Ga (h) ^{70}Ge (i) ^{70}Ga.

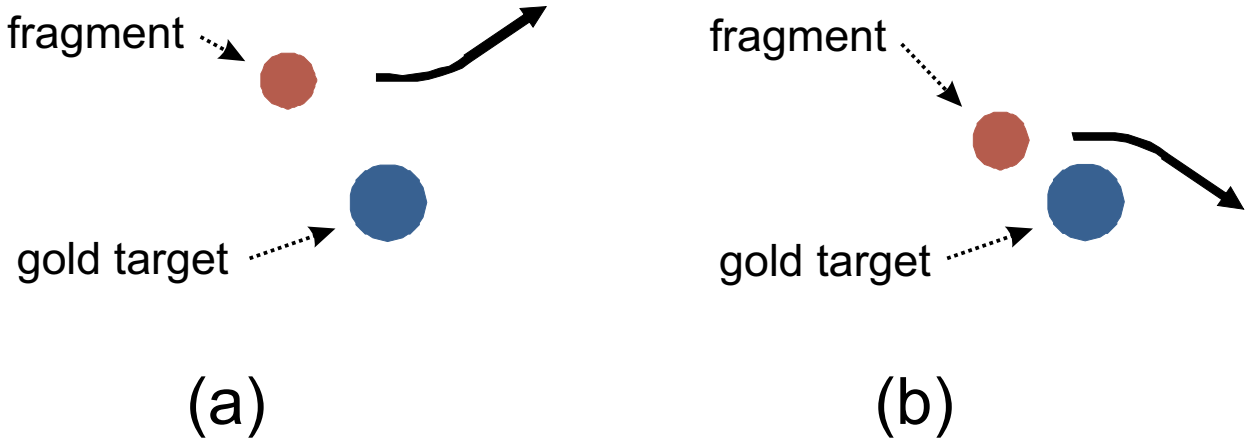

Figure 5.3: Cartoon schematic of a fragment scattering on a gold target (a) due to pure Coulomb potential resulting in 'same-side' scattering or (b) due to nuclear plus Coulomb potential resulting in 'far-side' scattering.

to the impact parameters for scattering of the fragment by the target due to the Coulomb potential alone and due to the nuclear plus Coulomb potentials. A schematic cartoon of the two scattering scenarios is shown in Figure 5.3. The larger impact parameter, labeled 'C', corresponds to 'same-side' scattering due to the long range repulsive Coulomb potential. The smaller impact parameter, labeled 'N+C', corresponds to 'far-side' scattering due to a combination of the Coulomb potential and the shorter range much stronger attractive nuclear potential. The two impact parameters for each fragment with $\Delta A<7$ calculated using the classical deflection function are shown as a function of fragment mass loss in Figure 5.4, along with the corresponding combined radius, $R_1 + R_2$, for each fragment with the gold target. The trends that emerge from Figure 5.4 for each set of impact parameters include the increase in value as the number of nucleons removed increases for the set of larger impact parameters associated with pure Coulomb scattering. The opposite trend occurs with the set of smaller valued impact parameters associated with nuclear plus Coulomb scattering decreases as the number of nucleons removed increases, approaching the sum of the radii. More importantly, the large separation between the fragment and target in a pure

Coulomb scattering would preclude the overlap of nuclear densities necessary for producing the observed fragment species. This excludes pure Coulomb scattering as the source of the observed perpendicular momentum distributions of the heaviest fragments produced with the gold target. On the other hand, the evolution of the set of impact parameters for the nuclear plus Coulomb scattering is close to the sum of the radii and follows the progression of the measured decrease in scattering angle with increasing ΔA. This trend also matches the trend in decreasing perpendicular momentum distribution width values with increasing ΔA. As the number of nucleons removed increases, the collision becomes more central and the final fragment has a perpendicular momentum distribution that is better described by the Van Bibber model. The smooth transition from scattering caused by a combined nuclear plus Coulomb interaction near the sum of the nuclear radii to overlapping nuclear densities resulting in fragmentation products with perpendicular momentum distributions peaked at zero momentum. This is well supported by both the transition within the measured width values of the perpendicular distributions and the transition within the impact parameters resulting from a calculation of the classical deflection angle associated with the interacting nuclei.

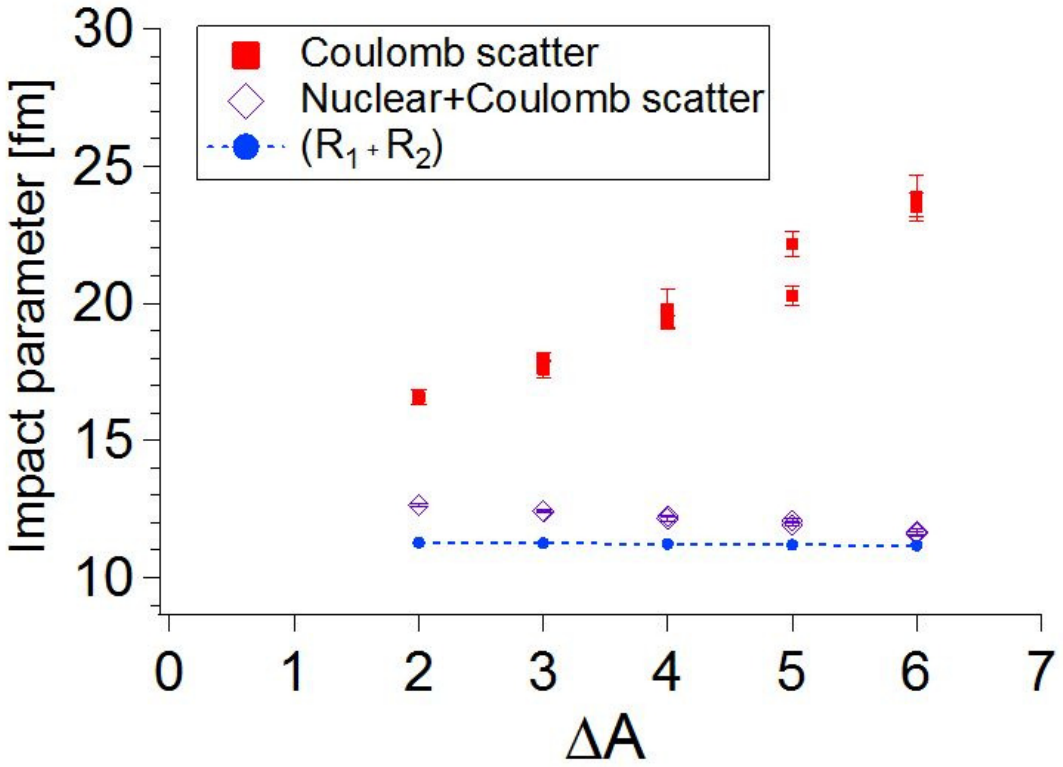

Figure 5.4: Calculated impact parameters as a function of projectile mass loss ΔA, associated with measured scattering angles for the heaviest fragments from a gold target.

Chapter 6

Conclusion

6.1 Summary

The linear momentum of final products are a well-established observable of the fragmentation reaction mechanism and was the main focus of this work. In particular, the determination of both the parallel and perpendicular momentum distributions was accomplished for final products from fragmentation reactions of a ^{76}Ge beam at 130 MeV/nucleon in either a beryllium or gold target. The widths and centroids of the parallel and perpendicular components of the momentum distribution have been reported as a function of fragment mass loss for a set of fragments covering large ranges in mass (37<A<75), nuclear charge (17<Z<33)and energy (3.60 GeV<TKE<7.60 GeV).

The parallel momentum distributions, used to determine both centroid and width values, were found to agree with earlier work. The parallel momentum transfer, calculated from the distribution centroid, was determined to have a linear dependence on fragment mass loss with a best fit slope value similar to published values. The widths of all the fragment par-

allel momentum distributions were also found to follow established empirical descriptions. The choice of target did not have an effect on the parallel distribution widths. The two models that the data were compared to with equal success differed in the dependent variables. Goldhaber's model included terms for both the projectile mass and fragment mass loss masses while Morrissey's model only considered the fragment mass loss [24, 36]. The models begin to diverge at $\Delta A = A_{projectile}/2$, which is near the limit of ΔA for this data set. The extension of parallel momentum width measurements to larger ΔA values would be of interest for future measurements, particularly to discern the relevance of the dependent variables employed by each model.

The perpendicular momentum distributions were also analyzed for width values and, unlike the parallel width values, were found to depend on the target species. The perpendicular widths of the heaviest fragments produced with the gold target suggest a deflection of the fragment by the gold nuclei. This result contrasts with perpendicular distribution width results of fragments produced with the light beryllium target and fragments with ΔA>20 using the gold target, which follow previously published descriptions of the perpendicular width as a function of mass loss. The measured scattering angles for the heaviest fragments from the gold target were found to agree with predictions from a qualitative calculation of the classic deflection angle as a function of the reaction impact parameter. The impact parameter, corresponding to the measured peak scattering angle, calculated from a combination of nuclear and Coulomb potentials were found to be very near the sum of the radii ($R_1 + R_2$) and decreases as the number of nucleons removed increases. This evolution of decreasing impact parameter agrees with the evolution of the measured scattering angle towards zero degrees.

A new hodoscope array of CsI(Na) crystals was installed in the focal plane of the S800 spectrometer to measure the total kinetic energy of incoming particles. The improved energy resolution of this device has provided an independent determination of the atomic-charge state of the particle. The identification of the atomic-charge state adds an additional parameter to the particle identification procedure utilized by experimenters.

6.2 Outlook

The data presented in this work provide the linear momentum distribution of fragmentation products in the fragmentation mechanism transition region. The new perpendicular momentum distribution data adds important information to a previously under-measured observable to the study of the fragmentation process and can serve as a test to more detailed theoretical calculations of the mechanism in the studied projectile energy regime. The data can also be practical for the numerous facilities utilizing projectile fragmentation as a method for rare isotope beam production. Possible future experiments can expand the work presented here to more projectile and target nuclei that will continue to fill in the picture of near projectile mass fragment interactions with a heavy target.

The installation and characterization of the hodoscope will provide future experimenters with improved total kinetic measurements as well as an additional parameter in the particle identification procedure.

APPENDICES

Appendix A

Measured Momentum Distributions

The parallel and perpendicular momentum distributions for fragments produced from a ^{76}Ge beam at 130 MeV/nucleon on either a ^{9}Be or ^{197}Au target are presented herein. In Figures A.1 through A.11 are given the parallel momentum distributions and in Figures A.12 through A.22 are given the perpendicular momentum distributions for fragments ^{74}As through ^{37}Cl produced in a beryllium target. In Figures A.23 through A.31 are given the parallel momentum distributions and in Figures A.32 through A.40 are given the perpendicular momentum distributions for fragments ^{74}As through ^{37}Cl produced in a gold target.

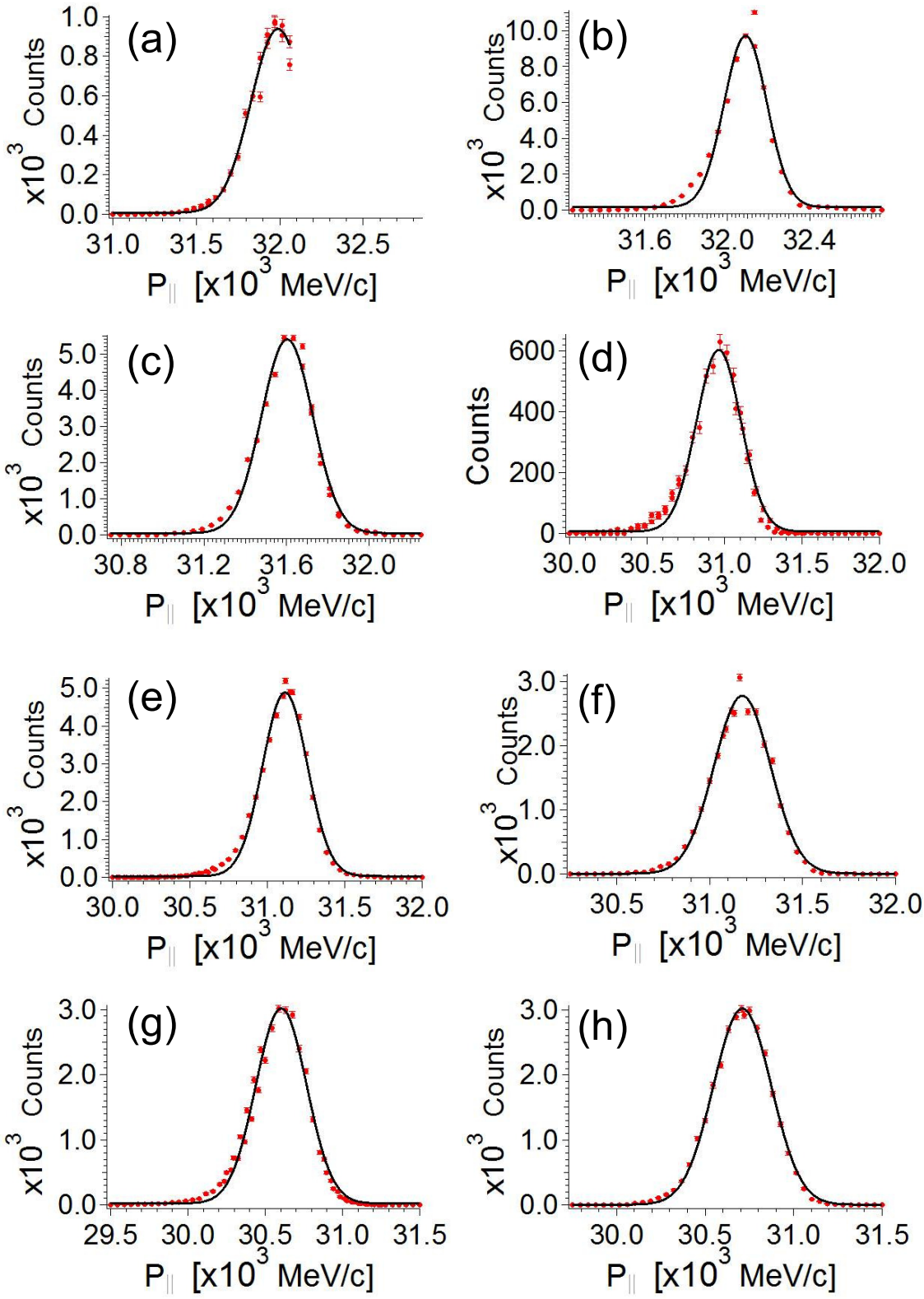

Figure A.1: Parallel momentum distributions for fragments produced from ^{76}Ge on a Be target. (a)^{74}As (b)^{74}Ge (c)^{73}Ge (d)^{72}As (e)^{72}Ge (f)^{72}Ga (g)^{71}Ge (h)^{71}Ga

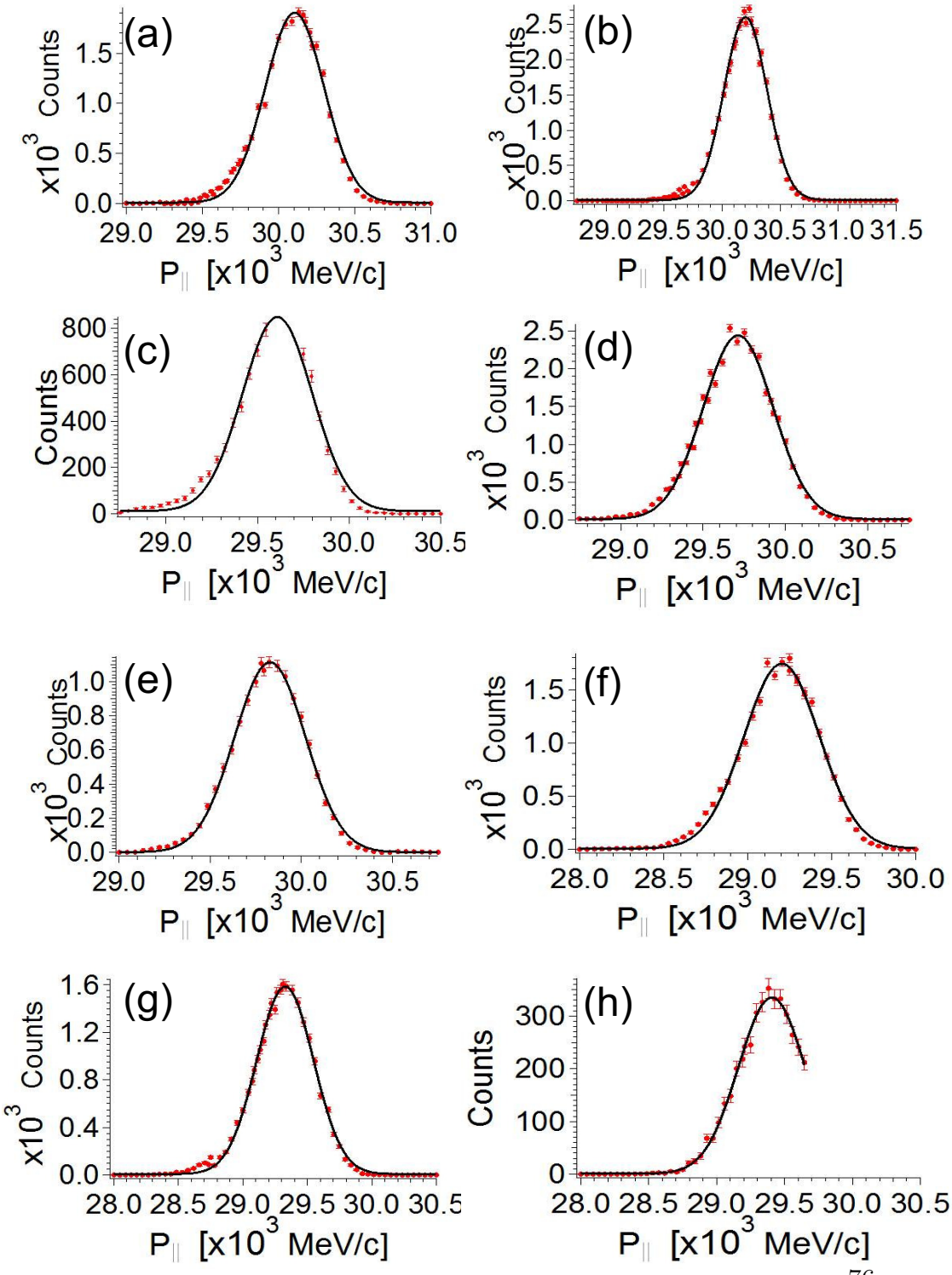

Figure A.2: Parallel momentum distributions for fragments produced from ^{76}Ge on a Be target. (a)^{70}Ge (b)^{70}Ga (c)^{69}Ge (d)^{69}Ga (e)^{69}Ge (f)^{68}Ga (g)^{68}Zn (h)^{68}Cu

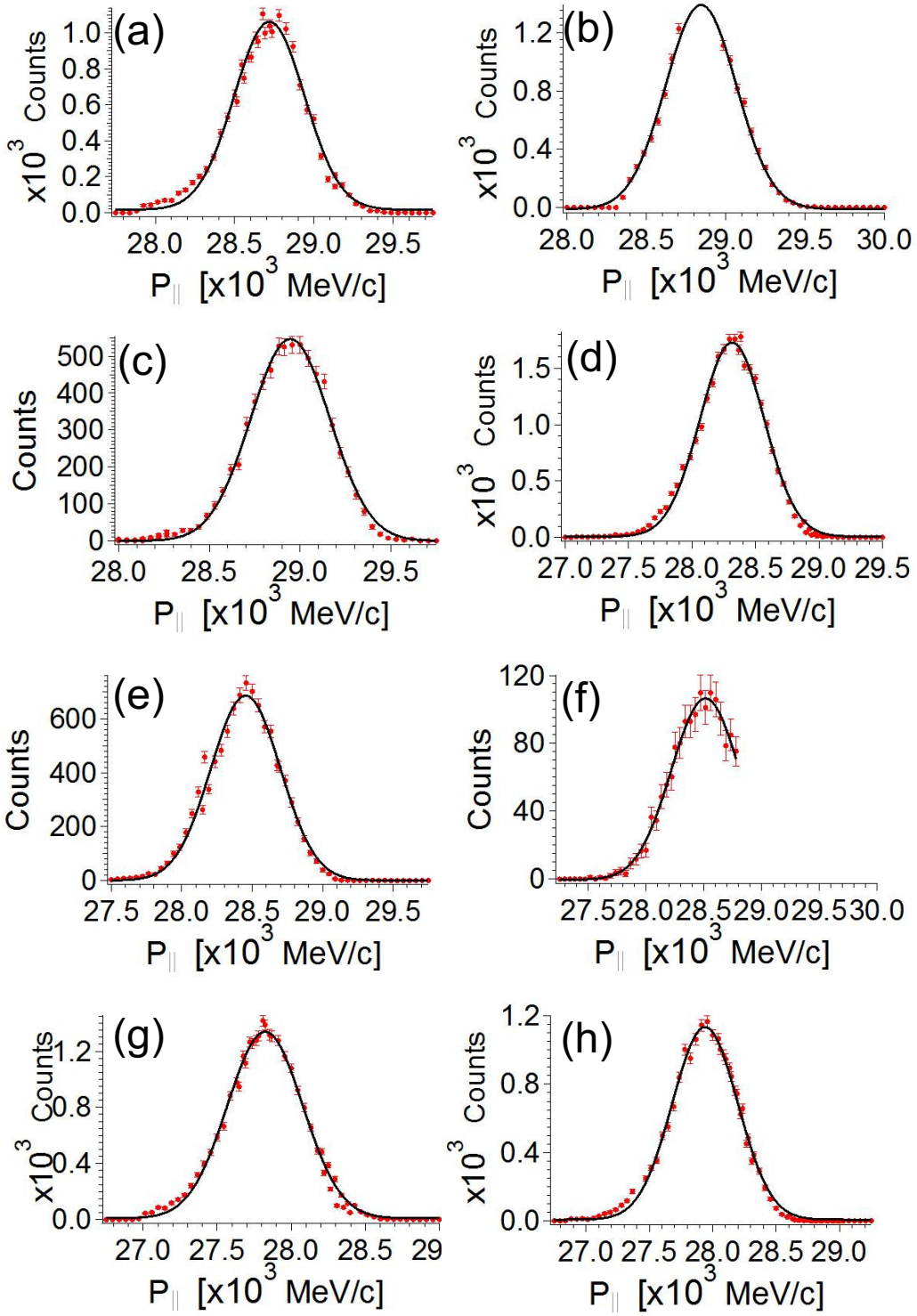

Figure A.3: Parallel momentum distributions for fragments produced from ^{76}Ge on a Be target. (a)^{67}Ga (b)^{67}Zn (c)^{67}Cu (d)^{66}Zn (e)^{66}Cu (f)^{66}Ni (g)^{65}Zn (h)^{65}Cu

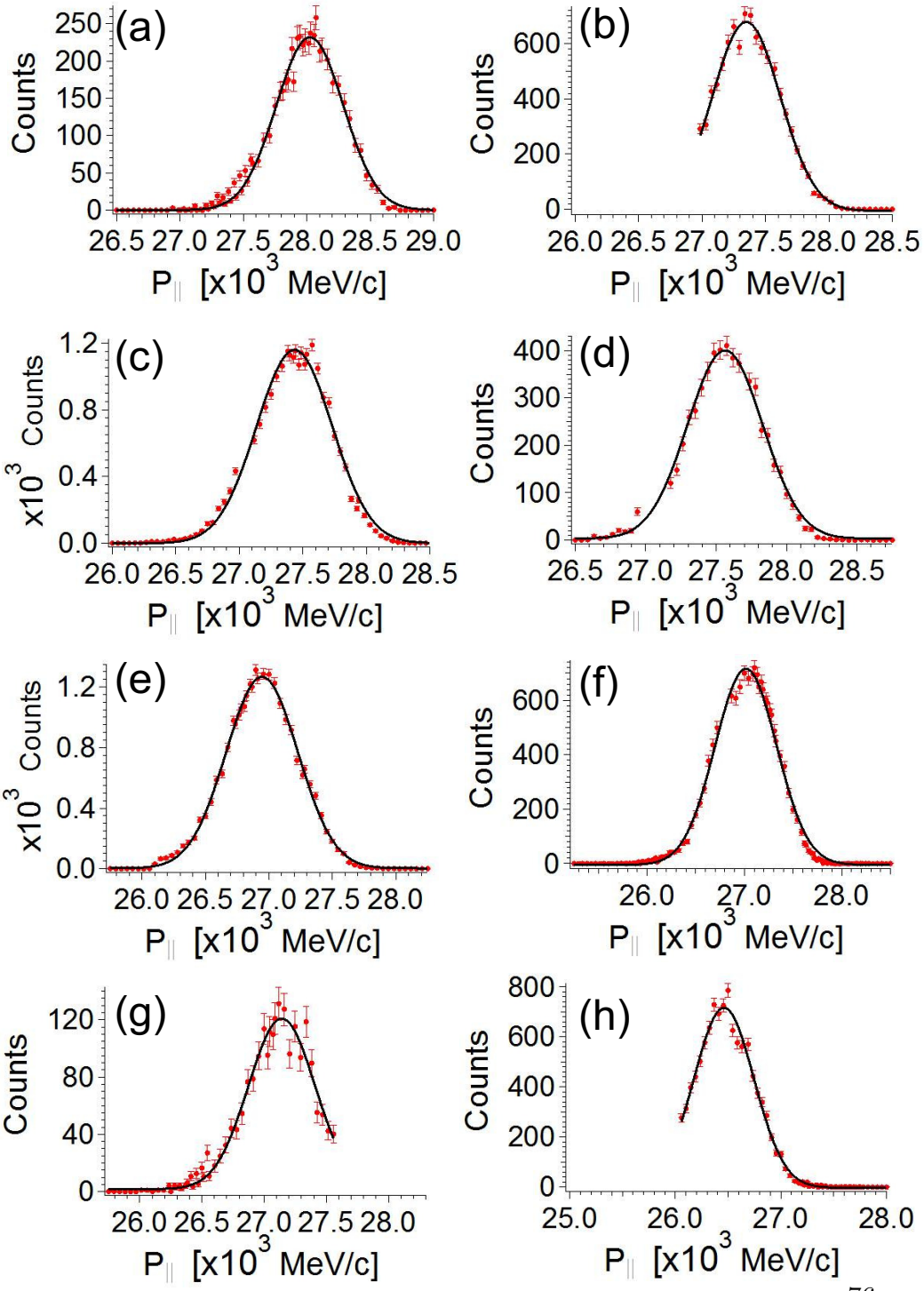

Figure A.4: Parallel momentum distributions for fragments produced from ^{76}Ge on a Be target. (a)^{65}Ni (b)^{64}Zn (c)^{64}Cu (d)^{64}Ni (e)^{63}Cu (f)^{63}Ni (g)^{63}Co (h)^{62}Cu

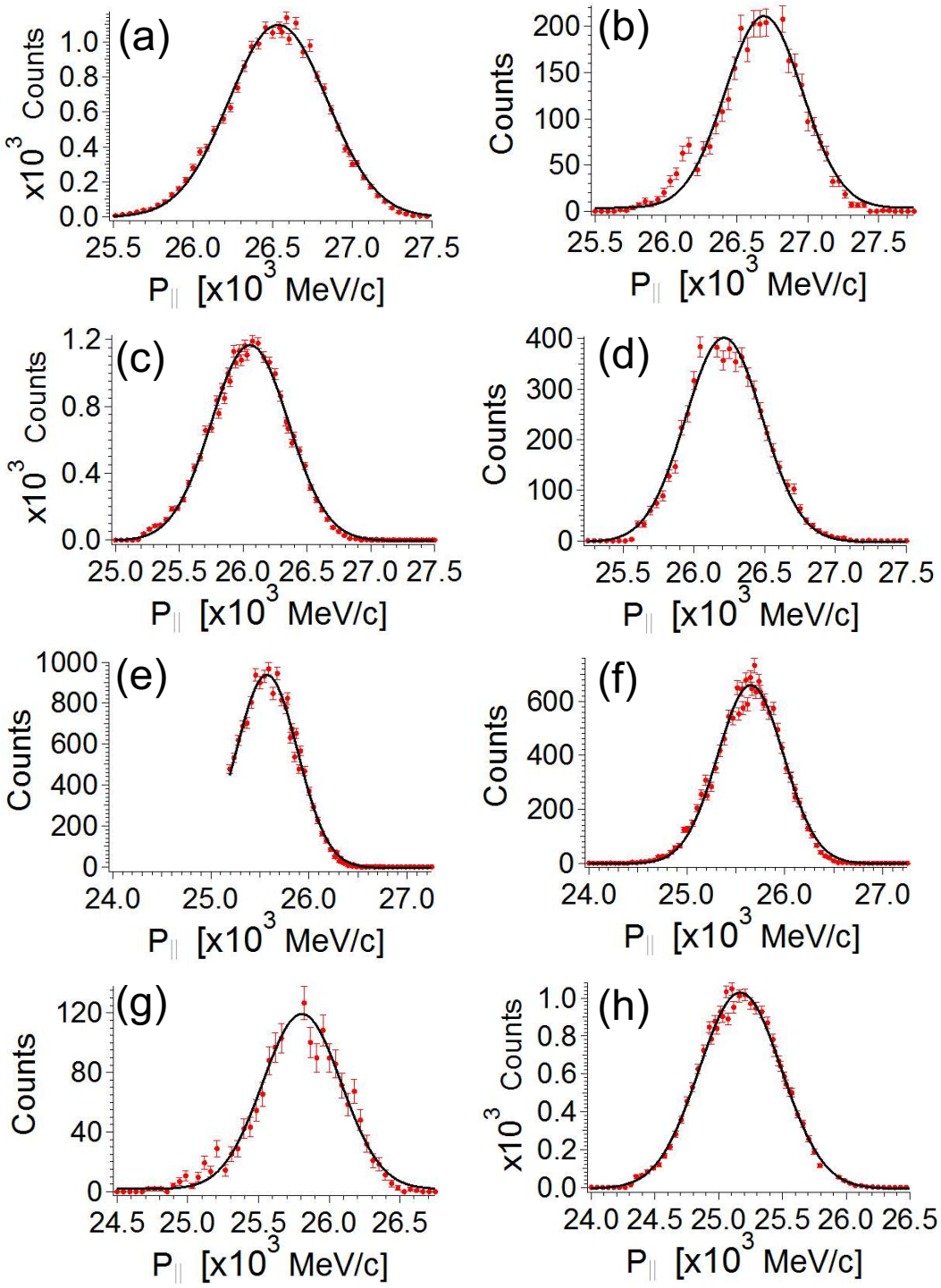

Figure A.5: Parallel momentum distributions for fragments produced from ^{76}Ge on a Be target. (a)^{62}Ni (b)^{62}Co (c)^{61}Ni (d)^{61}Co (e)^{60}Ni (f)^{60}Co (g)^{60}Fe (h)^{59}Co

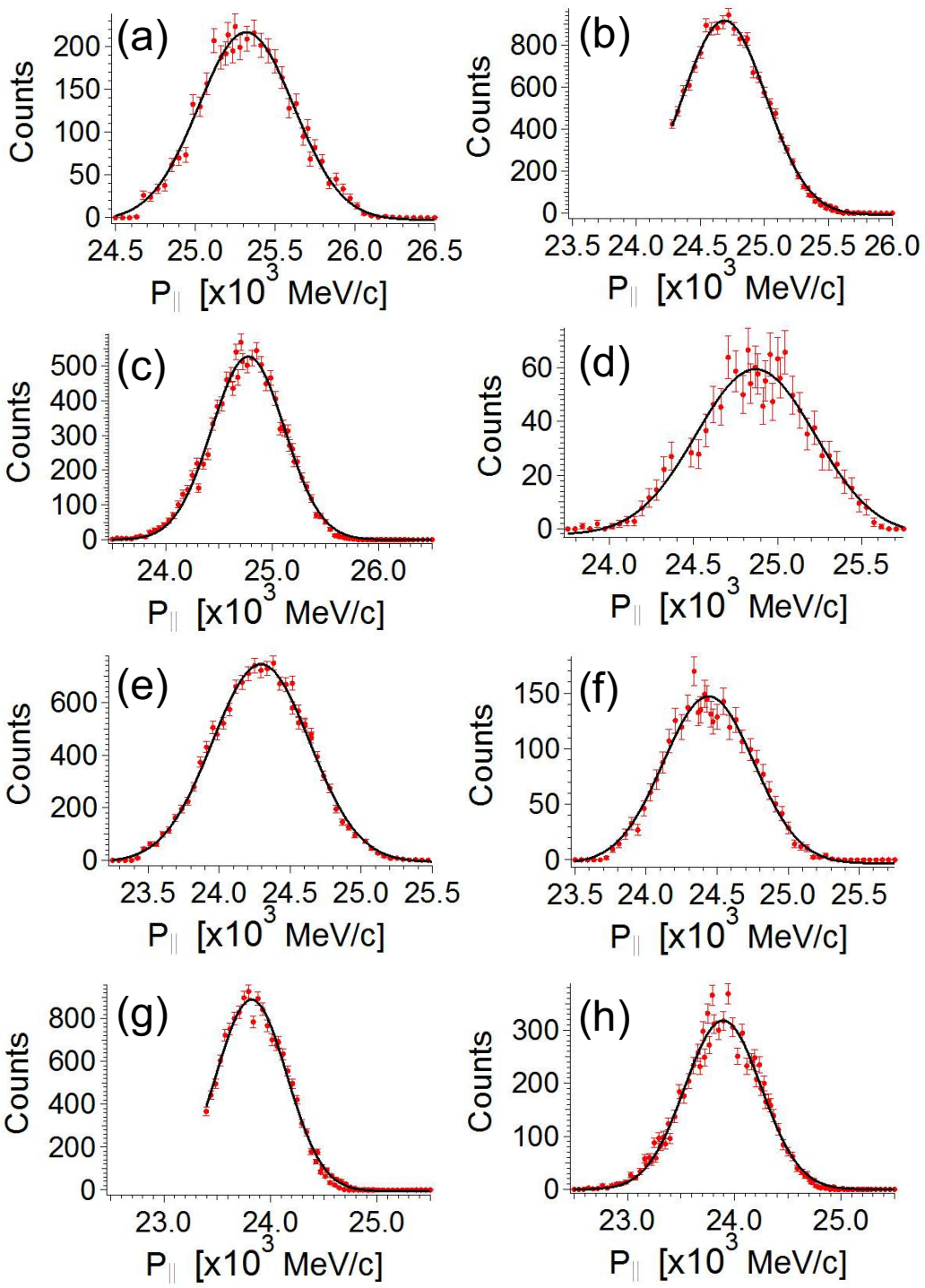

Figure A.6: Parallel momentum distributions for fragments produced from ^{76}Ge on a Be target. (a)^{59}Fe (b)^{58}Co (c)^{58}Fe (d)^{58}Mn (e)^{57}Fe (f)^{57}Mn (g)^{56}Fe (h)^{56}Mn

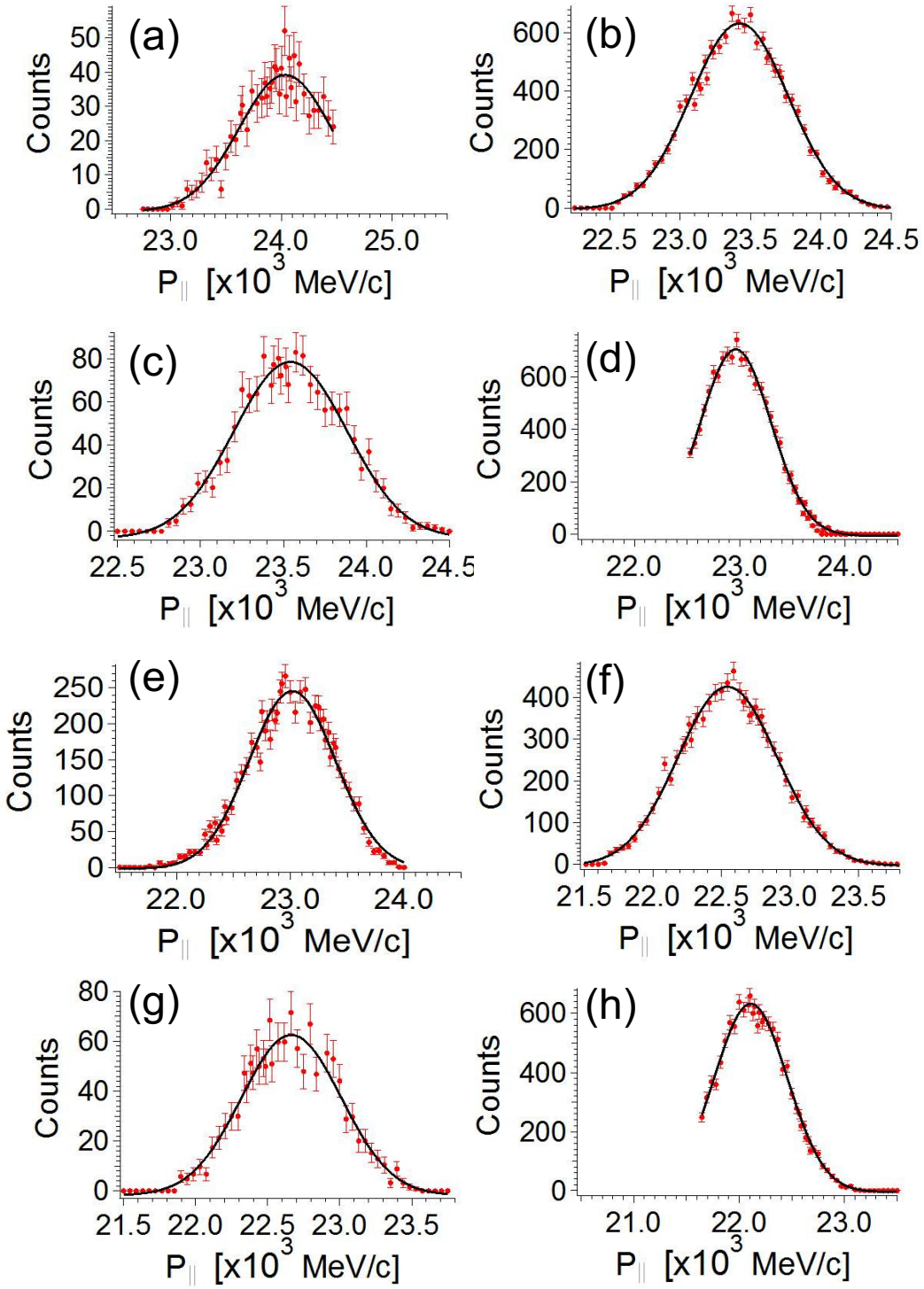

Figure A.7: Parallel momentum distributions for fragments produced from ^{76}Ge on a Be target. (a)^{56}Cr (b)^{55}Mn (c)^{55}Cr (d)^{54}Mn (e)^{54}Cr (f)^{53}Cr (g)^{53}V (h)^{52}Cr

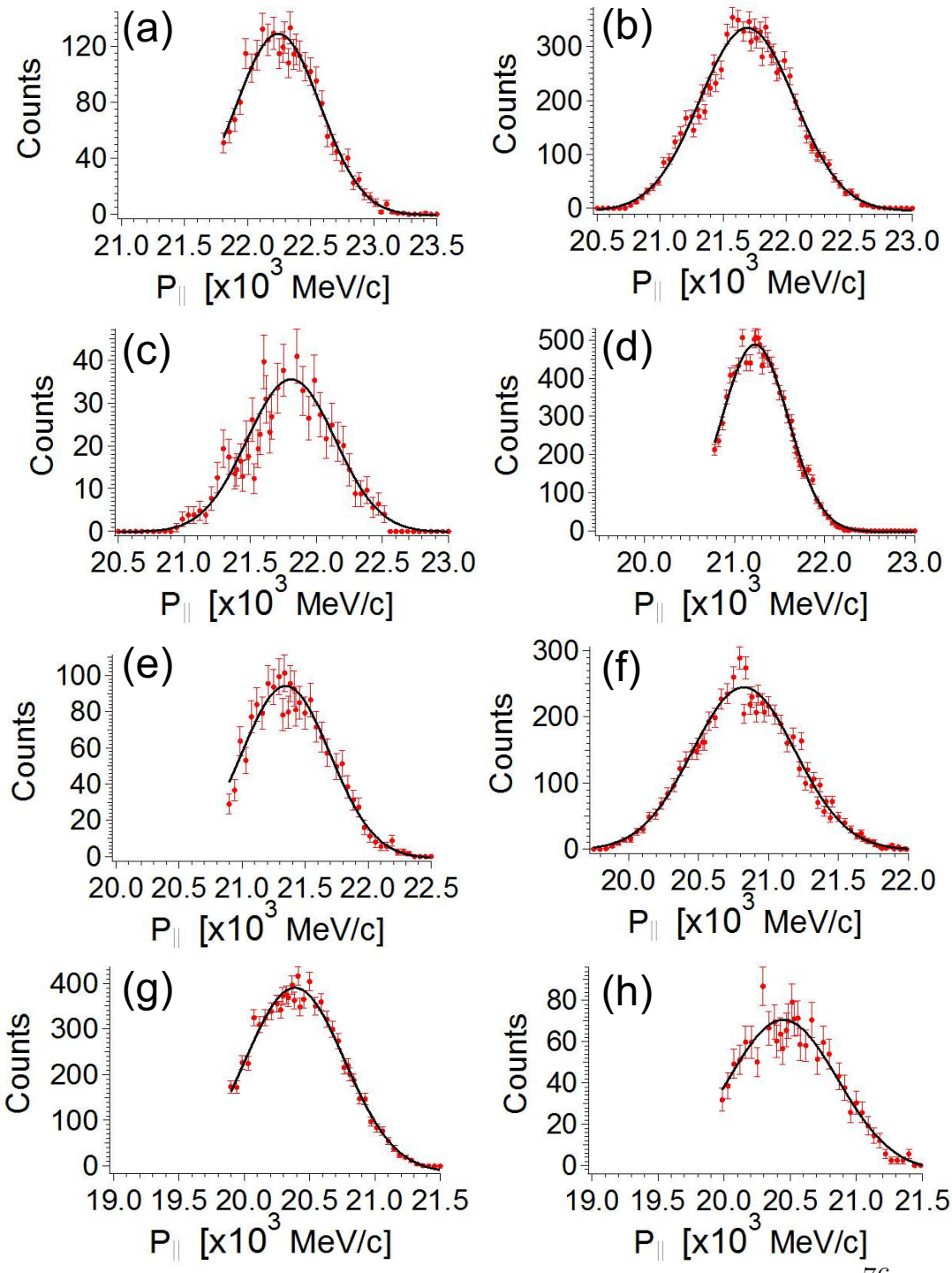

Figure A.8: Parallel momentum distributions for fragments produced from ^{76}Ge on a Be target. (a)^{52}V (b)^{51}V (c)^{51}Ti (d)^{50}V (e)^{50}Ti (f)^{49}Ti (g)^{48}Ti (h)^{48}Sc

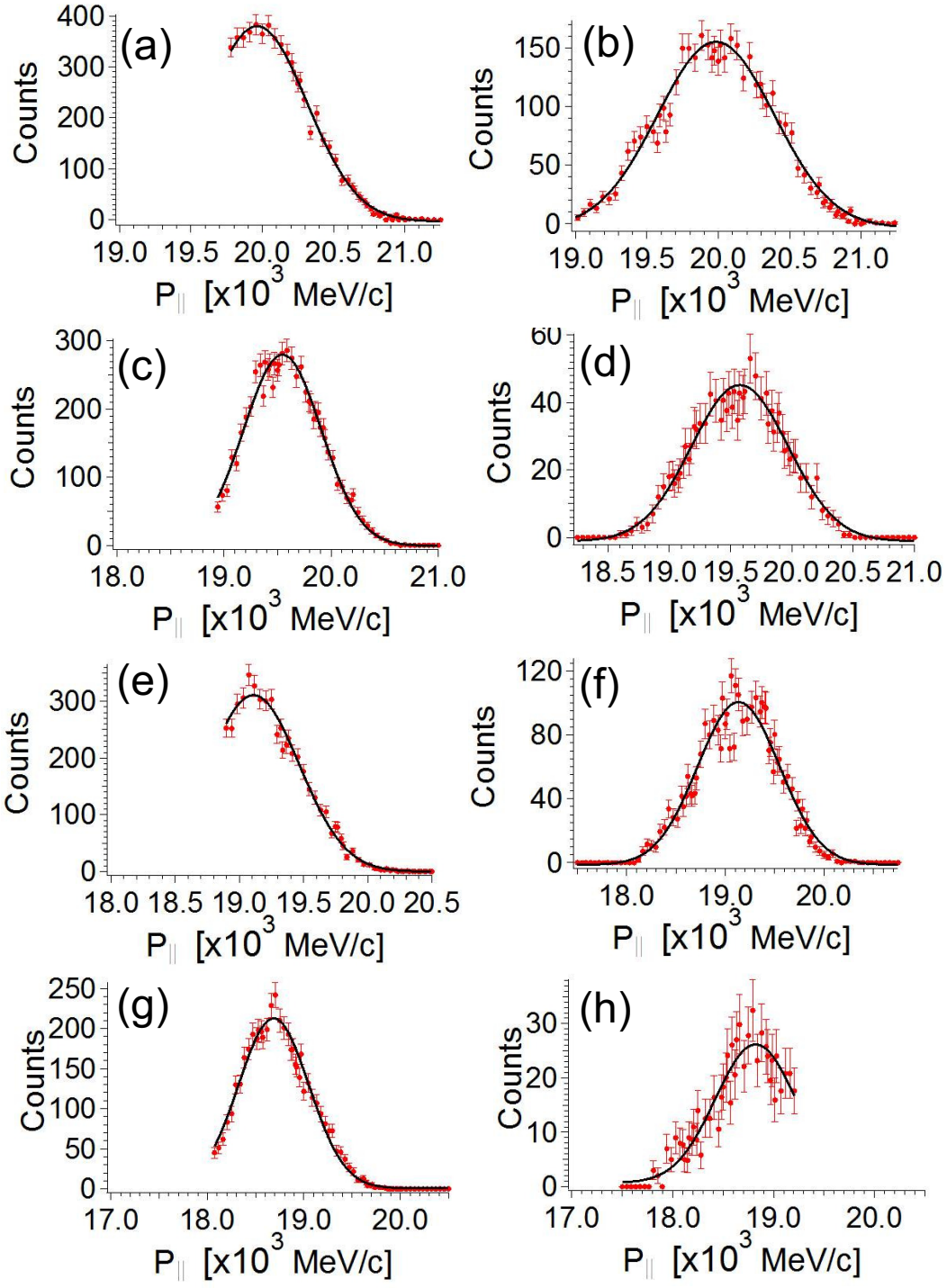

Figure A.9: Parallel momentum distributions for fragments produced from ^{76}Ge on a Be target. (a)^{47}Ti (b)^{47}Sc (c)^{46}Sc (d)^{46}Ca (e)^{45}Sc (f)^{45}Ca (g)^{44}Ca (h)^{44}K

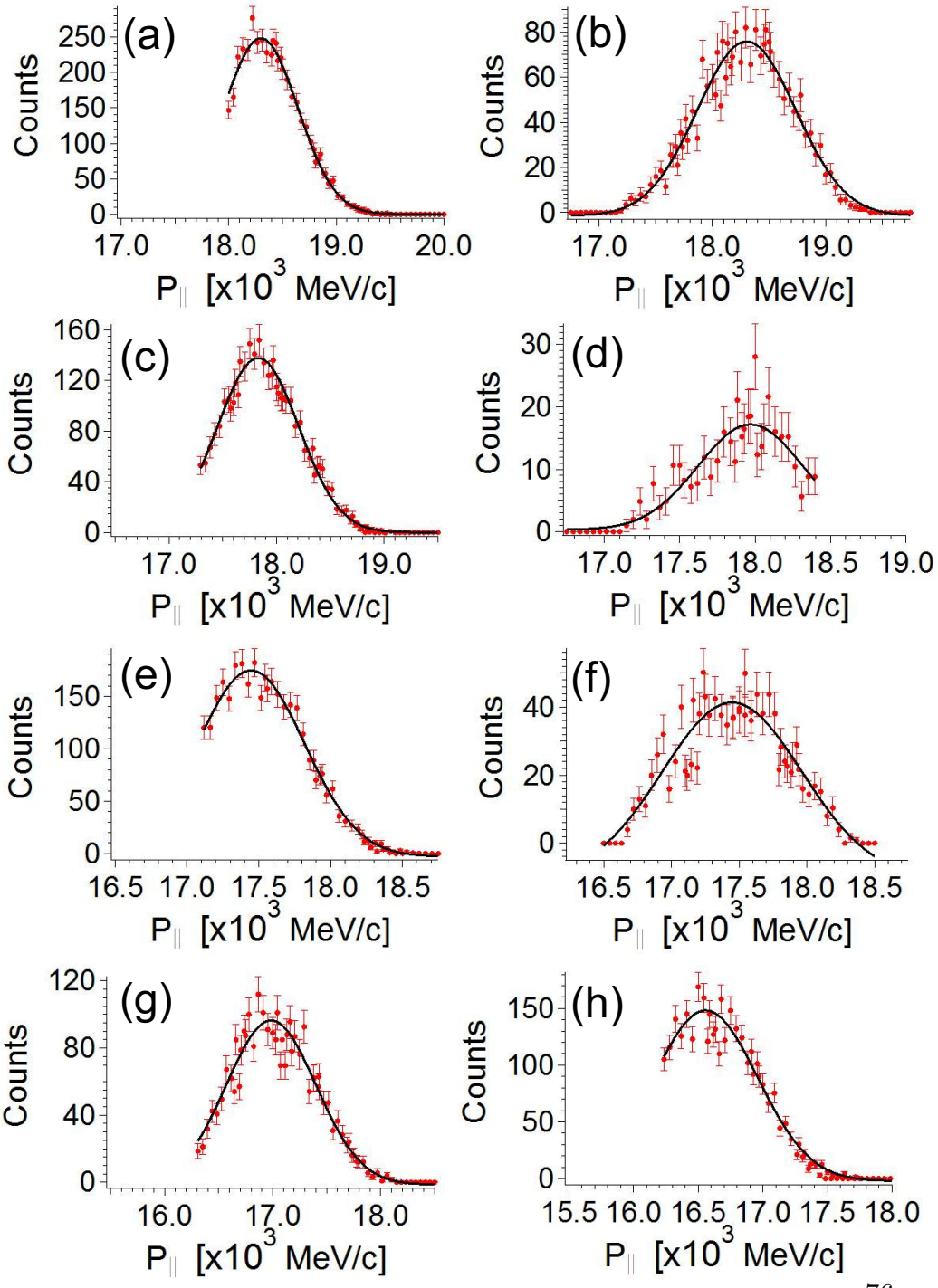

Figure A.10: Parallel momentum distributions for fragments produced from ^{76}Ge on a Be target. (a)^{43}Ca (b)^{43}K (c)^{42}K (d)^{42}Ar (e)^{41}K (f)^{41}Ar (g)^{40}Ar (h)^{39}Ar

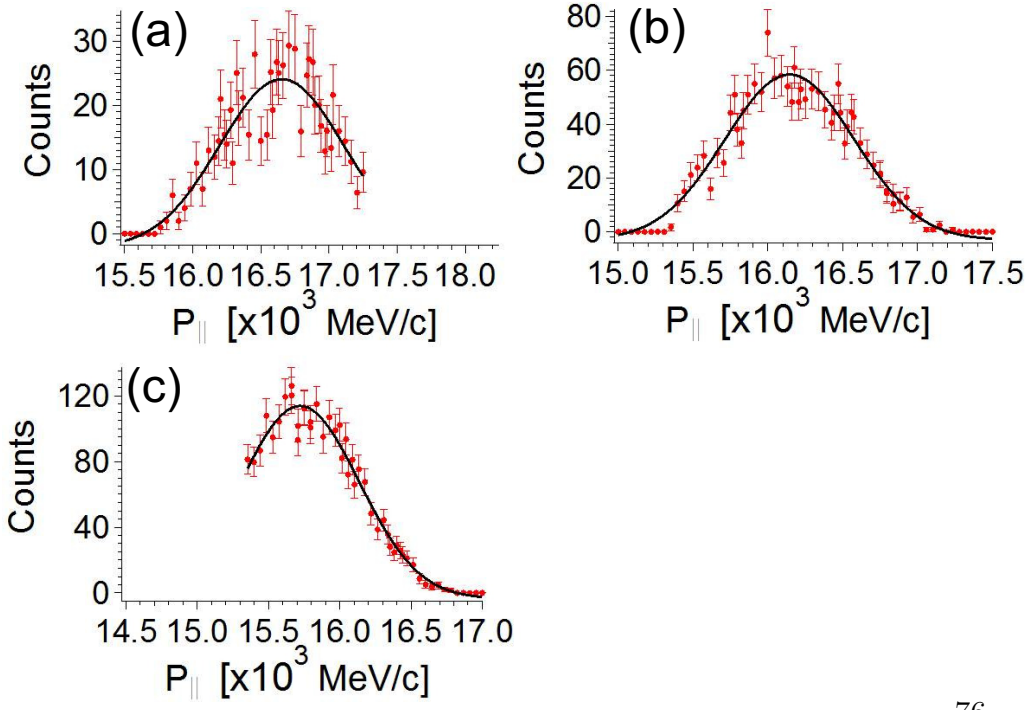

Figure A.11: Parallel momentum distributions for fragments produced from ^{76}Ge on a Be target. (a)^{39}Cl (b)^{38}Cl (c)^{37}Cl

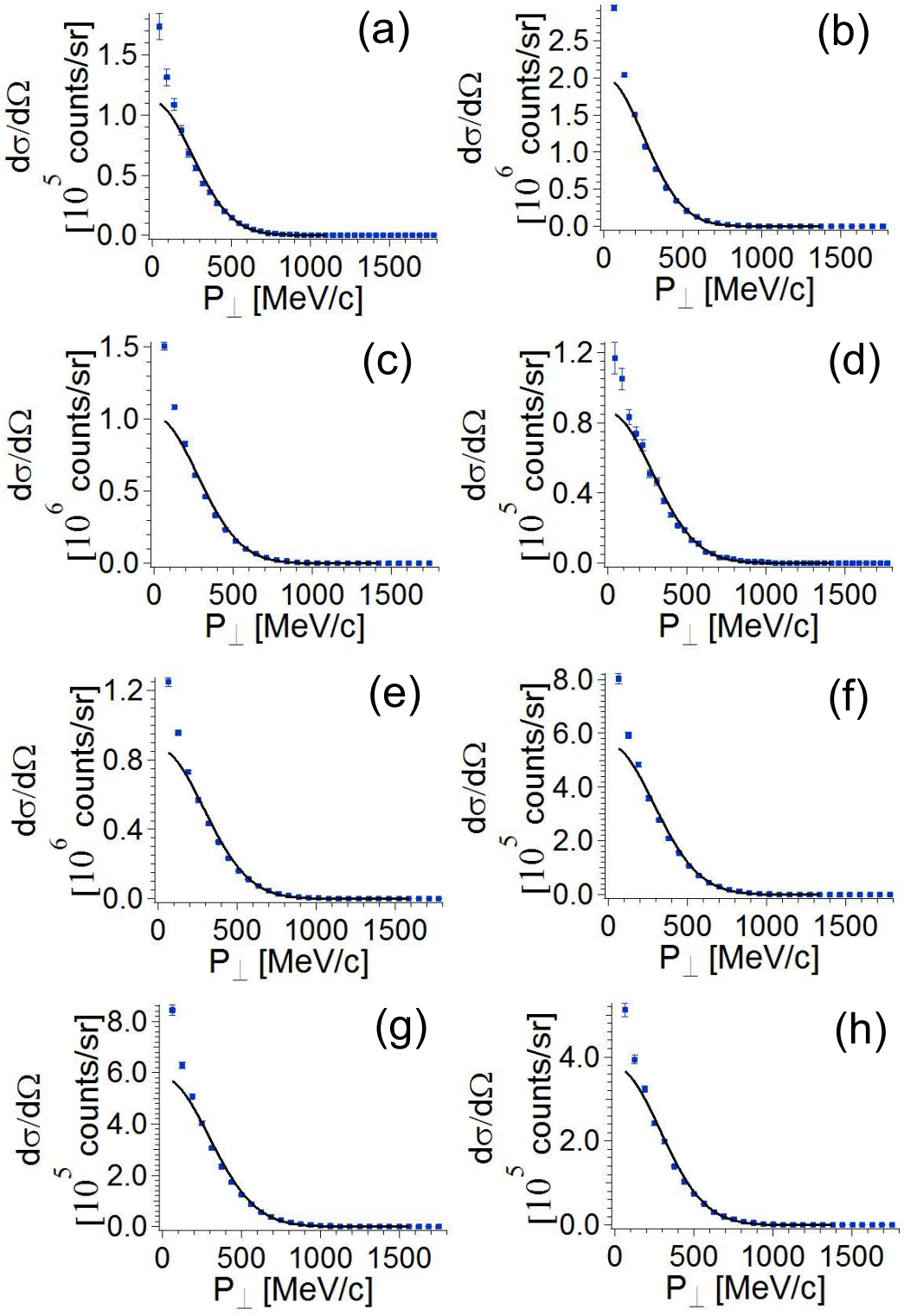

Figure A.12: Perpendicular momentum distributions for fragments produced from ^{76}Ge on a Be target. (a)^{74}As (b)^{74}Ge (c)^{73}Ge (d)^{72}As (e)^{72}Ge (f)^{72}Ga (g)^{71}Ge (h)^{71}Ga

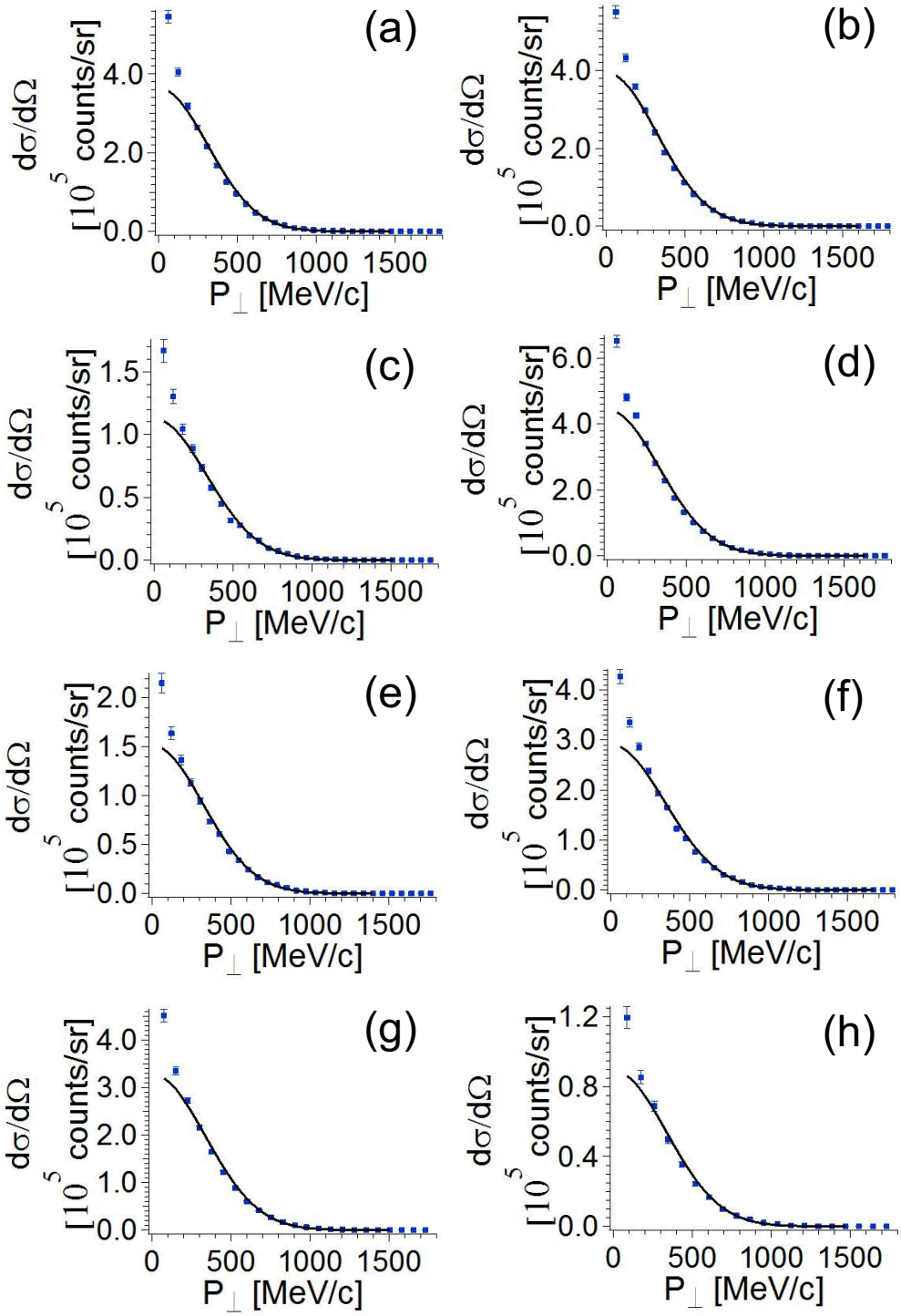

Figure A.13: Perpendicular momentum distributions for fragments produced from ^{76}Ge on a Be target. (a)^{70}Ge (b)^{70}Ga (c)^{69}Ge (d)^{69}Ga (e)^{69}Ge (f)^{68}Ga (g)^{68}Zn (h)^{68}Cu

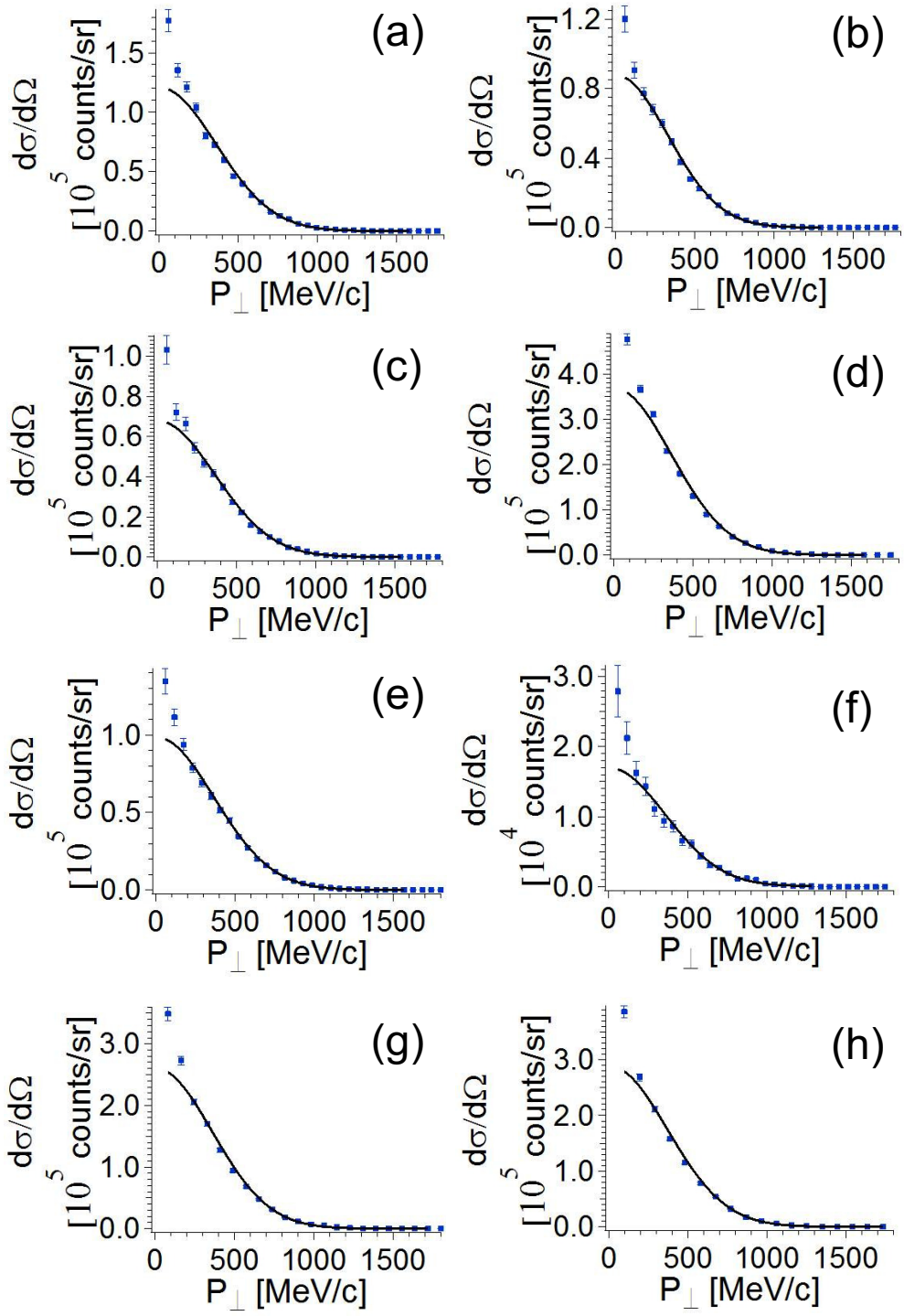

Figure A.14: Perpendicular momentum distributions for fragments produced from ^{76}Ge on a Be target. (a)^{67}Ga (b)^{67}Zn (c)^{67}Cu (d)^{66}Zn (e)^{66}Cu (f)^{66}Ni (g)^{65}Zn (h)^{65}Cu

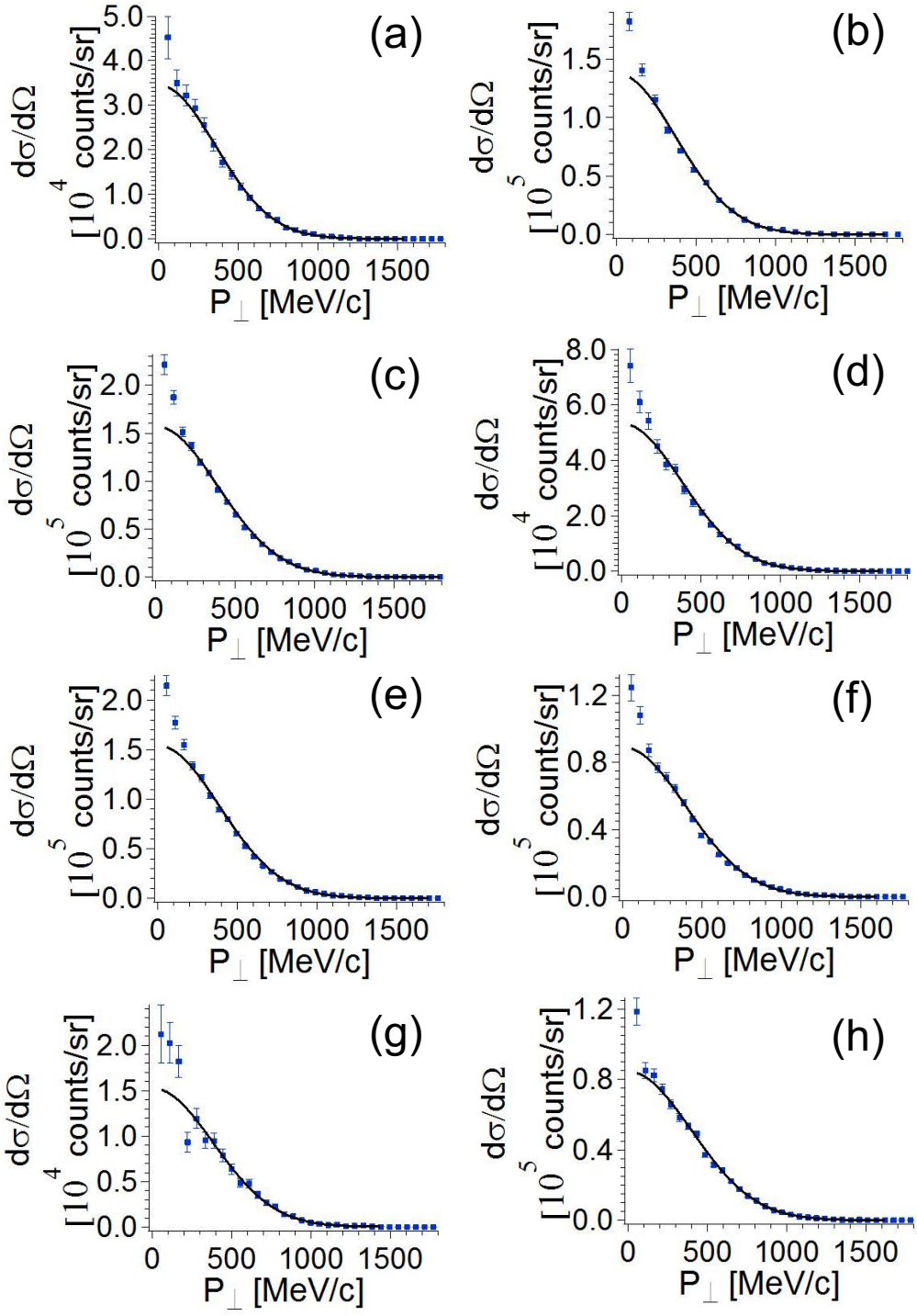

Figure A.15: Perpendicular momentum distributions for fragments produced from ^{76}Ge on a Be target. (a)^{65}Ni (b)^{64}Zn (c)^{64}Cu (d)^{64}Ni (e)^{63}Cu (f)^{63}Ni (g)^{63}Co (h)^{62}Cu

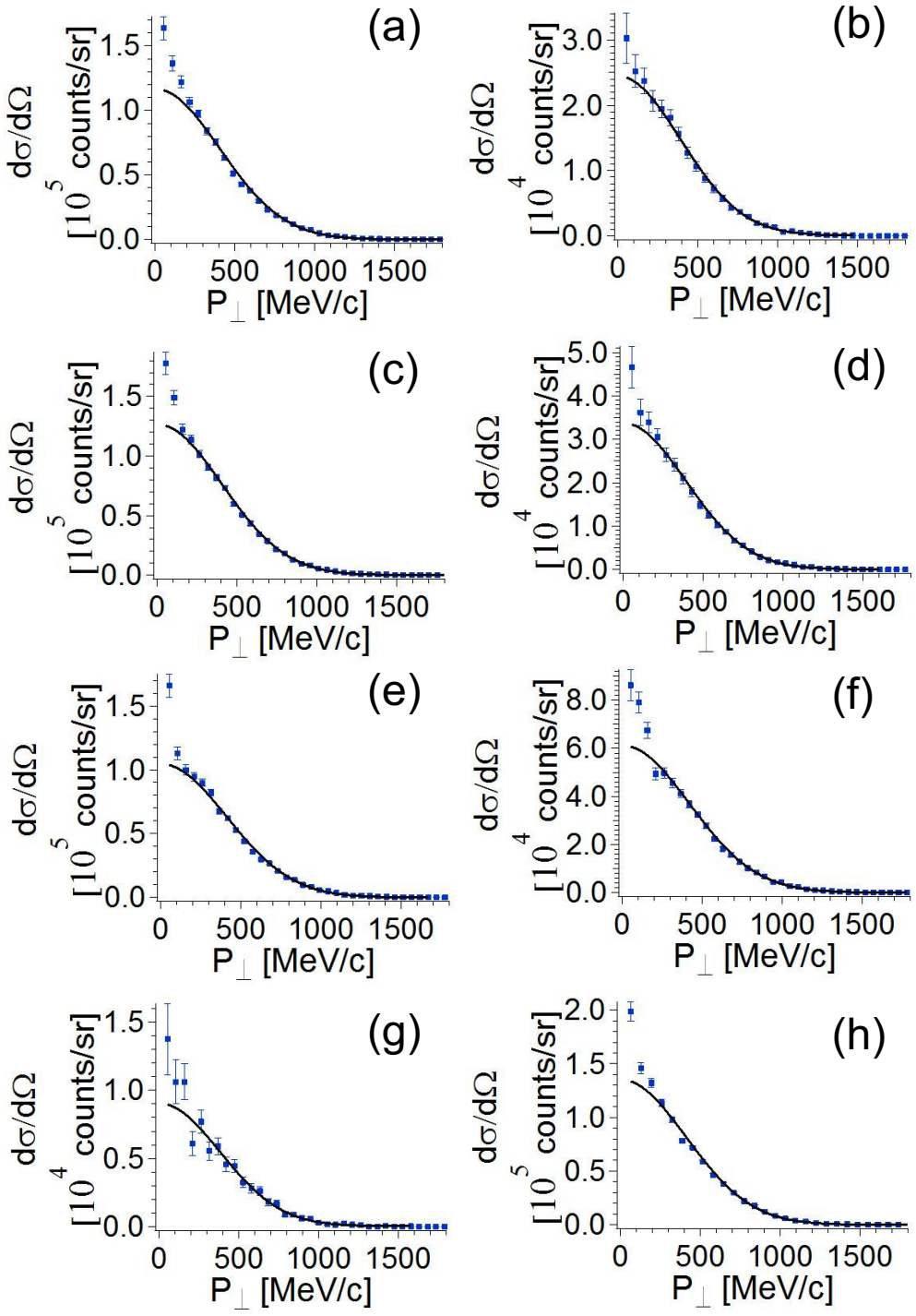

Figure A.16: Perpendicular momentum distributions for fragments produced from ^{76}Ge on a Be target. (a)^{62}Ni (b)^{62}Co (c)^{61}Ni (d)^{61}Co (e)^{60}Ni (f)^{60}Co (g)^{60}Fe (h)^{59}Co

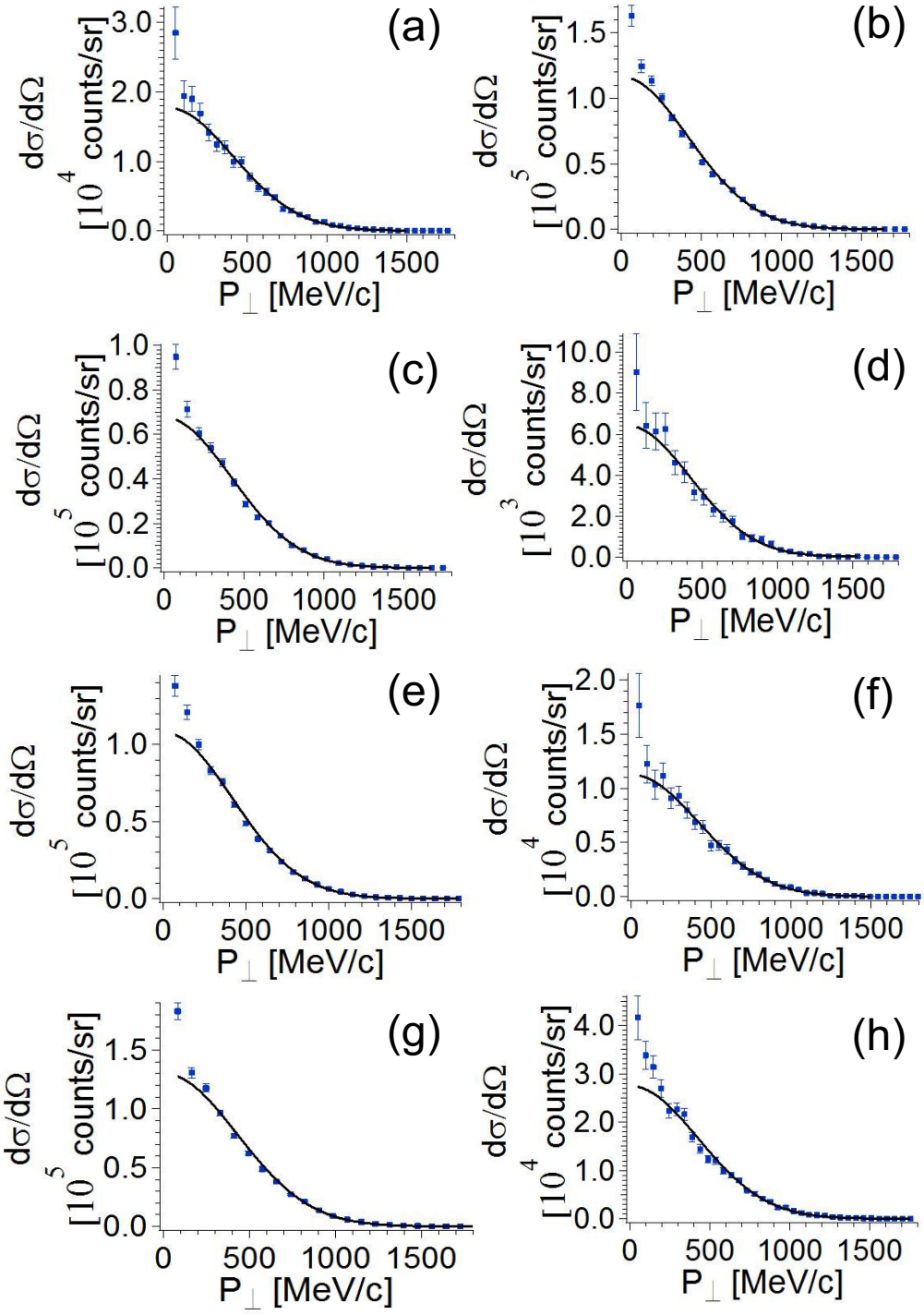

Figure A.17: Perpendicular momentum distributions for fragments produced from ^{76}Ge on a Be target. (a)^{59}Fe (b)^{58}Co (c)^{58}Fe (d)^{58}Mn (e)^{57}Fe (f)^{57}Mn (g)^{56}Fe (h)^{56}Mn

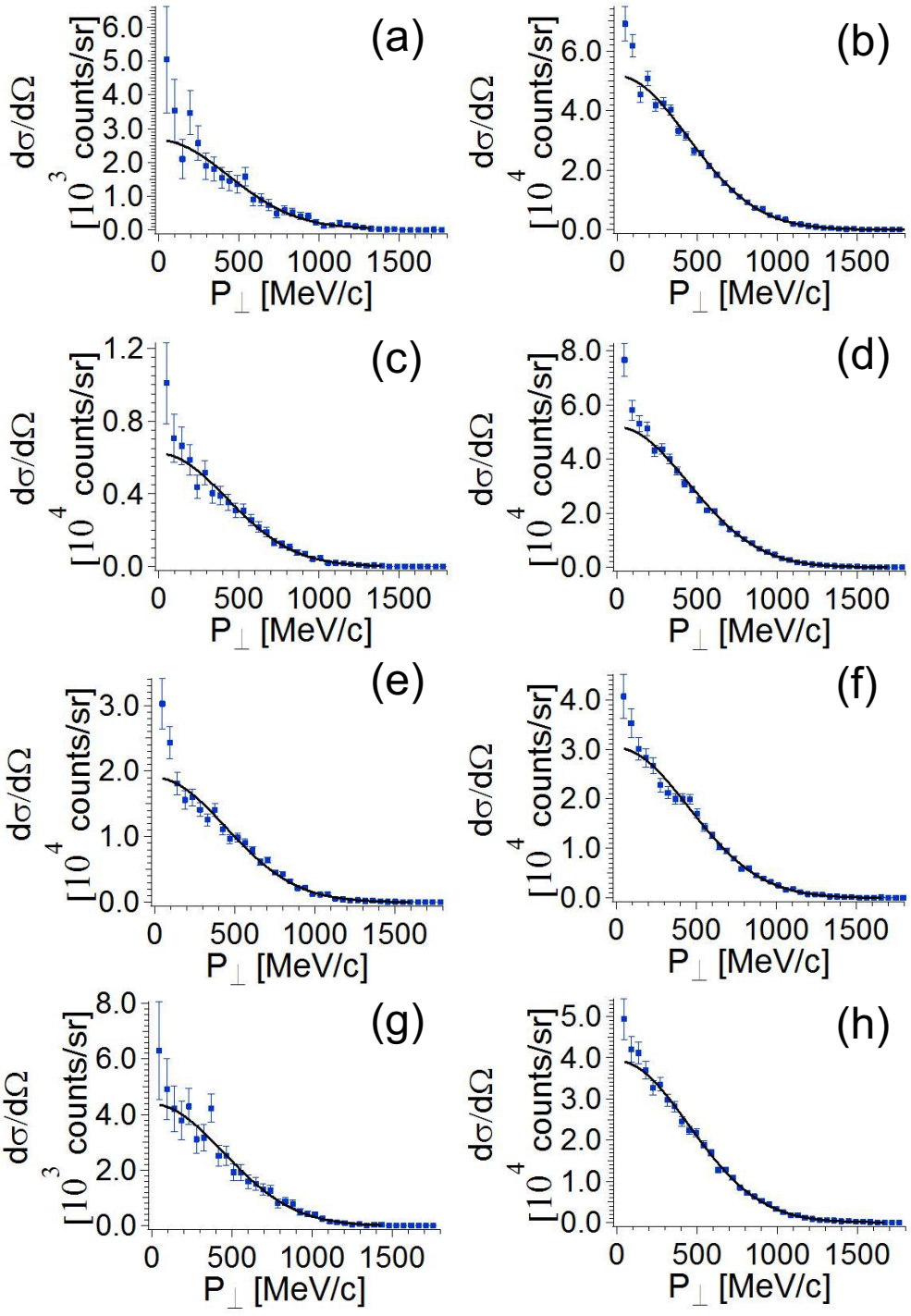

Figure A.18: Perpendicular momentum distributions for fragments produced from ^{76}Ge on a Be target. (a)^{56}Cr (b)^{55}Mn (c)^{55}Cr (d)^{54}Mn (e)^{54}Cr (f)^{53}Cr (g)^{53}V (h)^{52}Cr

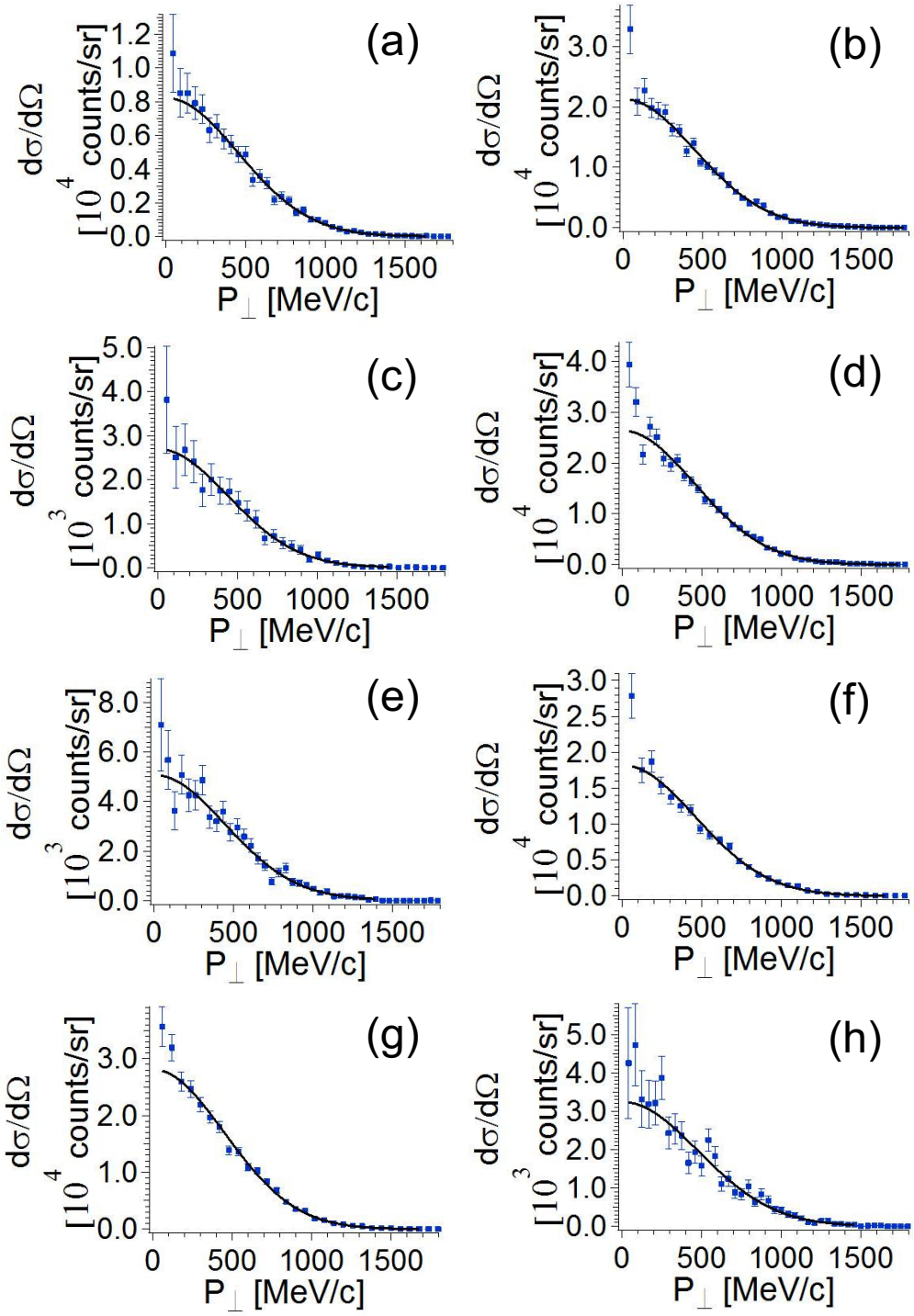

Figure A.19: Perpendicular momentum distributions for fragments produced from ^{76}Ge on a Be target. (a)^{52}V (b)^{51}V (c)^{51}Ti (d)^{50}V (e)^{50}Ti (f)^{49}Ti (g)^{48}Ti (h)^{48}Sc

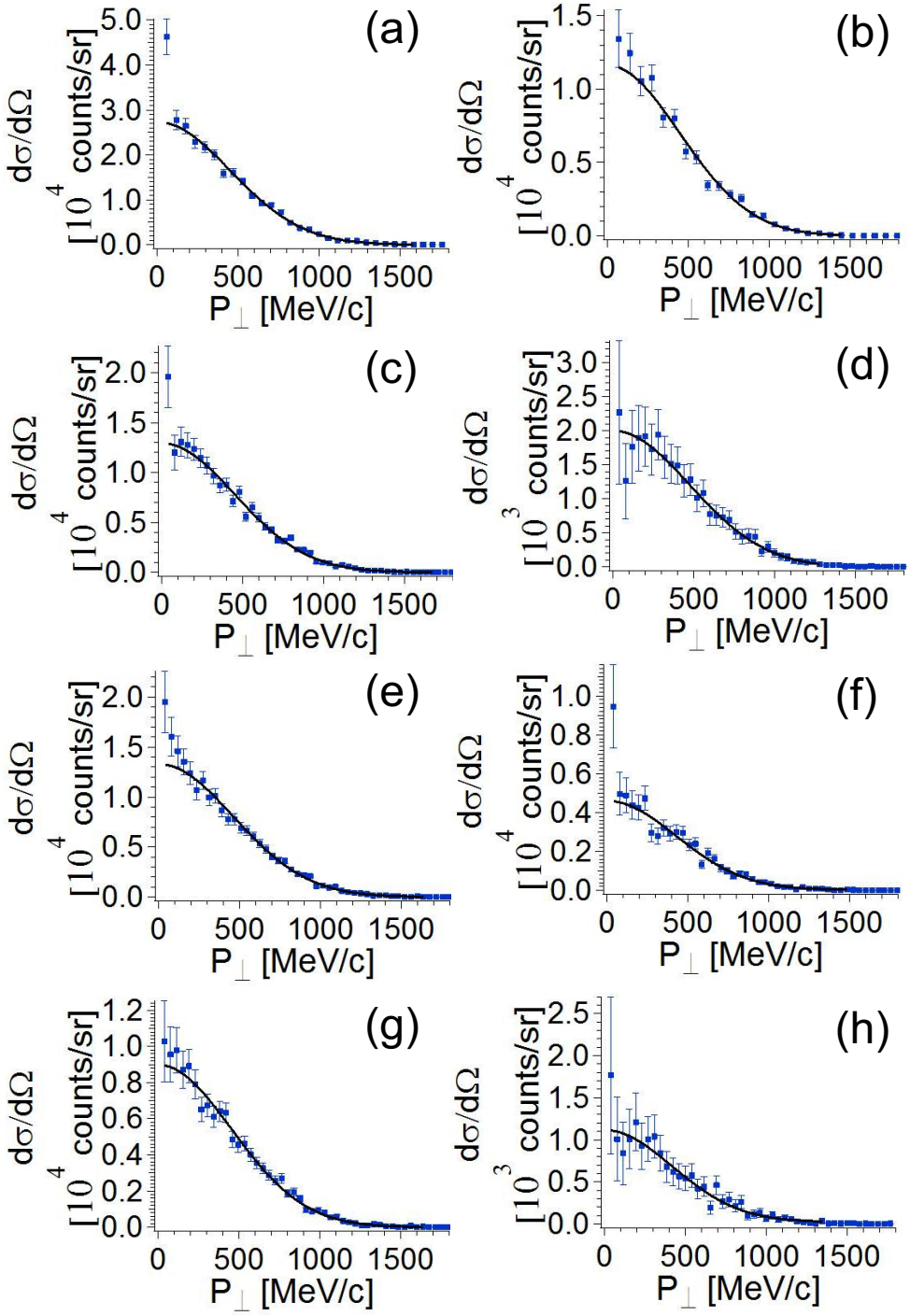

Figure A.20: Perpendicular momentum distributions for fragments produced from ^{76}Ge on a Be target. (a)^{47}Ti (b)^{47}Sc (c)^{46}Sc (d)^{46}Ca (e)^{45}Sc (f)^{45}Ca (g)^{44}Ca (h)^{44}K

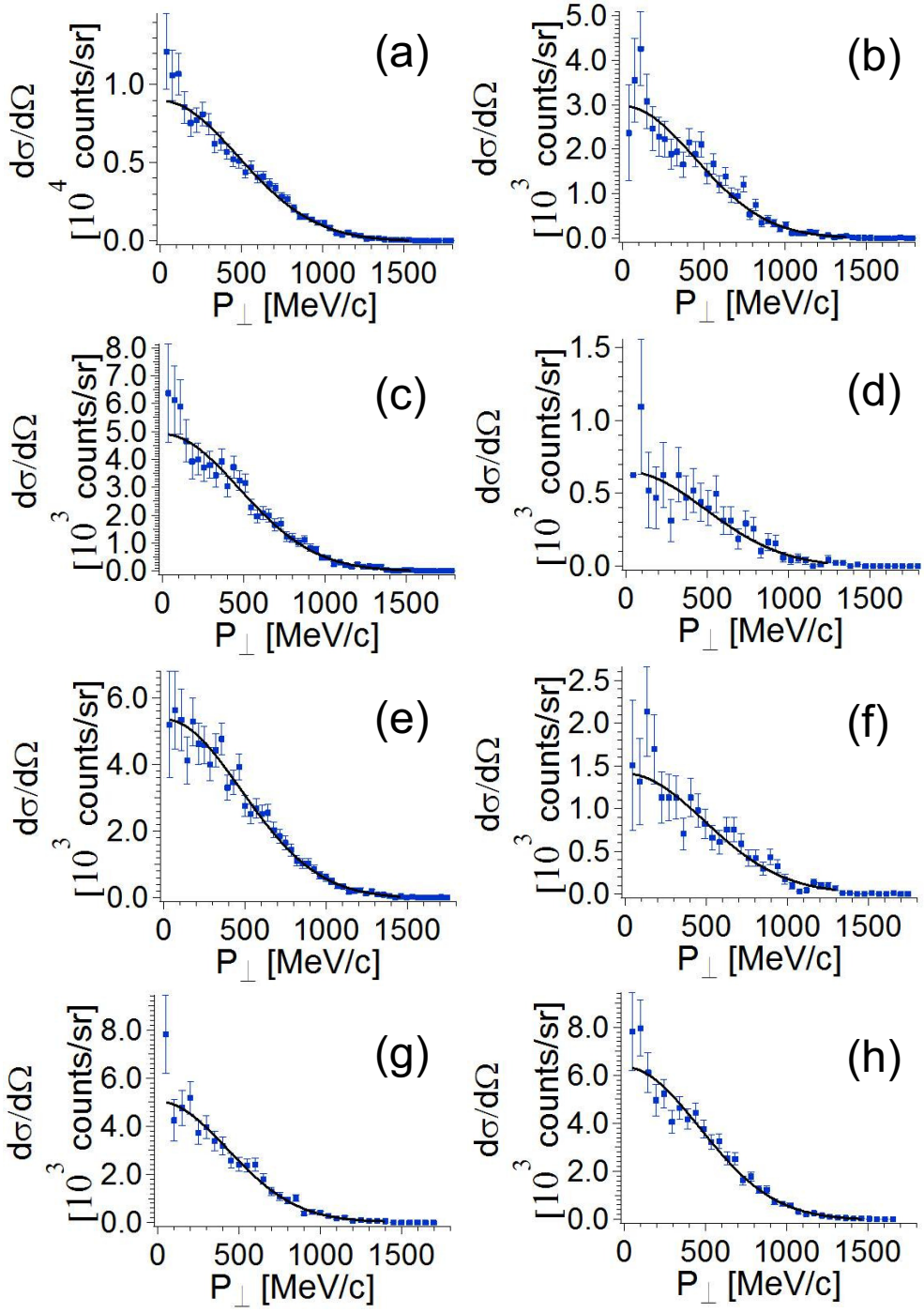

Figure A.21: Perpendicular momentum distributions for fragments produced from ^{76}Ge on a Be target. (a)^{43}Ca (b)^{43}K (c)^{42}K (d)^{42}Ar (e)^{41}K (f)^{41}Ar (g)^{40}Ar (h)^{39}Ar

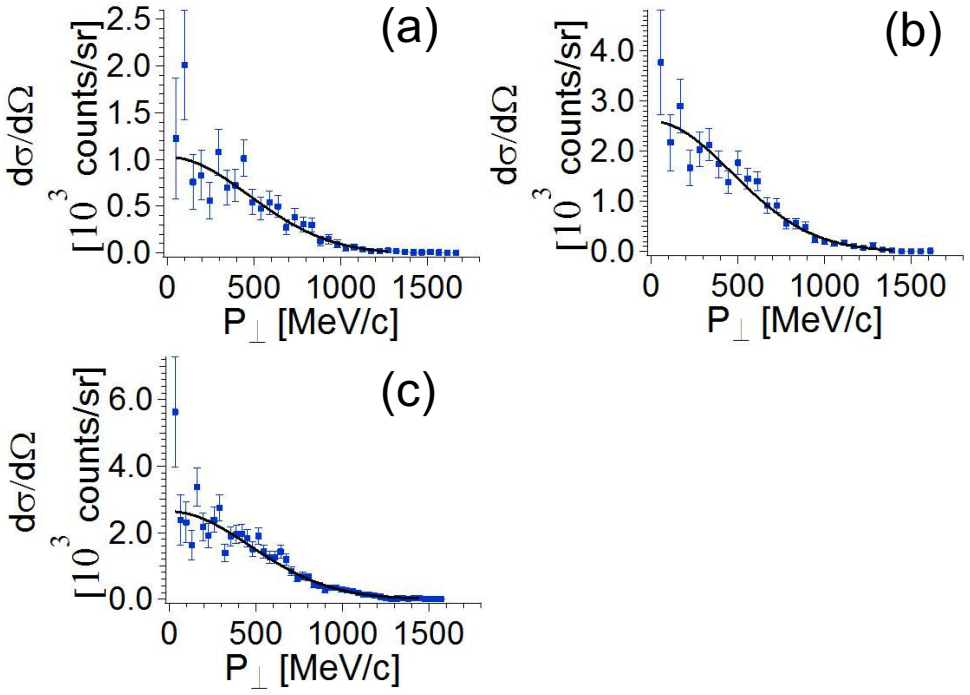

Figure A.22: Perpendicular momentum distributions for fragments produced from ^{76}Ge on a Be target. (a)^{39}Cl (b)^{38}Cl (c)^{37}Cl

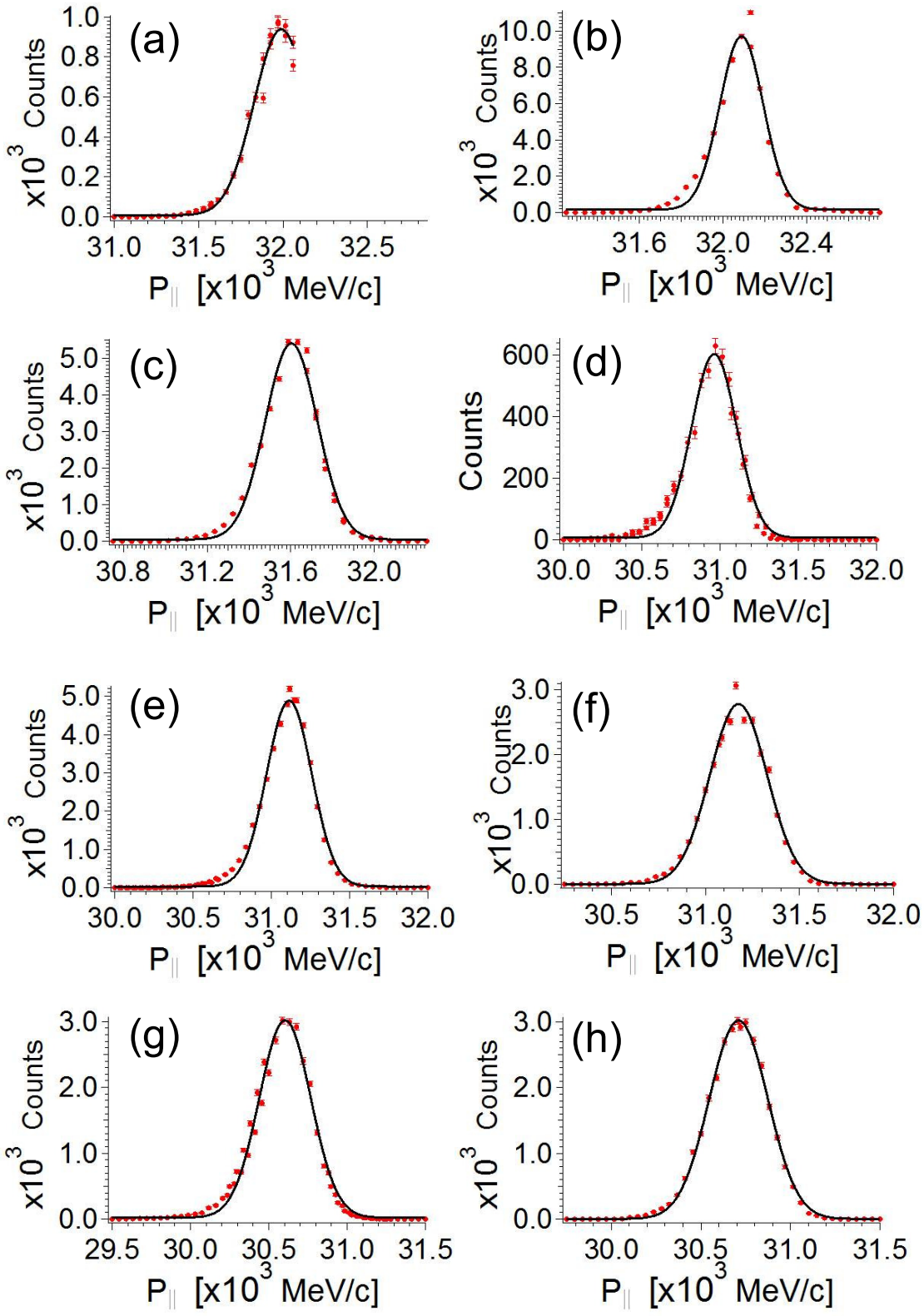

Figure A.23: Parallel momentum distributions for fragments produced from ^{76}Ge on a Au target. (a)^{74}As (b)^{73}As (c)^{73}Ge (d)^{72}As (e)^{72}Ge (f)^{71}Ge (g)^{71}Ga (h)^{70}Ge

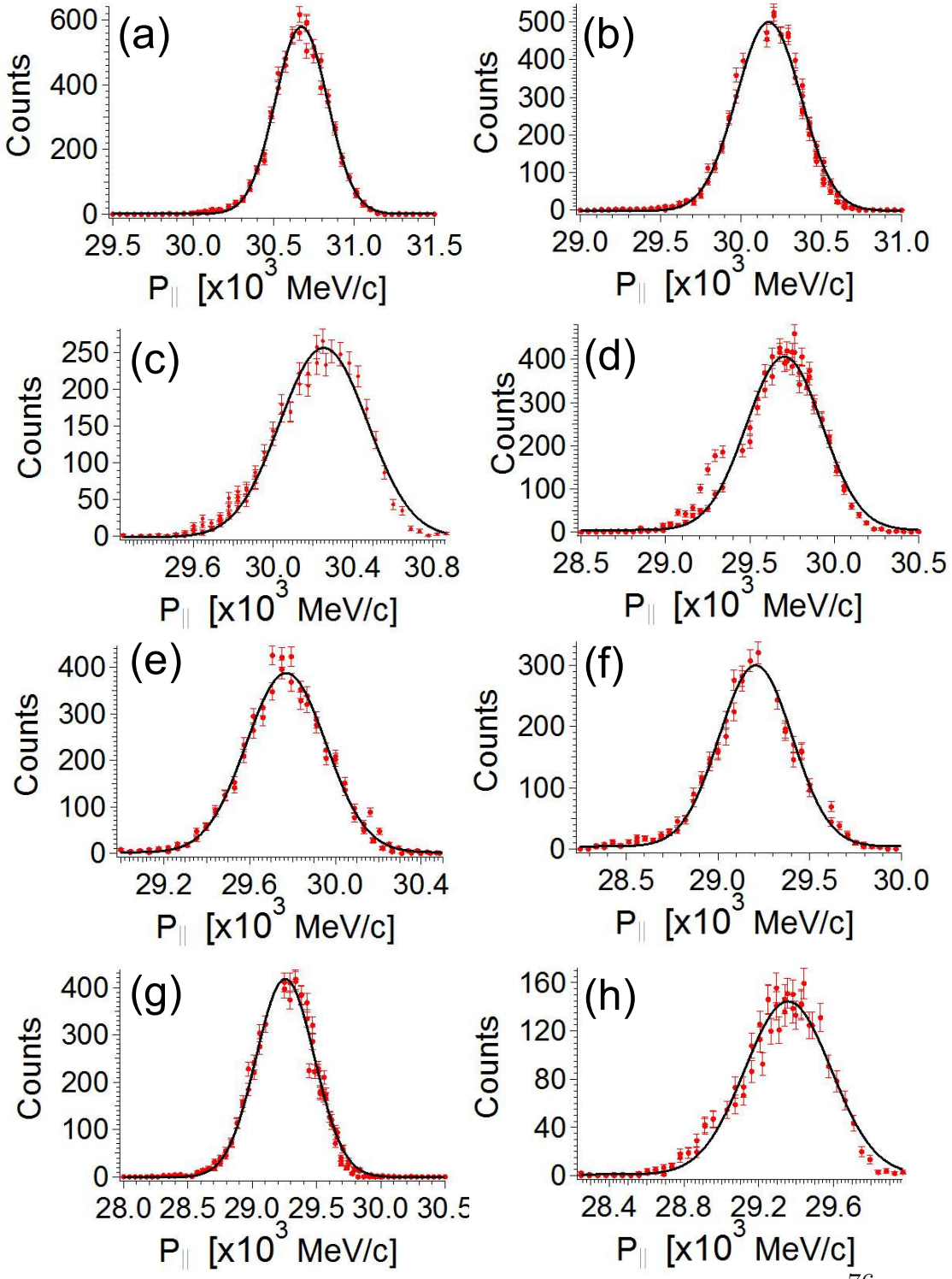

Figure A.24: Parallel momentum distributions for fragments produced from ^{76}Ge on a Au target. (a)^{70}Ga (b)^{69}Ga (c)^{69}Zn (d)^{68}Ga (e)^{68}Zn (f)^{67}Ga (g)^{67}Zn (h)^{67}Cu

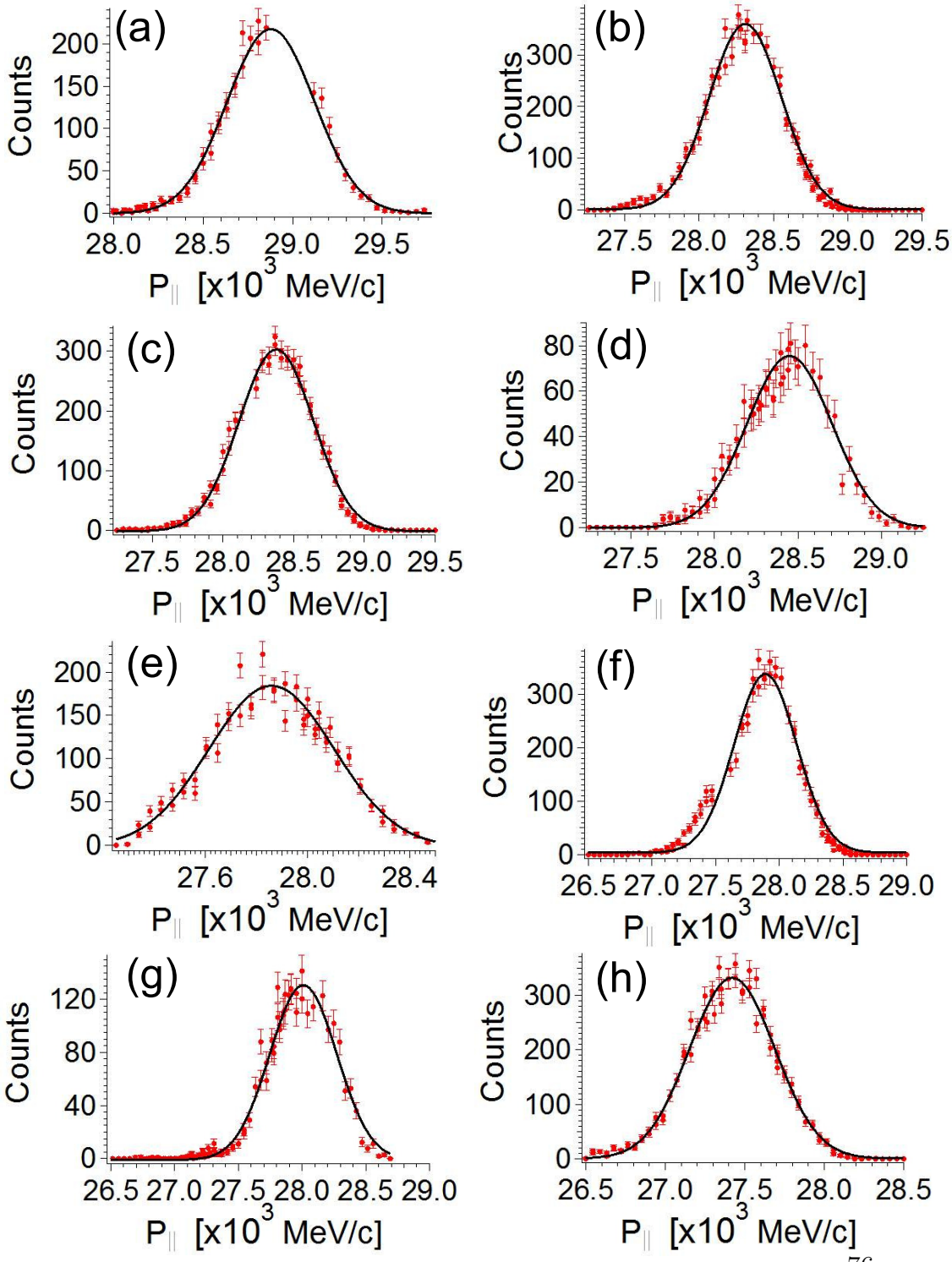

Figure A.25: Parallel momentum distributions for fragments produced from ^{76}Ge on a Au target. (a)^{66}Cu (b)^{65}Zn (c)^{65}Cu (d)^{65}Ni (e)^{64}Zn (f)^{64}Cu (g)^{64}Ni (h)^{63}Cu

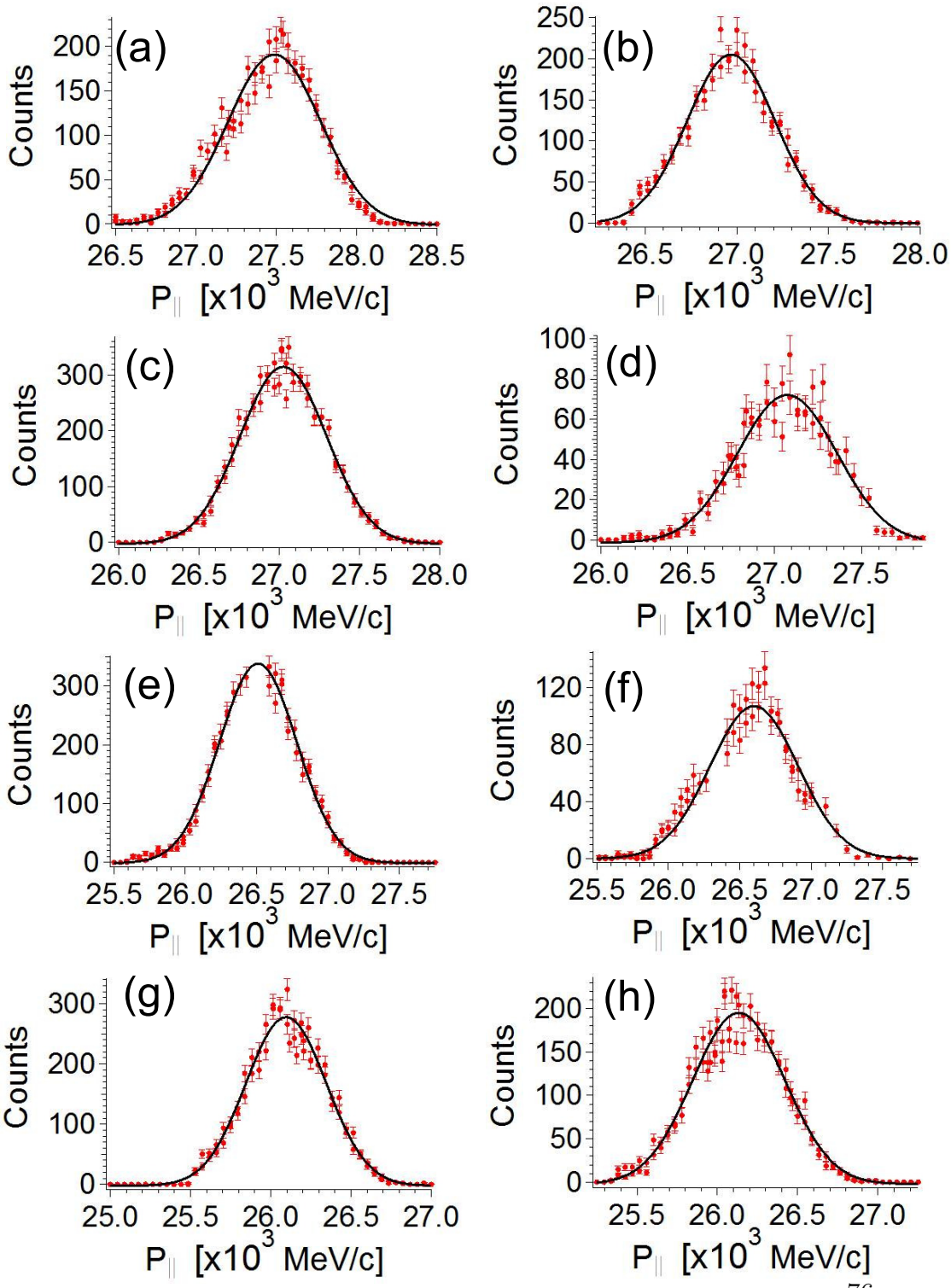

Figure A.26: Parallel momentum distributions for fragments produced from ^{76}Ge on a Au target. (a)^{63}Ni (b)^{62}Cu (c)^{62}Ni (d)^{62}Co (e)^{61}Ni (f)^{64}Cu (g)^{61}Co (h)^{60}Ni

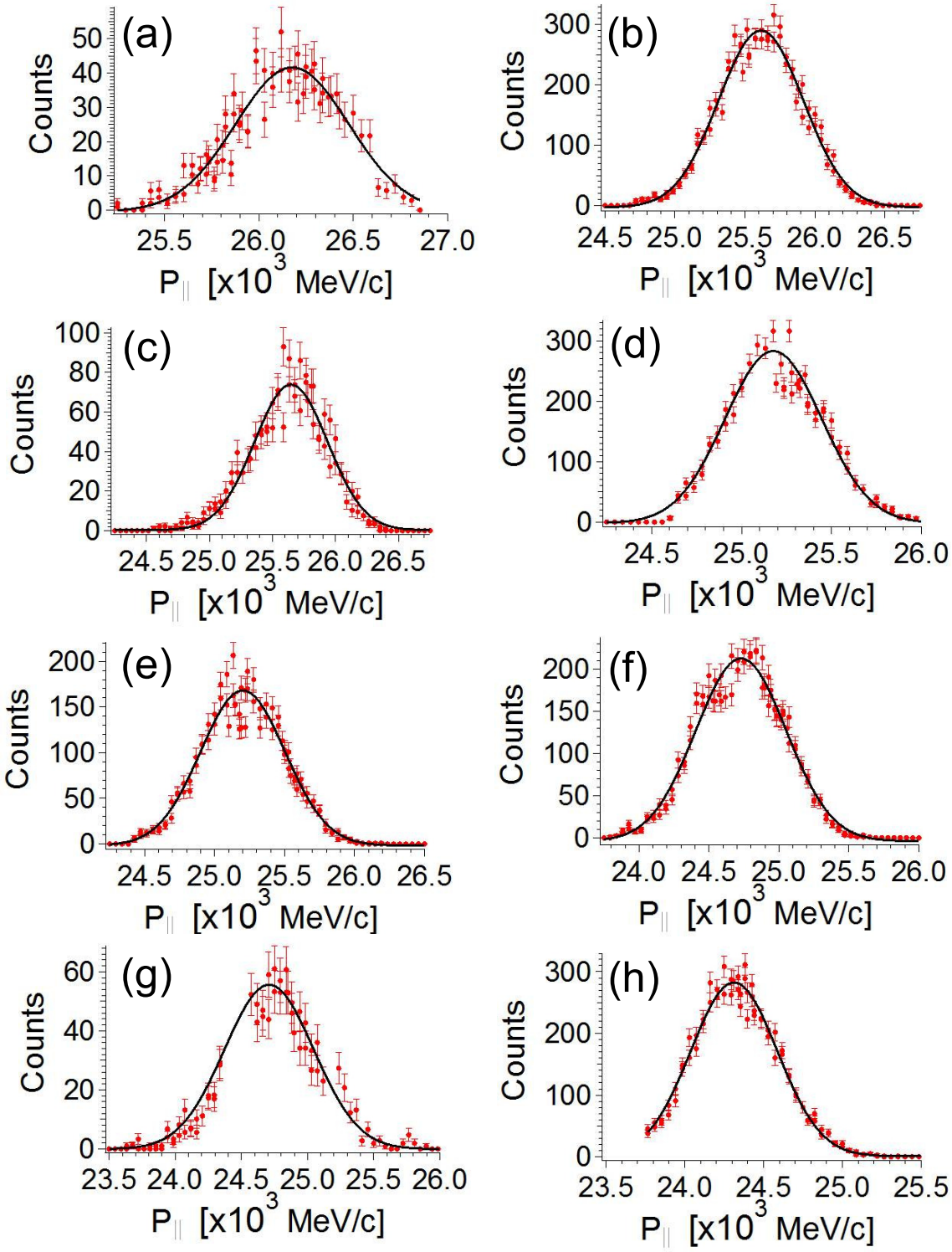

Figure A.27: Parallel momentum distributions for fragments produced from ^{76}Ge on a Au target. (a)^{60}Fe (b)^{59}Co (c)^{59}Fe (d)^{58}Co (e)^{58}Fe (f)^{57}Fe (g)^{57}Mn (h)^{56}Fe

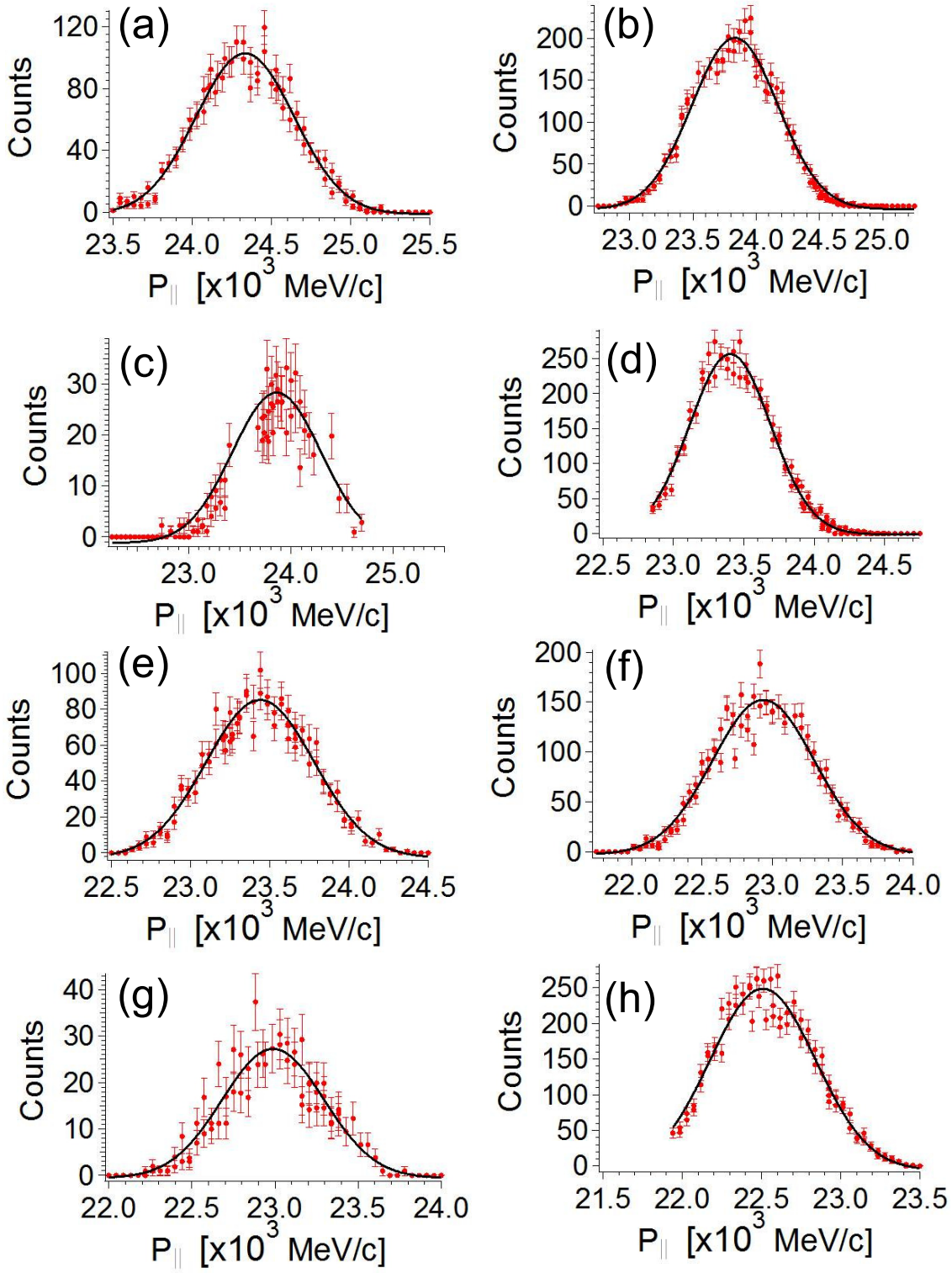

Figure A.28: Parallel momentum distributions for fragments produced from ^{76}Ge on a Au target. (a)^{56}Mn (b)^{55}Mn (c)^{55}Cr (d)^{54}Mn (e)^{54}Cr (f)^{53}Cr (g)^{53}V (h)^{52}Cr

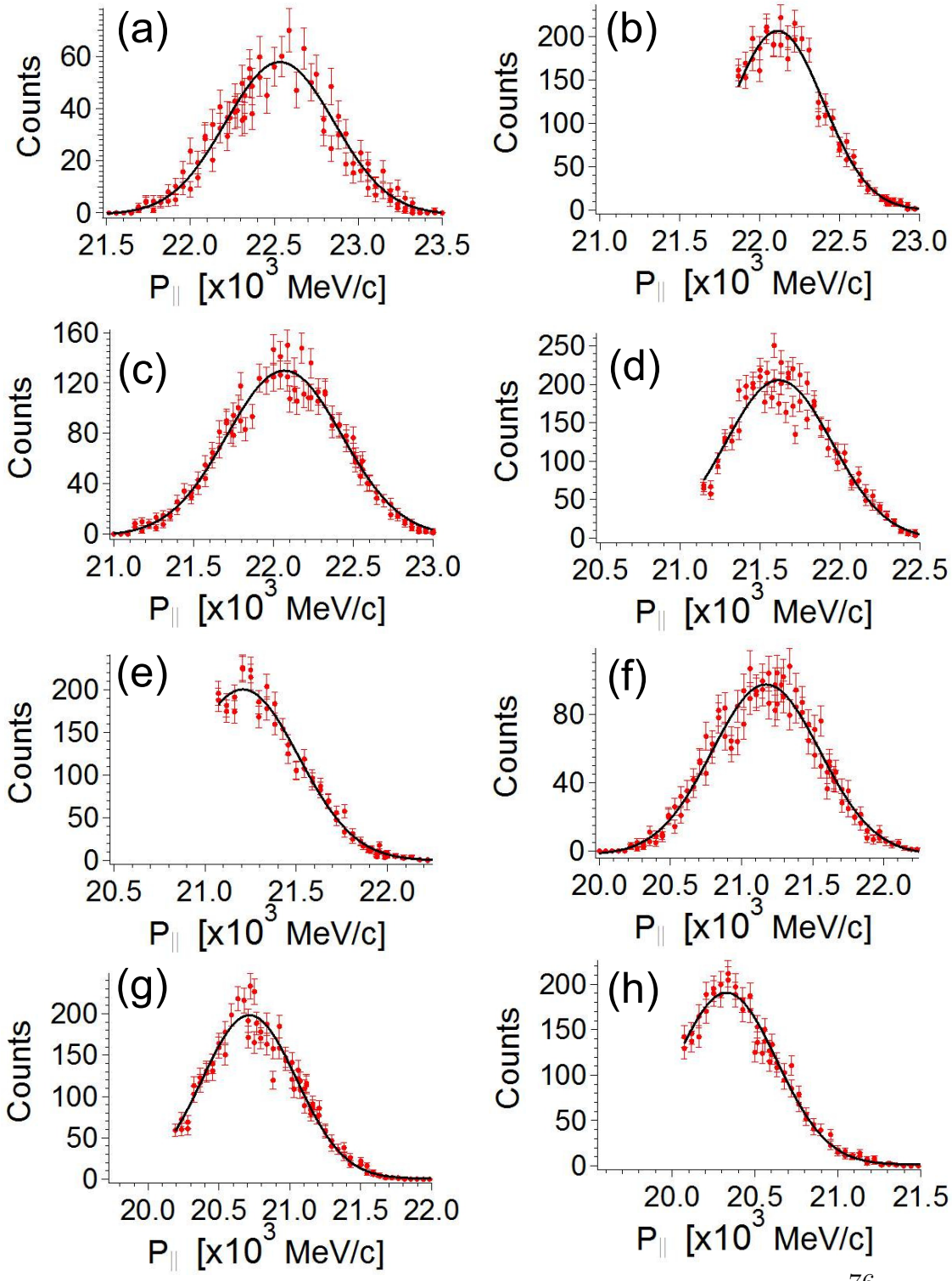

Figure A.29: Parallel momentum distributions for fragments produced from ^{76}Ge on a Au target. (a)^{52}V (b)^{51}Cr (c)^{51}V (d)^{50}V (e)^{49}V (f)^{49}Ti (g)^{48}Ti (h)^{47}Ti

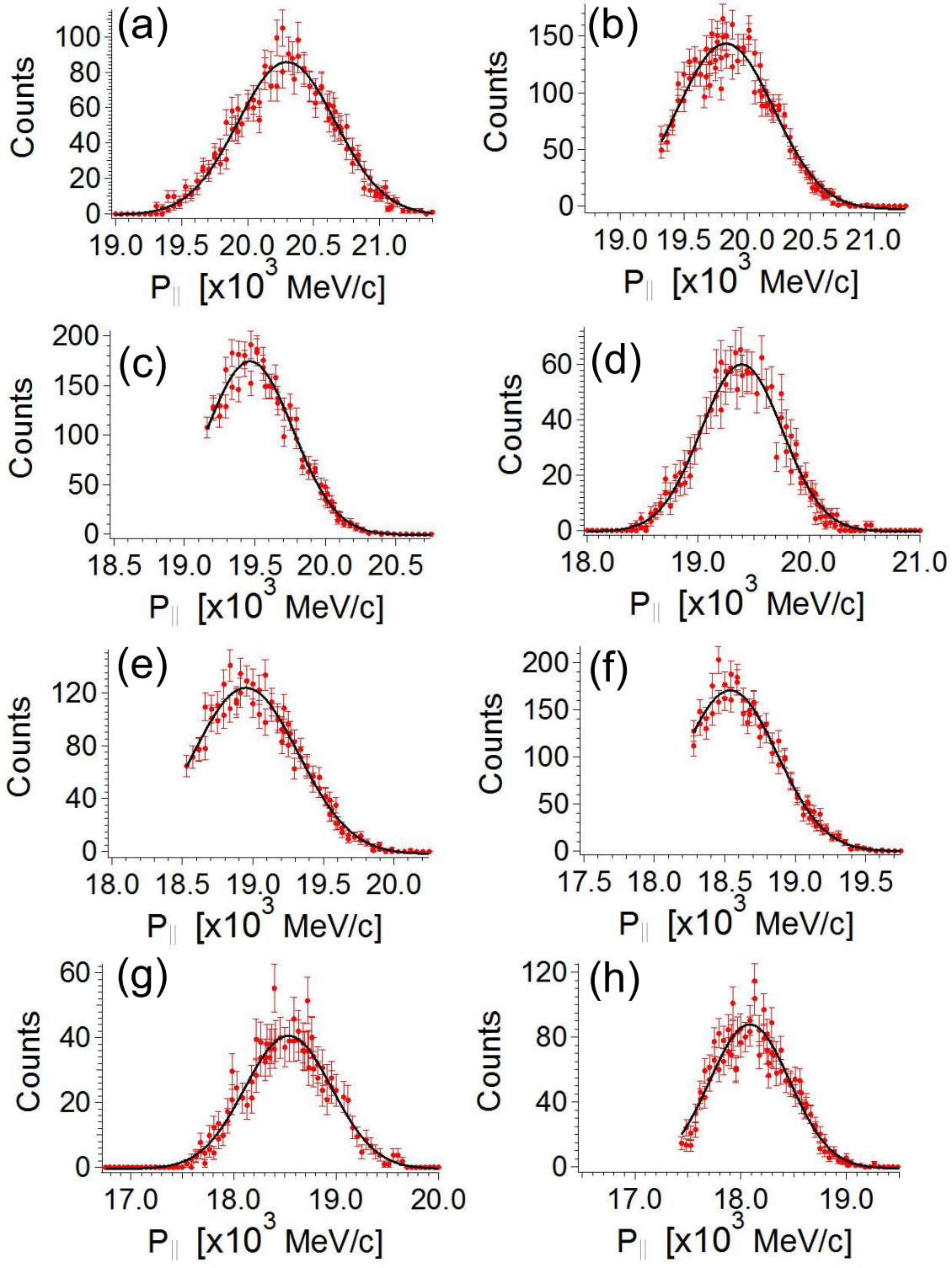

Figure A.30: Parallel momentum distributions for fragments produced from ^{76}Ge on a Au target. (a)^{47}Sc (b)^{46}Sc (c)^{45}Sc (d)^{45}Ca (e)^{44}Ca (f)^{43}Ca (g)^{43}K (h)^{42}K

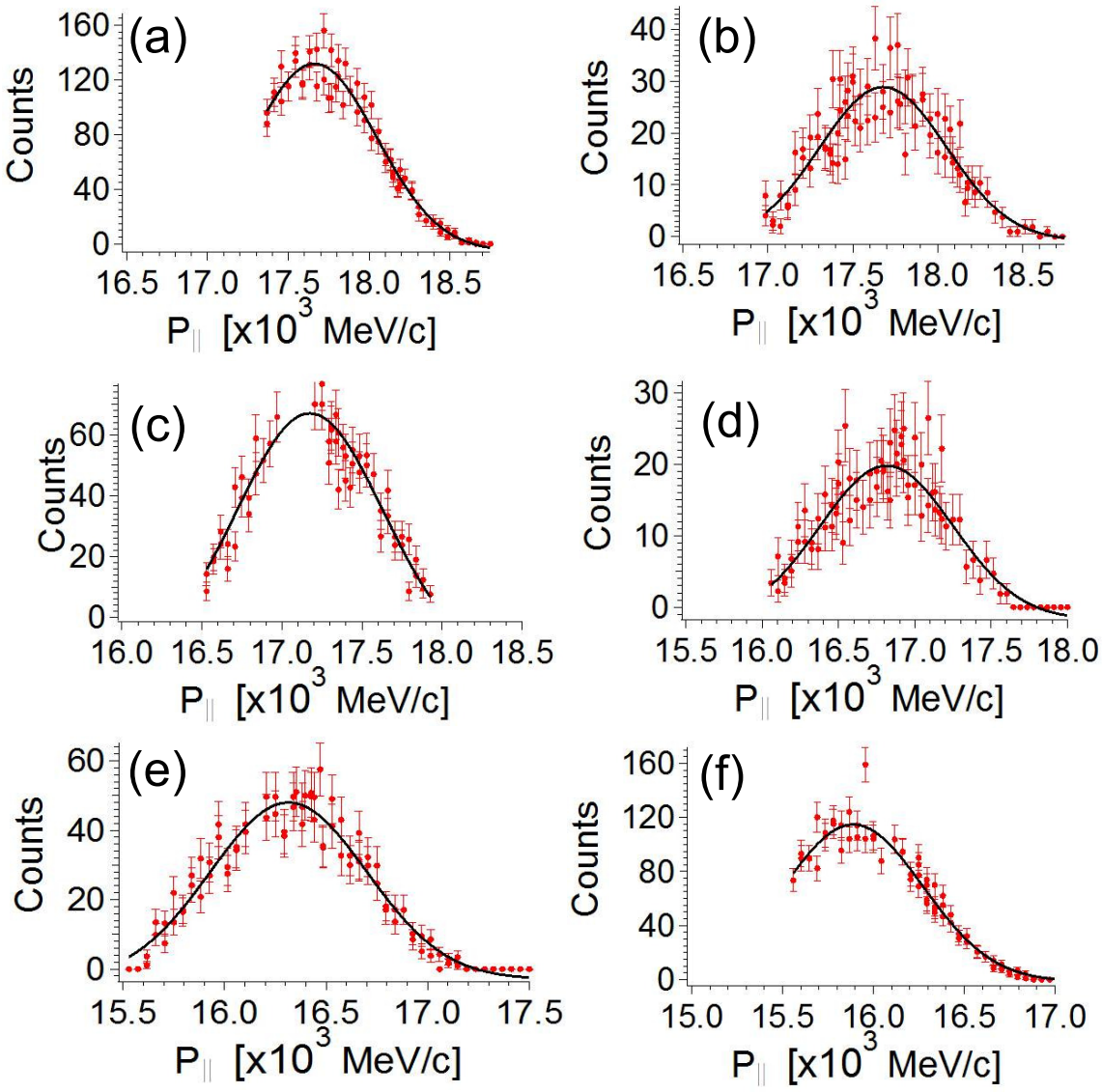

Figure A.31: Parallel momentum distributions for fragments produced from ^{76}Ge on a Au target. (a)^{41}K (b)^{41}Ar (c)^{40}Ar (d)^{39}Cl (e)^{38}Cl (f)^{37}Cl

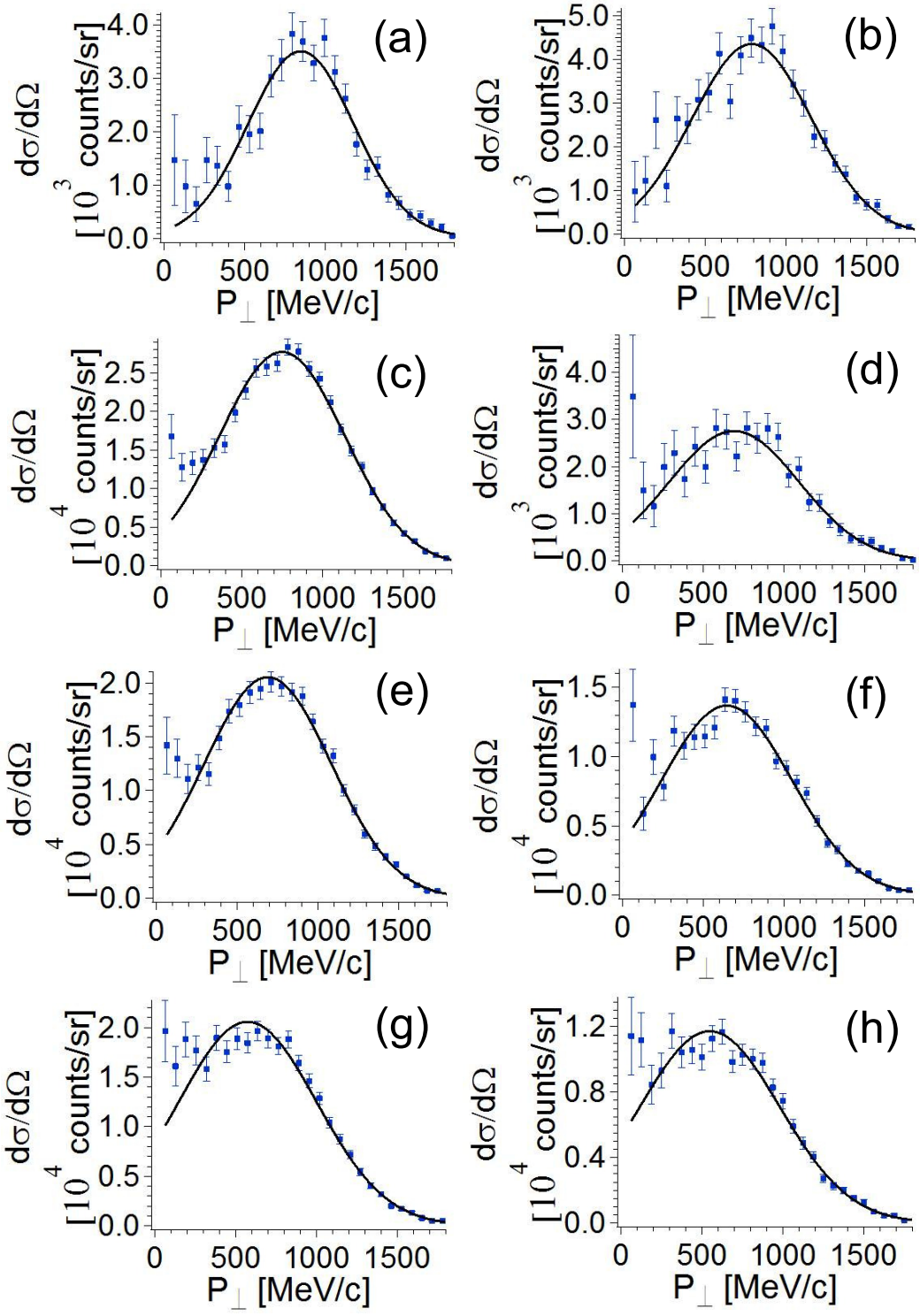

Figure A.32: Perpendicular momentum distributions for fragments produced from ^{76}Ge on a Au target. (a)^{74}As (b)^{73}As (c)^{73}Ge (d)^{72}As (e)^{72}Ge (f)^{71}Ge (g)^{71}Ga (h)^{70}Ge

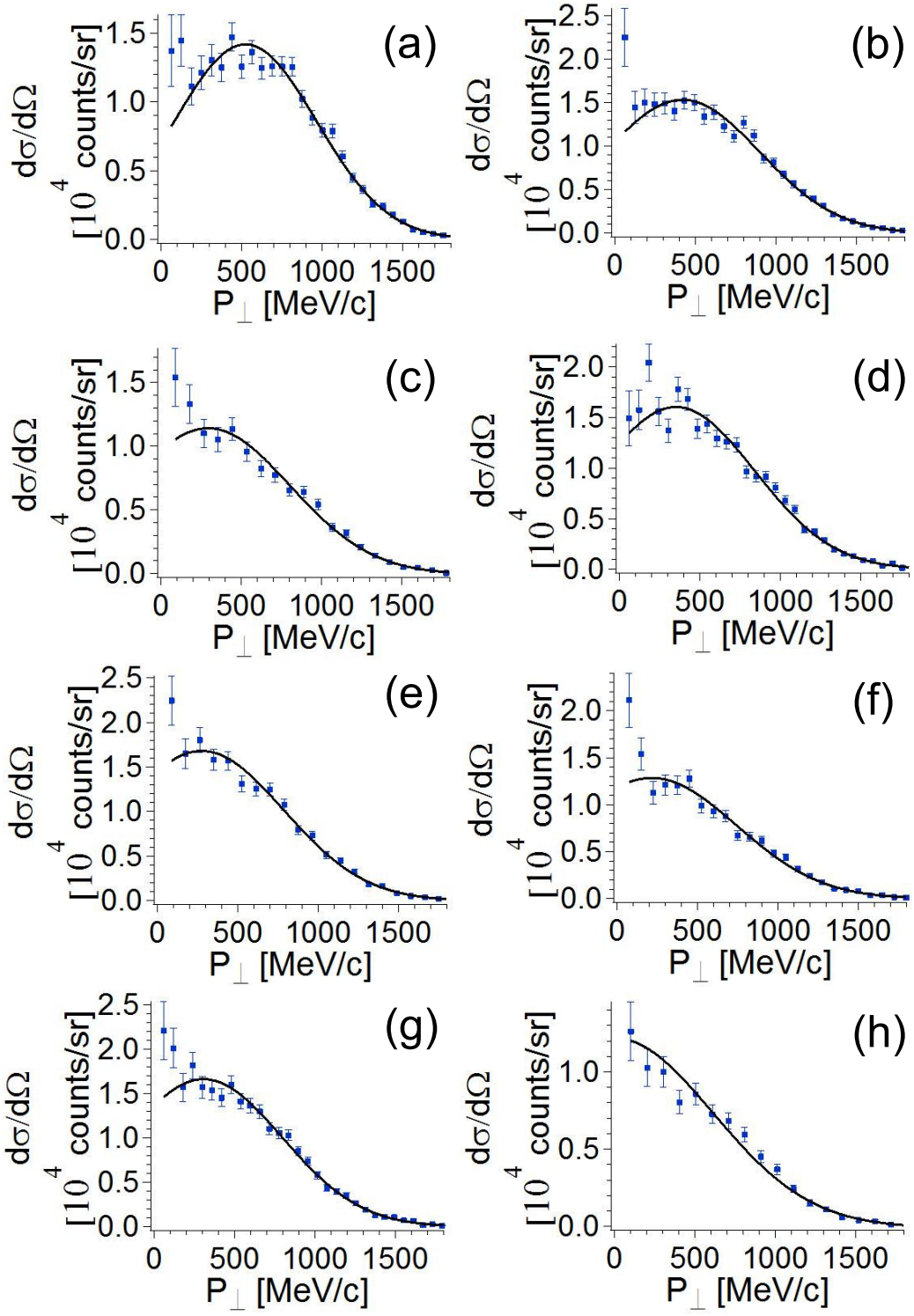

Figure A.33: Perpendicular momentum distributions for fragments produced from ^{76}Ge on a Au target. (a)^{70}Ga (b)^{69}Ga (c)^{69}Zn (d)^{68}Ga (e)^{68}Zn (f)^{67}Ga (g)^{67}Zn (h)^{67}Cu

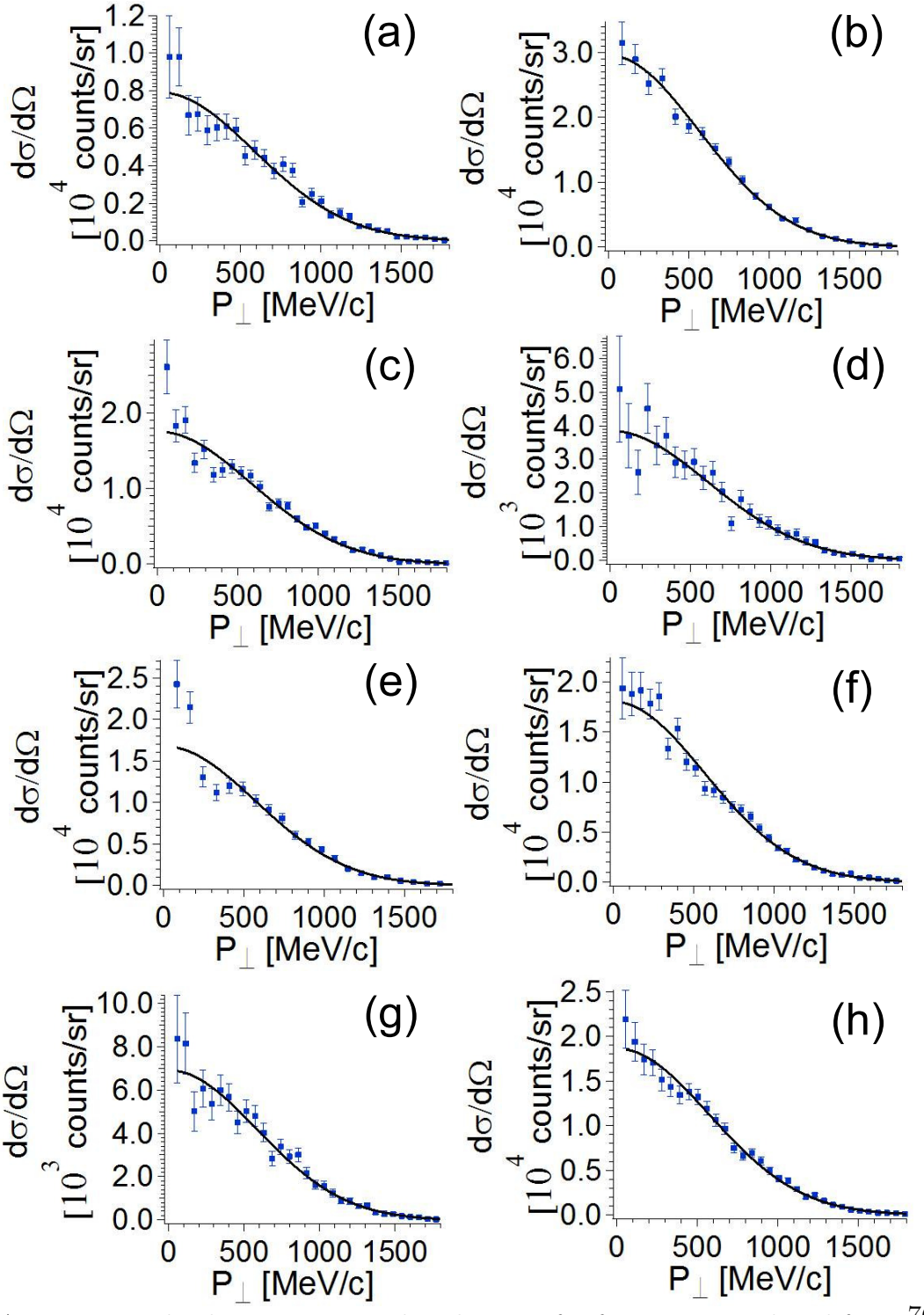

Figure A.34: Perpendicular momentum distributions for fragments produced from ^{76}Ge on a Au target. (a)^{66}Cu (b)^{65}Zn (c)^{65}Cu (d)^{65}Ni (e)^{64}Zn (f)^{64}Cu (g)^{64}Ni (h)^{63}Cu

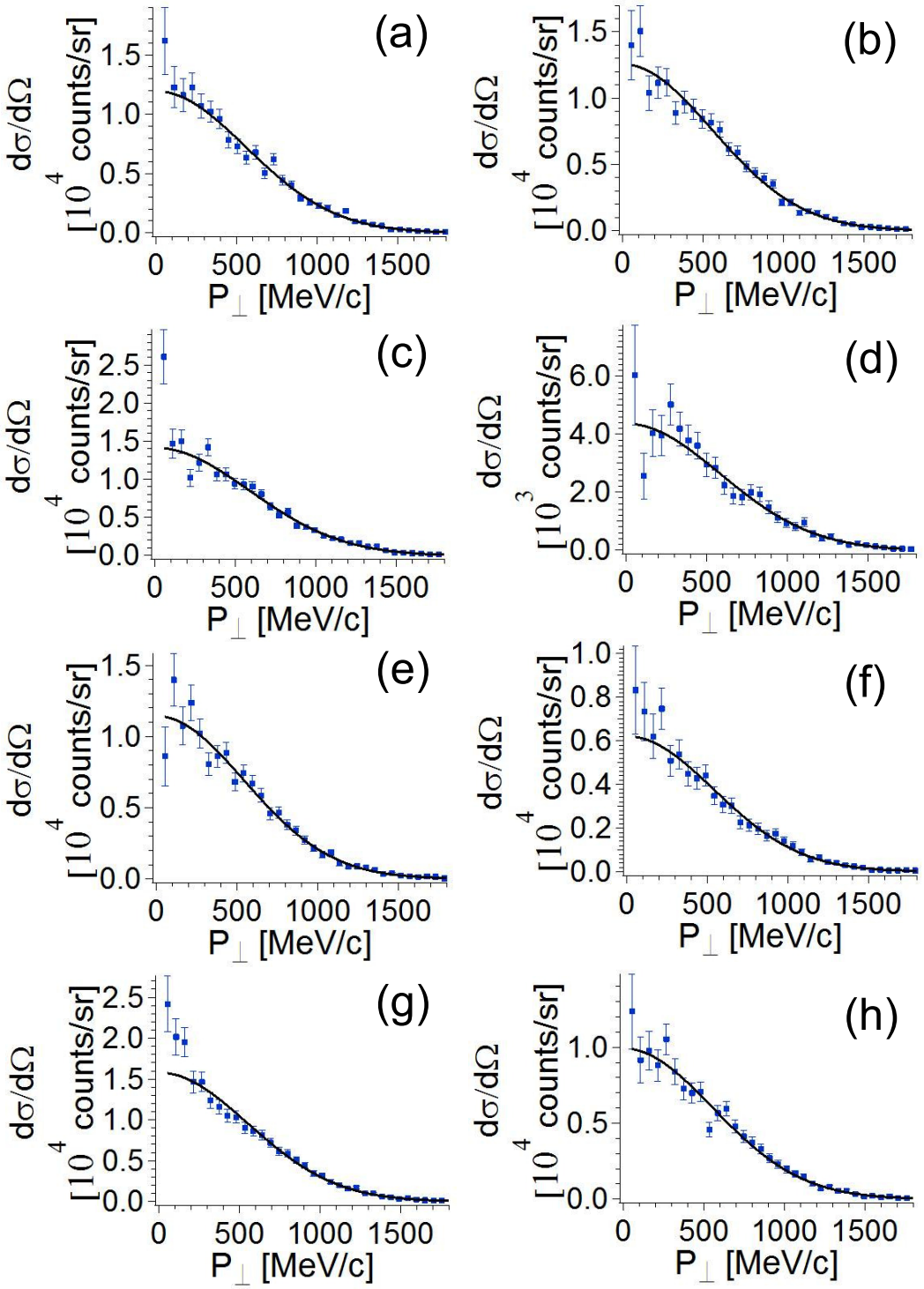

Figure A.35: Perpendicular momentum distributions for fragments produced from ^{76}Ge on a Au target. (a)^{63}Ni (b)^{62}Cu (c)^{62}Ni (d)^{62}Co (e)^{61}Ni (f)^{64}Cu (g)^{61}Co (h)^{60}Ni

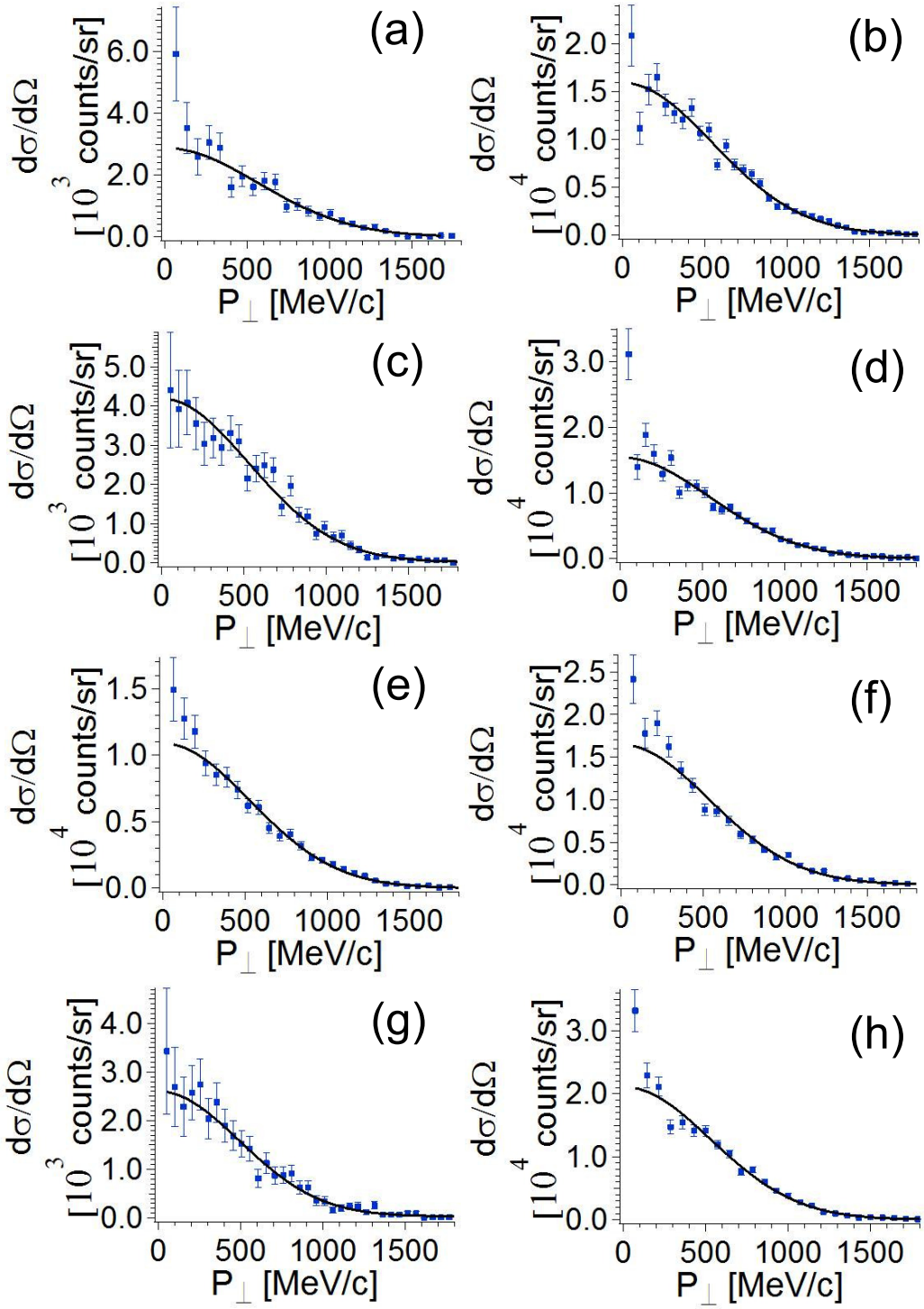

Figure A.36: Perpendicular momentum distributions for fragments produced from ^{76}Ge on a Au target. (a)^{60}Fe (b)^{59}Co (c)^{59}Fe (d)^{58}Co (e)^{58}Fe (f)^{57}Fe (g)^{57}Mn (h)^{56}Fe

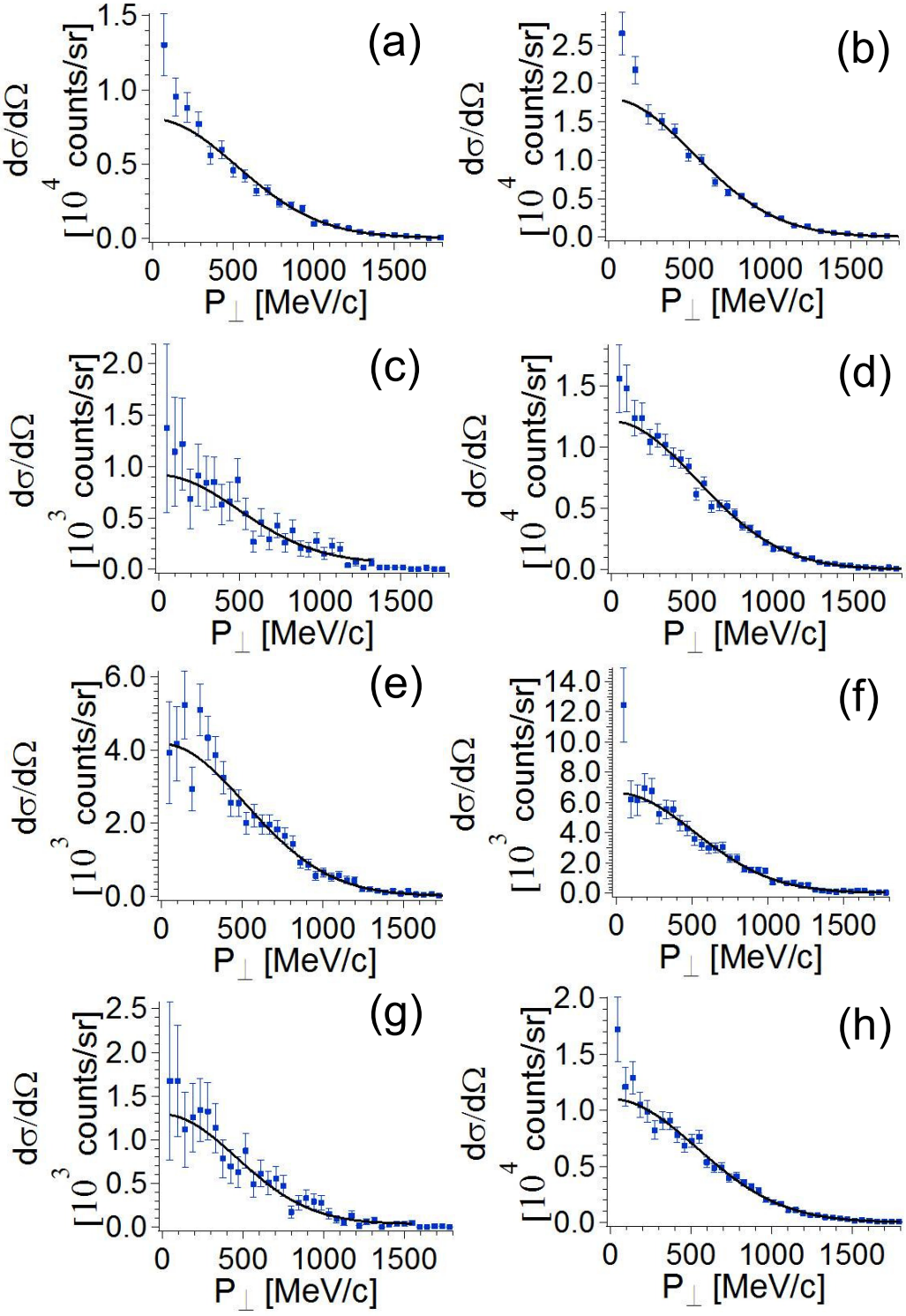

Figure A.37: Perpendicular momentum distributions for fragments produced from ^{76}Ge on a Au target. (a)^{56}Mn (b)^{55}Mn (c)^{55}Cr (d)^{54}Mn (e)^{54}Cr (f)^{53}Cr (g)^{53}V (h)^{52}Cr

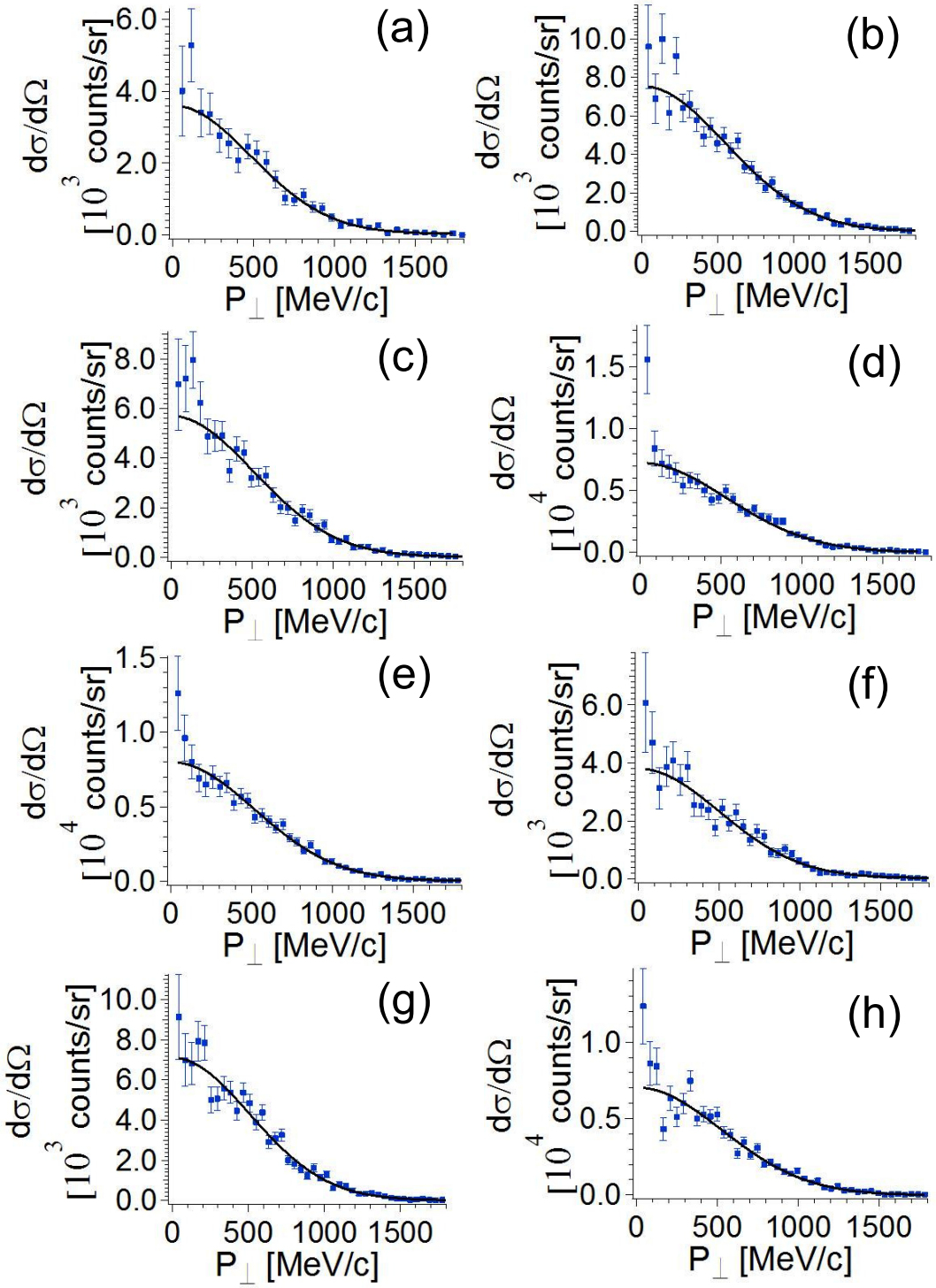

Figure A.38: Perpendicular momentum distributions for fragments produced from ^{76}Ge on a Au target. (a)^{52}V (b)^{51}Cr (c)^{51}V (d)^{50}V (e)^{49}V (f)^{49}Ti (g)^{48}Ti (h)^{47}Ti

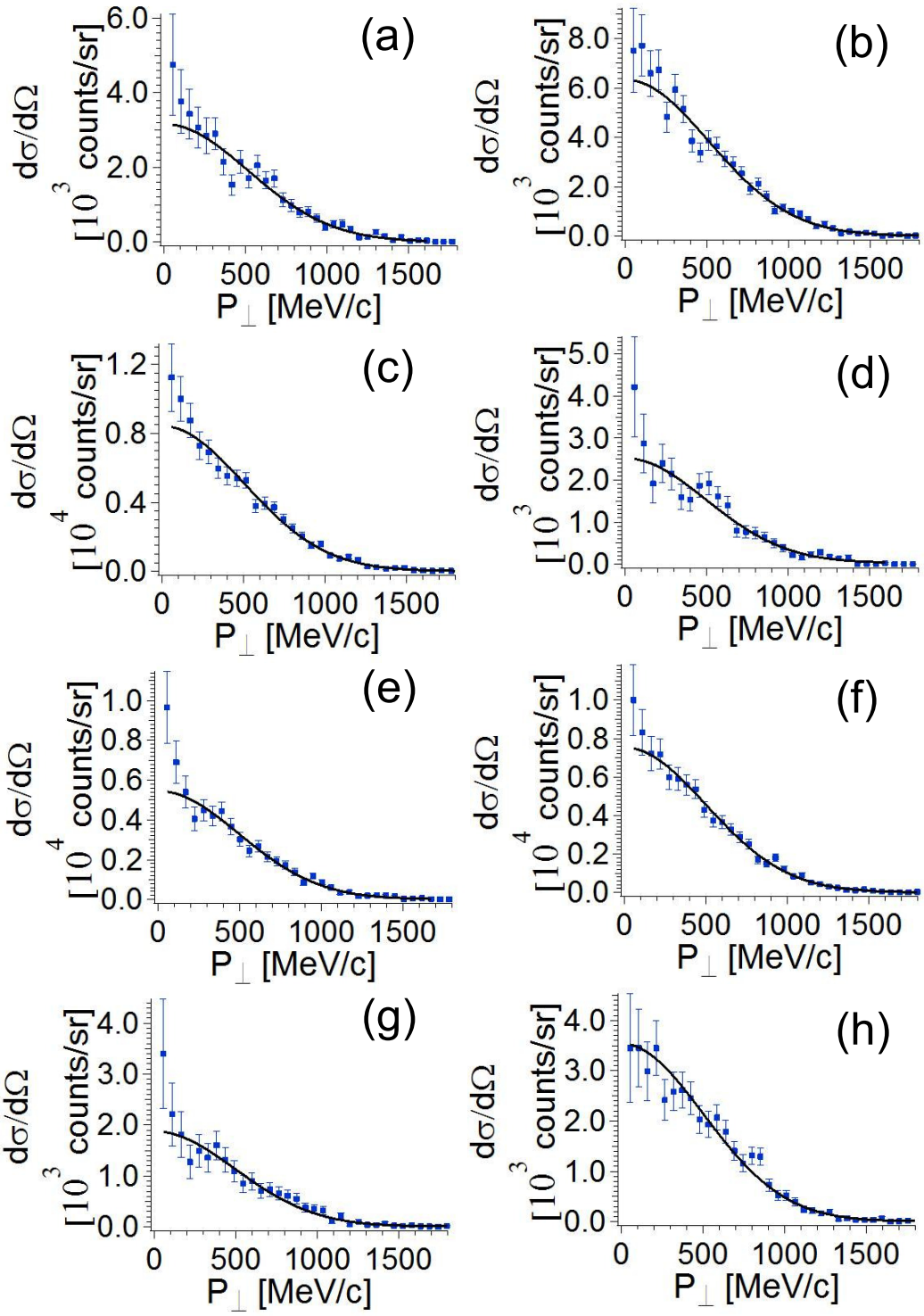

Figure A.39: Perpendicular momentum distributions for fragments produced from ^{76}Ge on a Au target. (a)^{47}Sc (b)^{46}Sc (c)^{45}Sc (d)^{45}Ca (e)^{44}Ca (f)^{43}Ca (g)^{43}K (h)^{42}K

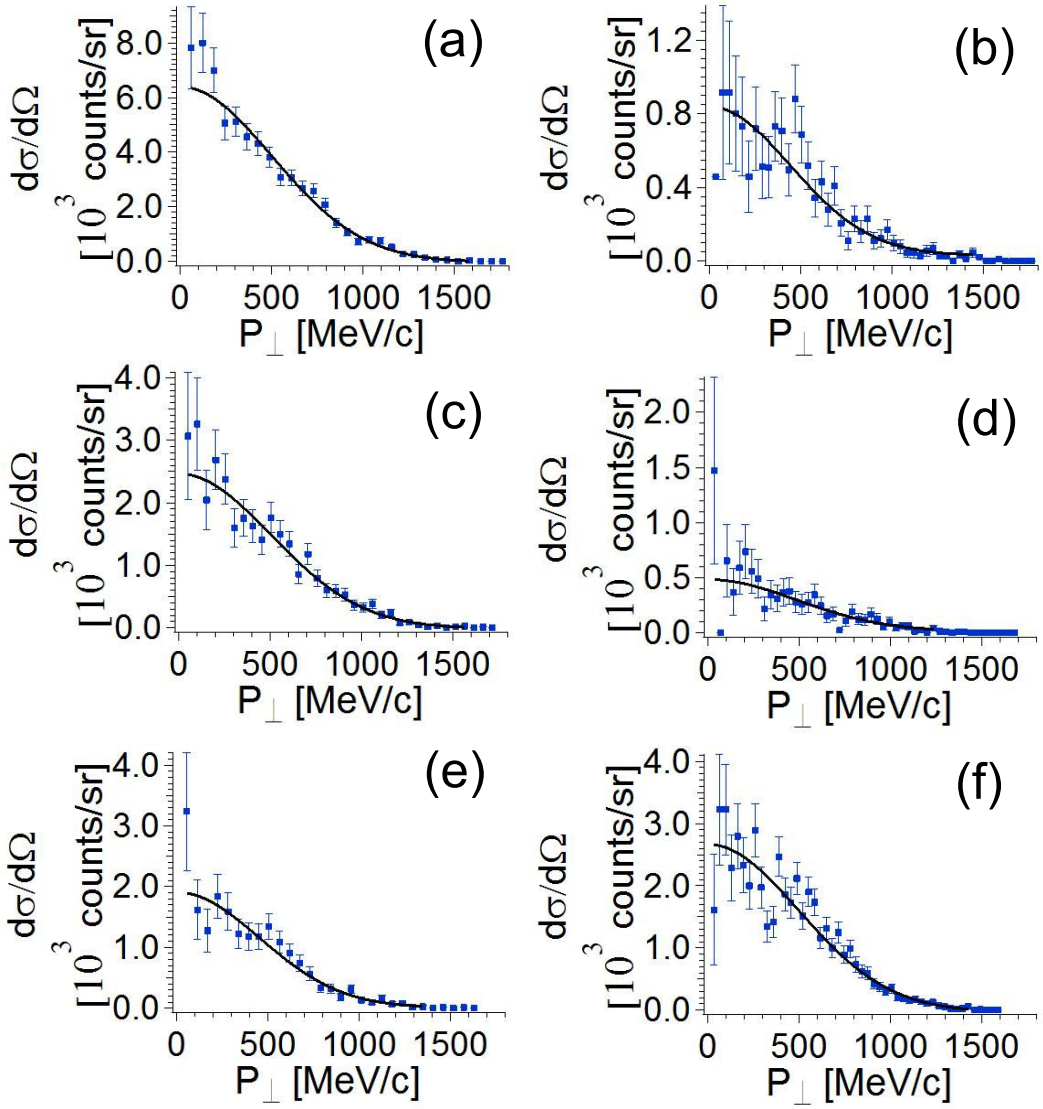

Figure A.40: Perpendicular momentum distributions for fragments produced from ^{76}Ge on a Au target. (a)^{41}K (b)^{41}Ar (c)^{40}Ar (d)^{39}Cl (e)^{38}Cl (f)^{37}Cl

BIBLIOGRAPHY

BIBLIOGRAPHY

[1] Kenneth S. Krane. *Introductory Nuclear Physics.* John Wiley and Sons, Inc., Hoboken, NJ, 1988.

[2] Walter Loveland, David J. Morrissey, and Glenn T. Seaborg. *Modern Nuclear Chemistry.* John Wiley and Sons, Inc., Hoboken, NJ, 2006.

[3] National Superconducting Cyclotron Laboratory, 2012. https://intra.nscl.msu.edu/illustrations/archive/479_150.png.

[4] R. Serber. Nuclear Reactions at High Energies. *Phys. Rev.*, 72:1114–1115, 1947.

[5] Y.P. Viyogi, T.J.M. Symons, P. Doll, D.E. Greiner, H.H. Heckman, D.L. Hendrie, P.J. Lindstrom, J. Mahoney, D.K. Scott, K. Van Bibber, G.D. Westfall, H. Wieman, H.J. Crawford, C. McParland, and C.K. Gelbke. Fragmentations of ^{40}Ar at 213 MeV/Nucleon. *Phys. Rev. Lett.*, 42:33–36, 1979.

[6] D. Guerreau, V. Borrel, D. Jacquet J. Galin, B. Gatty, and X. Tarrago. Isotopic Distributions of Projectile-like Fragments in 44 MeV/u ^{40}Ar Induced Reactions. *Phys. Lett.*, 131B:293–296, 1983.

[7] Y. Blumenfeld, PH. Chomaz, N. Frascaria, J.P. Garron, J.C. Jacmart, and J.C. Roynette. Angular Evolution of Peripheral Heavy Ion Reactions at Intermediate Energies. *Nucl. Phys. A*, 455:357–380, 1986.

[8] V. Borrel, B. Gatty, D. Guerreau, J. Galin, and D. Jacquet. Projectile Like Fragment Production in Ar Induced Reactions Around the Fermi Energy. *Z. Phys. A*, 324:205–216, 1986.

[9] D Bazin, D. Guerreau, R. Anne, D. Guillemaud-Mueller, A.C. Mueller, and M.G. Saint-Laurent. Zero Degree Measurements of Isotopic Distributions in 44 MeV/u ^{86}Kr-

Induced Reactions for the Production of Nuclei Far from Stability. *Nucl. Phys. A*, 515:349–364, 1990.

[10] M. Weber, C. Donzaud, J.P. Dufour, H. Geissel, A. Grewe, D. Guillemaud-Mueller, H. Keller, M. Lewitowicz, A. Magel, A.C. Mueller, G. Münzenberg, F. Nickel, M. Pfützner, A. Piechaczek, M. Pravikoff, E. Roeckel, K. Rykaczewski, M.G. Saint-Laurent, I. Schall, C. Stéphan, K. Sümmerer, L. Tassan-Got, D.J. Vieira, and B. Voss. Longitudinal momenta and production cross-sections of isotopes formed by fragmentation of a 500 AxMeV ^{86}Kr beam. *Nucl. Phys. A*, 578:659–672, 1994.

[11] T. Yamaguchi, T. Ohnishi, T. Suzuki, F. Becker, M. Fukuda, H. Geissel, M. Hosoi, R. Janik, A. Kelić, K. Kimura, S. Mandel, G. Münzenberg, S. Nakajima, A. Ozawa, A. Prochazka, M. Shindo, B. Sitár, P. Strmeň, T. Suda, K. Sümmerer, K. Sugawara, I. Szarka, M. Takechi, A. Takisawa, and K. Tanaka. Production cross sections of isotopes formed by fragmentation of 1A GeV ^{80}Kr beam. *Phys. Rev. C*, 74:044608–1–044608–5, 2006.

[12] Y. Yariv and Z. Fraenkel. Intranuclear cascade calculation of high-energy heavy-ion interactions. *Phys. Rev. C*, 20:2227–2243, 1979.

[13] K. Sümmerer, W. Brüchle, D.J. Morrissey, M. Schädel, B. Szweryn, and Yang Weifan. Target fragmentation of Au and Th by 2.6 GeV protons. *Phys. Rev. C*, 42:2546–2560, 1990.

[14] J. Dreute, W. Heinrich, G. Rusch, and B. Wiegel. Fragmentation of gold projectiles with energies of 200-980 MeV/nucleon. I. Experimental method, charge yields, and transverse momenta. *Phys. Rev. C*, 44:1057–1064, 1991.

[15] F.P. Brady, W.B. Christie, J.L. Romero, C.E. Tull, J.L. Chance, G.P. Grim, J.C. Young, H.J. Crawford, T. Kobayashi, P.J. Lindstrom, D.L. Olson, T.J.M. Symons, I. Tanihata, H. Wieman, W.F.J. Müller, H. Sann, and U. Lynen. Target fragmentation of Au and Th by 2.6 GeV protons. *Phys. Rev. C*, 50:R525–R529, 1994.

[16] J.L. Chance, F.P. Brady, J.L. Romero, S. Albergo, F. Bieser, Z. Caccia, D. Cebra, A.D. Chacon, Y. Choi, S. Costa, J.B. Elliott, M.L. Gilkes, J.A. Hauger, A.S. Hirsch, E.L. Hjort, A. Insolia, M. Justice, D. Keane, J.C. Kintner, V. Lindenstruth, M.A. Lisa, H.S. Matis, M. McMahan, C. McParland, W.F.J. Müller, D.L. Olson, M.D. Partlan, N.T. Porile, R. Potenza, G. Rai, J.O. Rasmussen, H.G. Ritter, J. Romanski, G.V. Russo, H. Sann, R. Scharenberg, A. Scott, Y. Shao, B.K. Srivastava, T.J.M. Symons, M. Tincknell, C. Tuve, S. Wang, P.G. Warren, H.H. Wieman, T. Wienold, and K. Wolf. Mass dependence of the transverse momenta of Au projectile fragments at 1.0A GeV. *Phys. Rev. C*, 64:014610–1–014610–5s, 2001.

[17] D.E. Greiner, P.J. Lindstrom, H.H. Heckman, Bruce Cork, and F.S. Bieser. Momentum Distributions of Isotopes Produced by Fragmentation of Relativistic ^{12}C and ^{16}O Projectiles. *Phys. Rev. Lett.*, 35:152–155, 1975.

[18] K. Van Bibber, D.L. Hendrie, D.K. Scott, H.H. Weiman, L.S. Schroeder, J.V. Geaga, S.A. Cessin, R. Treuhaft, Y.J. Grossiord, and J.O. Rasmussen. Evidence for Orbital Dispersion in the Fragmentation of ^{16}O at 90 and 120 MeV/nucleon. *Phys. Rev. Lett.*, 43:840–844, 1979.

[19] William A. Friedman. Heavy ion projectile fragmentation: A reexamination. *Phys. Rev. C*, 27:569–577, 1983.

[20] F. Rami, J.P. Coffin, B. Heusch G. Guillaume, P. Wagner, A. Fahli, and P. Fintz. Few Nucleon Transfer Versus Fragmentation in the Production of Projectile-Like Fragments in the ^{40}Ar + ^{68}Zn Reaction at 27.6 MeV/Nucleon. *Z. Phys. A*, 318:239–242, 1984.

[21] C.A. Bertulani and K.W. McVoy. Momentum distributions in reactions with radioactive beams. *Phys. Rev. C*, 46:2638–2641, 1992.

[22] C.Y. Wong and K. Van Bibber. Coulomb final state interaction and the charge effect in heavy ion projectile fragmentation at intermediate energies. *Phys. Rev. C*, 25:2990–2995, 1982.

[23] R. Pfaff, D.J. Morrissey, M. Fauerbach, M. Hellstrom, J.H. Kelley, R.A. Kryger, B.M. Sherrill, M. Steiner, J.S. Winfield, J.A. Winger, S.J. Yennello, and B.M. Young. Projectilelike fragment momentum distributions from ^{86}Kr + Al at 70 MeV/nucleon. *Phys. Rev. C*, 51:1348–1354, 1995.

[24] A.S. Goldhaber. Statistical Models of Fragmentation Processes. *Phys. Lett.*, 53B:306–308, 1974.

[25] E.J. Moinz. Pion Electroproduction from Nuclei. *Phys. Rev.*, 184:1154–1161, 1969.

[26] E.J. Moinz, I. Sick, R.R. Whitney, J.R. Ficenec, R.D. Kephart, and W.P. Trower. Nuclear Fermi Momenta from Quasielastic Electron Scattering. *Phys. Rev. Lett.*, 26:445–448, 1971.

[27] V. Borrel, D. Guerreau, J. Galin, B. Gatty, D. Jacquet, and X. Tarrago. Peripheral Ar Induced Reactions at 44 MeV/u - Similarities and Deviations with Respect to a High Energy Fragmentation Process. *Z. Phys. A*, 314:191–197, 1983.

[28] G.A. Souliotis, D.J. Morrissey, N.A. Orr, B.M. Sherrill, and J.A. Winger. 0° measurements of momentum distributions of projectile-like fragments. *Phys. Rev. C*, 46:1383–1392, 1992.

[29] M.J. Murphy and R.G. Stokstad. Momentum widths of heavy-ion reaction products at 27.4 MeV/nucleon. *Phys. Rev. C*, 28:428–431, 1983.

[30] Ch. Egelhaaf, G. Bohlen, H. Fuchs, A. Gamp, H. Homeyer, and H. Kluge. Small Momentum Widths in Heavy-Ion Fragmentation at 20 MeV/amu and Below. *Phys. Rev. Lett.*, 46:813–816, 1981.

[31] Bernard G. Harvey. Comment on Small Momentum Widths in Heavy-Ion Fragmentation at 20 MeV/nucleon and Below. *Phys. Rev. Lett.*, 47:454, 1981.

[32] J.B. Natowitz, M.N. Namboodiri, L. Adler, R.P. Schmitt, R.L. Watson, S. Simon, M. Berlanger, and R. Choudhury. Particle Emission at ^{20}Ne Projectile Velocity Comparable to the Fermi Velocity. *Phys. Rev. Lett.*, 47:1114–1117, 1981.

[33] J. Mougey, R. Ost, M. Buenerd, A.J. Cole, C. Guet, D. Lebrun, J.M. Loiseaux, P. Martin, M. Maurel, E. Monnand, H. Nifenecker, P. Perrin, J. Pinston, C. Ristori, P. de Saintignon, F. Schussler, L. Carlén, B. Jakobsson, A. Oskarsson, I. Otterlund, B. Schroder, H.A. Gustafsson, T. Johansson, H. Ryde, J.P. Bondorf, O.B. Nielsen, and G. Tibell. Projectile Fragments from 86 MeV/nucleon ^{12}C Induced Reactions. *Phys. Lett. B*, 105:25–29, 1981.

[34] Y. Cassagnou, M. Conjeaud, R. Dayras, S. Harar, R. Legrain, E.C. Pollacco, C. Volant, J. Menet, and J.B. Vianno, 1983. XXI International Winter Meeting on Nuclear Physics Bormio, 610.

[35] Y. Blumenfeld, J.C. Roynette, Ph. Chomaz, N. Frascaria, J.P. Garron, J.C. Jacmart, M. Buenerd, A. Gamp, D. Lebrun, and Ph. Martin, 1983. Proc. Cong. de la Soc. Franc. de Phys. Grenoble, 43.

[36] D.J. Morrissey. Systematics of momentum distributions from reactions with relativistic ions. *Phys. Rev. C*, 39:460–470, 1989.

[37] O.B. Tarasov, M. Portillo, A.M. Amthor, T. Baumann, D. Bazin, A. Gade, T.N. Ginter, M. Hausmann, N. Inabe, T. Kubo, D.J. Morrissey, A. Nettleton, J. Pereira, B.M. Sherrill, A. Stolz, and M. Thoennessen. Production of very neutron-rich nuclei with a ^{76}Ge beam. *Phys. Rev. C*, 80:034609–1–034609–11, 2009.

[38] P.A. Zavodszky, B. Arend, D. Cole, J. DeKamp, G. Machicoane, F. Marti, P. Miller, J. Moskalik, J. Ottarson, J. Vincent, and A. Zeller. Design of SuSI - superconducting source for ions at NSCL/MSU - II. The conventional parts. *Nucl. Instr. and Meth. B*, 241:959–0964, 2005.

[39] D.J. Morrissey, B.M. Sherrill, M. Steiner, A. Stolz, and I. Widenhoever. Commissioning the A1900 projectile fragment separator. *Nucl. Instr. and Meth. B*, 204:90–96, 2003.

[40] A. Stolz, T. Baumann, T.N. Ginter, D.J. Morrissey, M.Portillo, B.M. Sherrill, and M. Steiner an J.W. Stetson. Production of rare isotope beams with the NSCL fragment separator. *Nucl. Instr. and Meth. B*, 241:858–861, 2005.

[41] D. Bazin, J.A. Caggiano, B.M. Sherrill, J. Yurkon, and A. Zeller. The S800 spectrograph. *Nucl. Instr. and Meth. B*, 204:629–633, 2003.

[42] J. Yurkon, D. Bazin, W. Benenson, D.J. Morrissey, B.M. Sherrill, D. Swan, and R. Swanson. Focal plane detector for the S800 high-resolution spectrometer. *Nucl. Instr. and Meth. A*, 422:291–295, 1999.

[43] J. Yurkon, 2012. Private communication.

[44] Glenn F. Knoll. *Radiation Detection and Measurement Third Edition*. John Wiley and Sons, Inc., Hoboken, NJ, 2000.

[45] ScintiTech, 2010. http://www.scintitech.com/.

[46] K. Makino and M. Berz. COSY INFINITY version 8. *Nucl. Instr. and Meth. A*, 427:338–343, 1999.

[47] SpecTcl, 1999. http://docs.nscl.msu.edu/SpecTcl.

[48] Version 6.2.2.2 Igor Pro, 2011. WaveMetrics, Inc, Lake Oswego, Oregon.

[49] D. Bazin, 2010. Private communication.

[50] S. Keszthelyi-Lándori and G. Hrehuss. Scintillation response function and decay time of CsI(Na) to Charged Particles. *Nucl. Instr. and Meth.*, 68:9–12, 1969.

[51] D. Horn, G.C. Ball, A. Galindo-Uribarri, E. Hagberg, R.B. Walker, R. Laforest, and J. Pouliot. The mass dependence of CsI(Tl) scintillation response to heavy ions. *Nucl. Instr. and Meth. A*, 320:273–276, 1992.

[52] N. Colonna, G.J. Wozniak, A. Veeck, W. Skulski, G.W. Goth, L. Manduci, P.M. Milazzo, and P.F. Mastinu. Calibration of the response function of CsI(Tl) scintillators to intermediate-energy heavy ions. *Nucl. Instr. and Meth. A*, 321:529–534, 1992.

[53] P.F. Mastinu, P.M. Milazzo, M. Bruno, M. D'Agostino, and L. Manduci. Calibration of CsI(Tl) scintillators for heavy ions ($3 \leq Z \leq 54$) in a wide energy range ($E/u \leq 60$ MeV/u). *Nucl. Instr. and Meth. A*, 338:419–424, 1994.

[54] A.S. Fomichev, I. David, S.M. Lukyanov, Yu.E. Penionzhkevich, N.K. Skobelev, O.B. Tarasov, A. Matthies, H.-G. Ortlepp, W. Wagner, M. Levitowicz, M.G. Saint-Laurent, J.M. Corre, Z. Dlouhý, I. Pecina, and C. Borcea. THe response of a large CsI(Tl) detector to light particles and heavy ions in the intermediate energy range. *Nucl. Instr. and Meth. A*, 344:378–383, 1994.

[55] Y. Larochelle, L. Beaulieu, B. Djerroud, D. Doré, P. Gendron, E. Jalbert, R. Laforest, J. Pouliot, R. Roy, M. Samri, and C. St-Pierre. Energy-light relation for CsI(Tl) scintillators in heavy ion experiments at intermediate energies. *Nucl. Instr. and Meth. A*, 348:167–172, 1994.

[56] A. Wagner, W.P. Tan, K. Chalut, R.J. Charity, B. Davin, Y. Larochelle, M.D. Lennek, T.X. Liu, X.D. Liu, W.G. Lynch, A.M. Ramos, R. Shomin, L.G. Sobotka, R.T. de Souza, M.B. Tsang, G. Verde, and H.S. Xu. Energy-light relation for CsI(Tl) scintillators in heavy ion experiments at intermediate energies. *Nucl. Instr. and Meth. A*, 456:290–299, 2001.

[57] M. Pârlog, B. Borderie, M.F. Rivet, G. Tăbăcaru, A. Chbihi, M. Elouardi, N. Le Neindre, O. Lopez, E. Plagnol, L. Tassan-Got, G. Auger, Ch.O. Bacri, N. Bellaize, F. Bocage, R. Bougault, B. Bouriquet, R. Brou, P. Buchet, J.L. Charvet, J. Colin, D. Cussol, R. Dayras, A. Demeyer, D. Doré, D. Durand, J.D. Frankland, E. Galichet, E. Genouin-Duhamel, E. Gerlic, S. Hudan, D. Guinet, P. Lautesse, F. Lavaud, J.L. Laville, J.F. Lecolley, C. Leduc, R. Legrain, M. Louvel, A.M. Maskay, L. Nalpas, J. Normand, J. Péter, E. Rosato, F. Saint-Laurent, J.C. Steckmeyer, B. Tamain, O. Tirel, E. Vient, C. Volant, and J.P. Weileczko. Response of CsI(Tl) scintillators over a large range in energy and atomic number of ions. Part II: calibration and identification in the INDRA array. *Nucl. Instr. and Meth. A*, 482:693–706, 2002.

[58] O.B. Tarasov and D. Bazin. LISE++: Radioactive beam production with in-flight separators. *Nucl. Instr. and Meth. B*, 266:4657–4664, 2008.

[59] J.B. Birks. Scintillators from Organic Crystals: Specific Fluorescence and Relative Response to Different Radiations. *Proc. Phys. Soc. A*, 64:874–877, 1951.

[60] J.B. Birks. *The Theory and Practice of Scintillation Counting*. Pergamon Press, Oxford, 1964.

[61] D. Bazin, 2011. Private communication.

[62] C.A. Bertulani and P. Danielewicz. *Introduction to Nuclear Reactions*. Institute of Physics Publishing London, 2004.

[63] J. Blocki, J. Randdrup, W.J. Światecki, and C.F. Tsang. Proximity Forces. *Annals of Phys.*, 105:427–462, 1977.